Development of a Novel Magnetic Single Cell Micro Array

by

William Wing Ning Liu
BASc, University of Toronto, 2006

A Thesis Submitted in Partial Fulfillment
of the Requirements for the Degree of

MASTER OF APPLIED SCIENCE

in the Department of Mechanical Engineering

Supervisory Committee

Development of a Novel Magnetic Single Cell Micro Array

by

William Wing Ning Liu
BASc, University of Toronto, 2006

Supervisory Committee

Dr. Nikolai Dechev
Department of Mechanical Engineering, University of Victoria, BC, Canada
Supervisor

Dr. Edward J. Park
Department of Mechanical Engineering, University of Victoria, BC, Canada
Departmental Member

Dr. Andrew Rowe
Department of Mechanical Engineering, University of Victoria, BC, Canada
Departmental Member

Abstract

Supervisory Committee
Dr. Nikolai Dechev
Department of Mechanical Engineering, University of Victoria, BC, Canada
Supervisor
Dr. Edward J. Park
Department of Mechanical Engineering, University of Victoria, BC, Canada
Departmental Member
Dr. Andrew Rowe
Department of Mechanical Engineering, University of Victoria, BC, Canada
Departmental Member

Single cell analysis techniques are valuable for revealing individual cell behaviour, which is of interest to many researchers. In such experiments, various types of devices capable of aligning cells into organized arrays are often used. Application of cell arrays reduces the cell-cell interaction during the experiment, allows parallel analysis of cells and facilitates the use of automated equipment. This thesis documents the development of a novel Magnetic Single Cell Micro Array (MSCMA), which makes use of magnetic force to array cells. The working principles, process of design, simulation and fabrication of the prototypes of the MSCMA are described. Prototypes of the MSCMA were successfully fabricated and tested using Jurkat cells that have been labelled with immunomagnetic labels. Experimental results show that the prototypes are effectively in capturing and arraying the cells labelled with immunomagnetic labels. In addition, tests using simple magnetic particles revealed the behaviour of the magnetic field created by the MSCMA, and matched the simulation results well. Although the prototypes suffered from some fabrication defects, these defects had little effect on the performance of the prototypes. Design changes to the MSCMA are proposed for future work, such as implementing a transparent substrate, and addressing the issues of fabrication defects.

Table of Contents

List of Tables

List of Figures

Acknowledgments

I would like to use this opportunity to express my sincerest thanks to Dr. Nikolai Dechev, and Dr. Edward Park. I deeply appreciate their invaluable guidance, inspiration and advice on my academic works and my personal life. I am delighted to have this opportunity to involve in this fascinating project and intriguing research group.

Moreover, I would like to thank Dr. Robert Burke and Dr. Diana Wang for their support on the material and advice for conducting the biological experiments. Their precious advice is an important help for me to complete this thesis. I am especially thankful for the time and effort that Dr. Wang had put into culturing and preparing the cells. Without her help, the experiments in this work would not be possible.

I would also like to thank Dr. Ash Parameswaran for letting me to access the micro fabrication facility at Simon Fraser University, Mr Sae-Won Lee and Dr. Ian Foulds for their helps in fabricating the prototypes of the MSCMA.

Lastly, I would like to acknowledge the support from my friends and families. Their encouragement and support are the biggest motivation behind my works. Thank everyone who has given me their support in person or from other part of the World over the course of this thesis.

Dedication

To my parents and my warm-hearted grandmother, for raising and taking care of me with their greatest generosity.

In memory of my late grandfather, who did not have the chance to share my accomplishment with me.

Chapter 1 Introduction

Research experiments involving biological cells are often done by studying cells in bulk, which means cell properties are usually measured and averaged over the entire cell population. However, research has shown that single cell behaviour can vary significantly from individual to individual [1-5]. Thus, the distribution of various cell properties and the dynamic response of cells to stimuli can easily be hidden in the averaged experimental measurements. Therefore single cell analysis techniques are becoming more and more popular. Some applications, such as drug screening [6-9], identifying and sorting cells [10-12] and bio-sensors [13-14], have already been demonstrated by several research groups.

Currently, single cell analysis is usually done with flow cytometry [1,4,11]. In flow cytometry, cells with fluorescent labels are passed through a capillary, while a fluorescent probe reads the fluorescent properties of each passing cell that is excited by a laser source. Using this technique, millions of fluorescently labelled cells can be checked in a short time, which makes it a very useful tool for scientists to measure the distribution of cell parameters. In addition, flow cytometry is also the backbone of Fluorescence Activated Cell Sorting (FACS). However, flow cytometry is limited to discriminating cells by the strength of the fluorescent labels on them. Other valuable information, such as the spatial localization of fluorescence within the cells, time dependent cell dynamics, and cell secretion cannot be monitored by this technique [1,4,11,15]. Moreover, long-term cell identification in flow cytometry devices is virtually impossible [16], which greatly limits the ability of such devices on checking time dependent response of individual cells [1,4,15].

In addition to flow cytometry, there are also other single cell analysis techniques. For example, laser scanning cytometry is a variant of flow cytometry that uses an excitation laser to scan through an immobilized culture of cells [1,17]. This method has the capability of measuring the time dependent cell properties, since the same culture can be scanned multiple times. Another single cell analysis technique is automated microscopy [6,18-19], which uses an automated microscope system and digital imaging technology to evaluate hundreds of different cells in a culture. This method can yield more valuable parameters by using the microscopic image, such as the nucleus shape and multiple protein distributions within a cell [1,6]. Moreover, these techniques are capable to measure the dynamic response of the cells while flow cytometry cannot.

In recent years, immobilization and manipulation of individual cells has become possible with advances in micro-fabrication technology and material science. Such advancements allow researchers to organise cells in a structured array and open up more opportunities for studying and using cells individually. Studying arrayed cells is motivated by a number of reasons. First of all, each individual cell in an array is separated from every other cell, thus cell-cell interaction on the device is better controlled than in an unstructured environment [1]. Moreover, studying individual cells in an array allows researchers to evaluate the cells in parallel, while they are all subjected to the same process. This increases the throughput of single cell experiments in contrast with serial experiments of single cells, such as flow cytometry [15]. Additionally, an address can be assigned to each individual cell, which makes tracking cells in an experiment simpler. With the assigned address, data logging of each individual cell is achievable which is particularly useful for studying time dependent response on large numbers of

cells [10,15-16]. Addressed cell arrays also facilitate the use of machine automation for performing experiments. Since the cells are held in place at predefined and addressed locations, the automation tasks are simplified by reducing the computational power for locating and tracking individual cells in comparison to a dynamic or unstructured environment [1,10,12]. This is especially important when evaluating non-adherent cell types with scanning microscopy techniques.

In previous attempts to array cells, researchers have manipulated cells with the application of different mechanical, chemical and electromagnetic forces [16-17]. Among these many approaches, magnetic cell manipulation is one of the most common approaches. The research presented in this thesis utilizes the proven concept of magnetic cell manipulation and proposes a novel Magnetic Single Cell Micro Array (MSCMA) for creating arrays of single cells. This thesis will discuss the background information of the proposed MSCMA, the basic theory of magnetic cell manipulation, the development of the MSCMA prototypes, and the results of experimental evaluations on the MSCMA prototypes.

Chapter 2 Background

Over the last decade, many researchers have devoted their efforts to the development of cell arraying devices. In these devices, actuation based on mechanical, chemical or electromagnetic interaction between the cells and their surroundings is used [20-21]. The following sections will illustrate and discuss each of these techniques in detail.

2.1 Mechanical Cell Arrays

Mechanical cell arrays are perhaps the simplest of all cell arraying techniques. Cells in these arrays are simply placed in a container that has many micro-wells on its bottom [3,16,22,23], and allowed to settle into these wells under the influence of gravity. Examples of these devices are shown in Fig. 2-1(a-b). These arrays are generally fabricated with common micro-fabrication processes, such as masked isotropic etching [3,16], soft-lithography [22], or micro-injection moulding [23]. More elaborate arrays may be created using extruded features on the wall of a micro-channel to stop the cells in the flowing medium [24], shown in Fig. 2-1(c), or by using micro-channels to deliver suction to an array of openings on the bottom of a cell container [25], as shown in Fig. 2-1(d). Although these methods are generally simple, quick and reversible, these methods are not selective. In other words, they are not capable of separating specific cells of interest. In a special category of mechanical cell arrays, cells can be put into an array without the help of a physical structure. Albrecht *et al.* [26] demonstrated the process of curing a hydrogel around a cell or a group of cells, thus forming an encapsulation around a cell of interest and trapping it. Fig. 2-1(e) shows a sheet of cured hydrogel and the array of cells trapped within it. Another approach in this category is the use of acoustic traps [21]. The acoustic traps are formed by several crossed, standing ultrasonic waves in a

micro-fluidic chamber, which results in a cell array as shown in Fig. 2-1 (f). The differential pressure at different parts of the wave causes the cells to accumulate at the nodes and the anti-nodes of the wave. Similar to other mechanical cell arrays, both methods do not offer any selectivity for cell separation. In contrast, employing these arraying methods does not require any micro-fabrication to be done, since there are no physical micro-features. However, controlling the size and the number of cells that can be fitted in each trap is tricky, because of the lack of physical constraints.

2.2 Chemical Cell Arrays

Another common approach of creating cells arrays is with the use of chemicals. Cell-adhesive ligands can be patterned onto a substrate to create a cell array. For example, Halter *et al*. [19] have successfully created fibroblasts arrays, shown in Fig. 2-2(a), by contact printing fibronectin onto a coverslip with a Polydimethylsiloxane (PDMS) stamp. In some applications, where the cells in the array are subject to constant fluid flow, the chemical adherent may not be strong enough to hold the cells in place. Thus mechanical micro-wells, such as the configuration of Fig. 2-2(b), may be used in conjunction with the adherent coating to hold the cells in position [13,27]. Unlike mechanical based methods, specific cell types can be selected by the process of applying the corresponding ligands onto the array. However, the effectiveness of this method is highly dependent on the nature of the cell and the corresponding ligands, thus it does not work well for all cell types. Moreover the process is slow, and can be difficult to trigger and reverse [20,28].

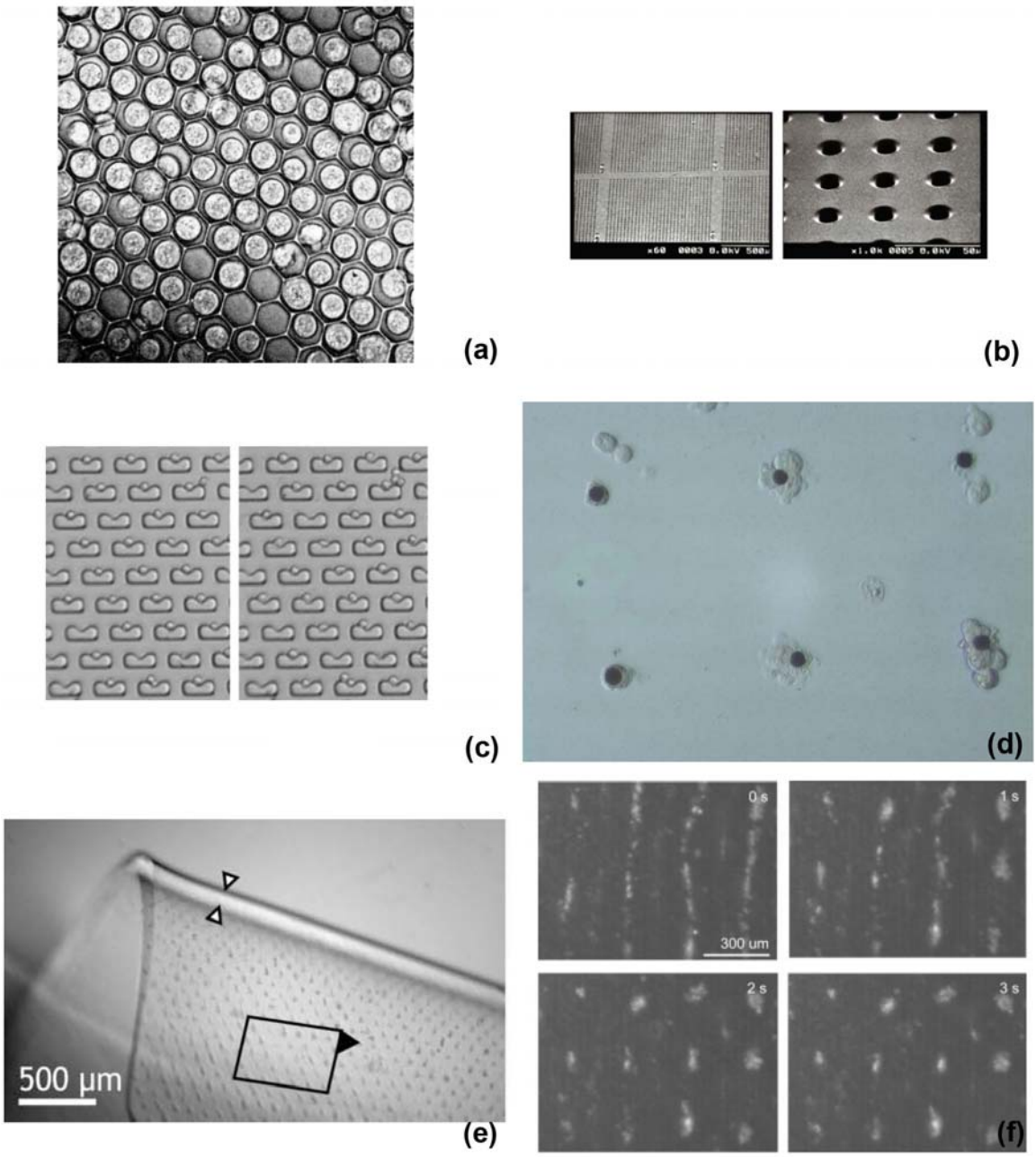

Figure 2-1 Different types of mechanical cell arrays, includings, (a-b) Micro-well arrays [16,23], (c) extruded stops array [24], (d) vacuum arrays [25], (e) hydrogel encapsulation array [26], and (f) acoustic trapping array [21].

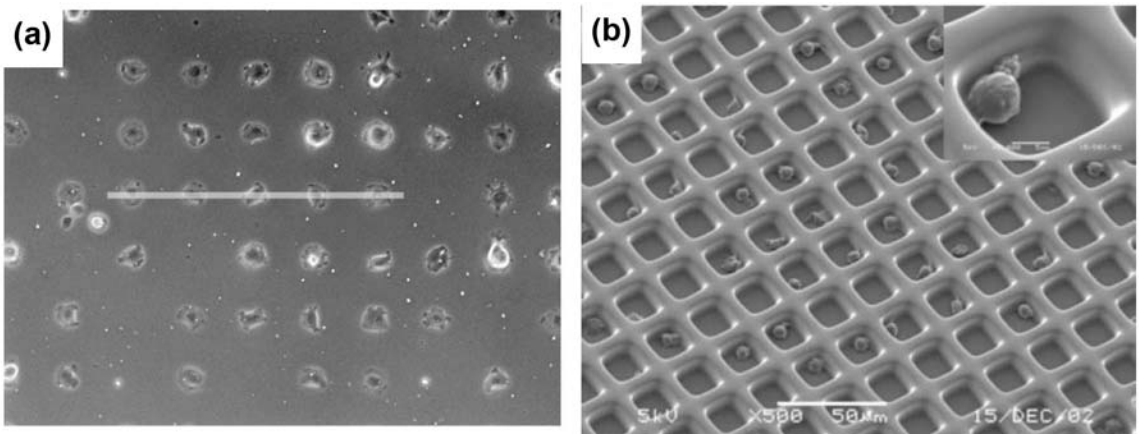

Figure 2-2 Chemical adherent cell arrays. (a) shows the cell stick to a patterned cell adherent [19], (b) shows a hybrid mechanical and chemical cell array [27].

2.3 Electromagnetic Cell Arrays

In addition to mechanical and chemical methods, cells can also be put into an array with the help of an electromagnetic field. For example, dielectrophorectic (DEP) arraying methods [11-12,29] use an electric field to position the cells. Depending on the electrical properties of the cells and the medium around the cells, the cells are either attracted toward the stronger field (positive-DEP) or repelled from it (negative-DEP). Since this technique relies on the inherent properties of the cells, cell surface markers are not necessary, though the markers can be used to increase the selectivity of the process [30]. To position the cells into an array, the electrodes are fabricated on the surface of the devices. Depending on the actuation mode, negative-DEP [11] or positive-DEP [12], the electrodes are arranged to provide the appropriate electric field profile. Thus a negative-DEP electrode configuration, such as the one that is shown in Fig. 2-3(a), will not work with the cell and medium combination that is meant for positive-DEP and vice versa. To overcome this problem, Chiou *et al*. [29] presented a reconfigurable electrode design by focusing an optical image of the electrode pattern on a photoconductive layer, which is shown in Fig. 2-3(b). Although DEP is a rather flexible method of arraying cells, DEP

cell arrays are generally limited by several disadvantages. For example, the culture medium must have low conductivity, which limits the variety of experiments, since it limit the concentration and composition of ions in the culture medium. Additionally, DEP requires high potential electric fields, which can be damaging to the cells. To avoid such damage, a high frequency electric field is required, but it also increases the complexity of the system [28]. In addition, designing and fabricating an array of electrodes to manipulate the cells is never a simple task, since it requires elaborate circuit layout and control circuitry.

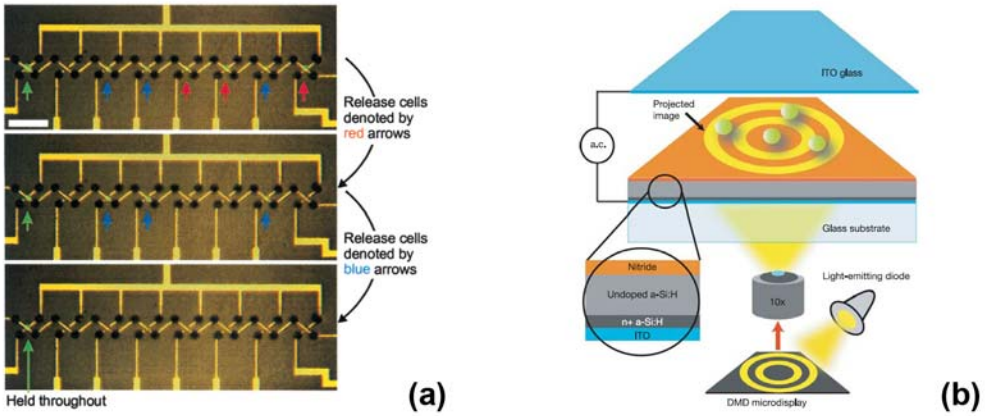

Figure 2-3 (a) Negative-DEP cell array is shown in [11]. Notice that each capture site can be activated and deactivated individually. (b) Illustration of the reconfigurable optical electrode of the DEP cell array developed by P. Chiou *et al.* [29].

Another method for cell arraying using electromagnetic interaction of the cells and their surroundings is the use of the optical tweezers array [14,31-32], shown in Fig. 2-4. Similar to the acoustic arraying technique, no physical structure is required to array the cells. Moreover, the cells can be manipulated while in an array arrangement [31-32], which adds flexibility to the system. Although the optical tweezers method is flexible, it is generally expensive. In addition, the cells to be manipulated by the optical tweezers must be transparent, and non-absorbing at the operational wave-length of the tweezers. Also, the cells must have a refractive index difference with the medium that they are

suspended in [20]. However, the major obstacle of this method is the power limit of the optical tweezers, which limits scalability of the cell array, and the endurance of the traps [1,20]. Thus, the combination of optical tweezers with other cell arraying techniques, such as hydrogel [33] and micro-wells [34], is explored to bypass the power limitation of the laser diode.

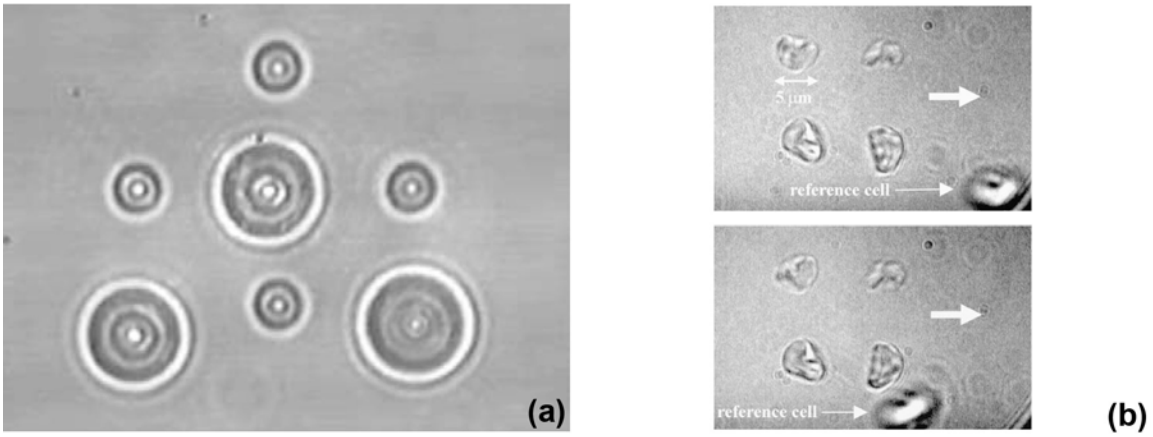

Figure 2-4 Optical tweezers cell arrays. (a) shows the experiment of arranging polystyrene beads of different sizes in an array configuration. (b) shows the manipulation of a 2×2 cell array.

In addition to DEP devices and optical tweezers, magnetic devices are also commonly used in cell manipulation. Researchers have been using Magnetic Activated Cell Separation (MACS) devices to extract magnetically labelled cells from a primary sample for decades. It is known that magnetic field has a minimal effect on cell viability [35,36]. The technique is also useful since a static magnetic field does not disturb the movement of ions in the culture medium (at low velocity) [36]. Therefore, it is suitable to use in conjunction with other electrophysiology analysis techniques. Unlike DEP and some hydrodynamic methods, the magnetic field does not induced trans-membrane voltage, joule heating or shear stress on the cell. Thus, it is suitable for prolonged immobilization of cells, and therefore ideal for long-term cell experiments such as cell function assays and rare event detection [10].

Recently, several research groups have fabricated devices that use magnetic fields to manipulate cells [37-38] and to organise cells into arrays [15,28]. These devices cover a range of different configurations. The most elaborate device is built by the group of Lee *et al*. [38], shown in Fig. 2-5(a). In their device, they have built an active magnetic cell manipulation array that consists of several arrays of micro-electromagnetic coils. Each micro-electromagnetic coil is controlled individually by the attached integrated circuitry, therefore, each coil can be turned on and off individually to move the cells to the exact location. The fabrication of this device is quite complicated due to the multi-layer micro-electromagnetic coils. Moreover, the layout of the accompanying control circuit also makes it difficult to scale up the array. Although this cell manipulation method can be turned into a cell arraying method by activating all coils at the same time, it is hard to scale up to achieve large scale cell array. In addition, such system would require a cooling system to be attached to the device, to keep the temperature of the culture medium at a survivable level for the cells. This makes the device less suitable for experiments that last for hours than other devices that do not generate heat during operation.

In order to avoid the complex design, fabrication and heating problems associated with micro-electromagnetic coils, other researchers have opted for an approach of using “off-chip” magnetization in combination with “off-chip” or “on-chip” passive magnetic elements. In the work by Kimura *et al*. [39], a block of laminated iron/aluminium is used as a field modulator for shaping the magnetic field to create a magnetic cell array. The field modulator block is composed of a series of alternating layers of iron and aluminium that measures 100 μm to 300 μm thick. Once magnetized, lines of **B-**field peaks will

appear on the surface of the modulator. The magnetized field modulator block is then placed under a Petri dish, and cells that are within the Petri dish are attracted to the **B**-field peaks, and hence form an array pattern. In a similar approach, Ino *et al*. [15] micro-machined an array of micro-pillars, shown in Fig. 2-5(b), that measured 100 μm × 100 μm × 300 μm each, and were situated 150 μm from each other. The device could be magnetized by using a block of permanent magnet, then, a peak of the **B**-field would appear on top of each micro-pillar. Cells that are cultured on a cover slip can then be arrayed by placing the cover slip on the magnetized block. At sufficiently low cell densities, a 2-dimensional single cell array is achievable, with close to a 50% success rate of having one cell on top of each pillar [15]. However, the thickness of the bottom of the cell container (coverslip) is limited to no thicker than 150 μm for both the laminated field modulator and the soft iron micro-pillars. This is because the magnetic field diminishes rapidly as the distance from the surface of the magnetized object increases. This effect is especially significant for micro-scaled magnetic elements. Moreover, the magnetization blocks are opaque, and would have to be removed before the cells can be imaged under a transmitted light microscopy system. However, if the magnetization block is removed, non-adherent cells types could drift out of their arrayed positions. Thus this approach is only suitable for adherent cell types.

Another magnetic array device has been created by Tibbe *et al*. [10], shown in Fig. 2-5(c). It is similar to the laminated field modulated block by Kimura *et al*. [39] in configuration, however, the nickel lines that are used for concentrating the field are deposited on the ceiling of the container. Thus, the container wall thickness limitation is eliminated since the passive magnetic elements are lying inside the cell container.

Moreover, both field strength and resolution is considerably improved, since the cells can get very close to the magnetic elements. Once magnetized, the cells will be pulled toward the edge of the nickel line, thus, aligning the cell in lines. Do *et al*. [40] also created a line array by electroplating permalloy pattern on the bottom of a micro-channel. The permalloy layer pattern is consisted of a pair of interdigitated combs, which were magnetized with an electromagnet such that the field lines were along the major axis of the fingers of the combs. Although effective, both of these methods are only capable of arranging cells in lines, specific position of cells on these lines is not controlled. In the work by Tanase *et al.* [28], permalloy ellipses are deposited on the surface of the device, shown in Fig. 2-5(d). Once magnetized, the cells will be drawn toward the tips of the ellipses, thus creating a 2-dimensional array. However, the density of the array is limited, since it was noted that bringing the ellipses closer together will cause the cells to clump together, thus forming rows of cells instead of an array of cells.

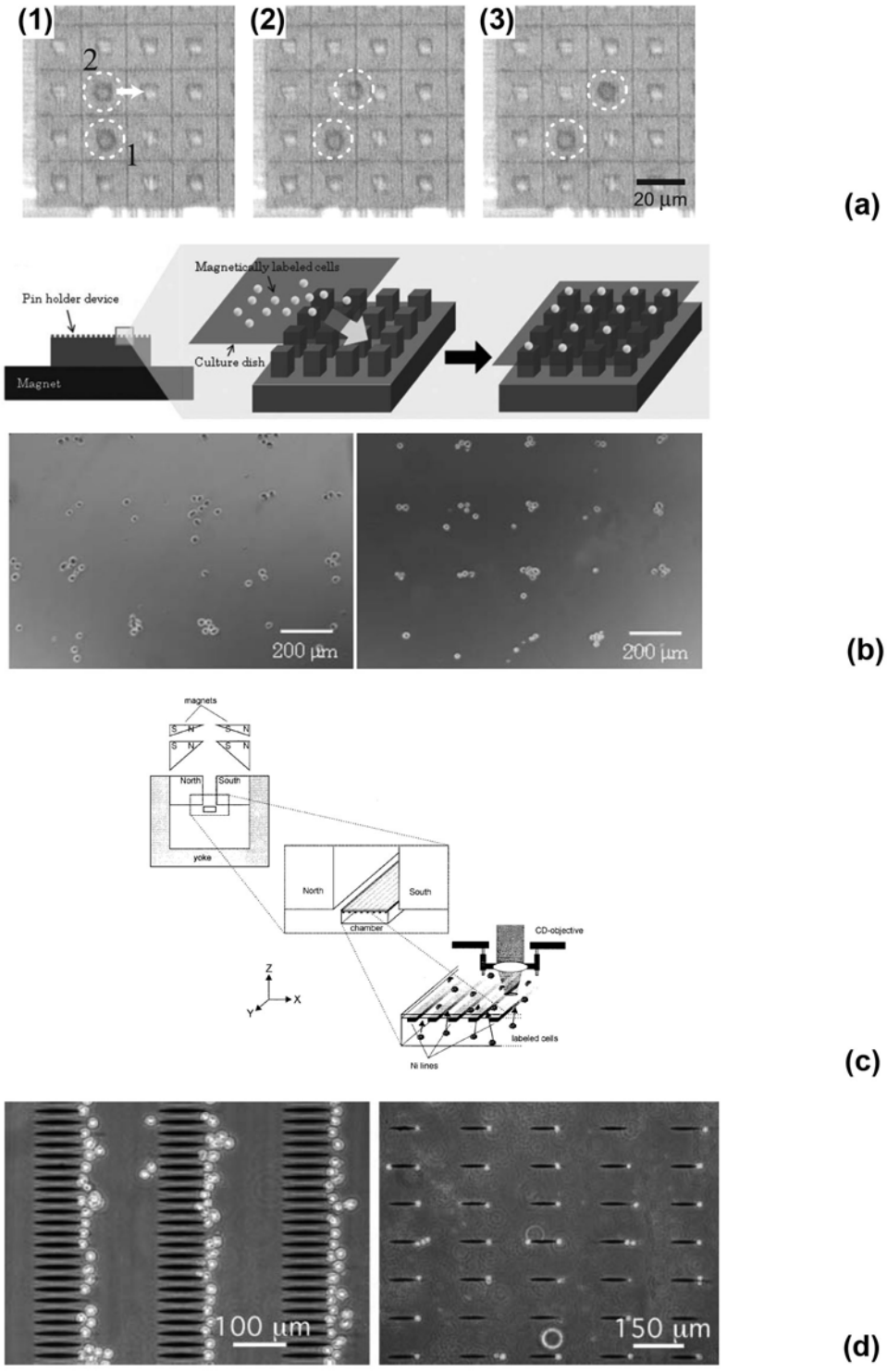

Figure 2-5 Various types of magnetic cell arrays. (a) Sequential images of the active micro-coil [38]. (b) Schematic of the soft iron micro-pillar block and cell array [15]. (c) The schematic of the device by Tibbe *et al.* [10]. (d)Another cell array with micro-permalloy ellipses [28].

Chapter 3 Basic Magnetism and Magnetic MEMS

Magnetic transducers are one of the most widely used of all transducers. Although the various magnetic transducers differ in appearance, size and construction, the working principles are all based on the physics of magnetism. The following section will briefly describe the basic theory of magnetism, and the related terminologies.

3.1 Basic Magnetic Terminology

The magnetic response of any material can be classified by several key magnetic properties of the material, namely the susceptibility, permeability, and coercivity. Under an applied magnetic field (**H**-field), the magnetic flux density (**B**-field) in free space is defined as:

$$\mathbf{B} = \mu_0 \mathbf{H} \qquad \textbf{eq 3.1}$$

Where μ_0 is the magnetic permeability of free space, which is a universal constant that defines how much magnetic flux can pass through space due to an applied field. When a piece of material is introduced into the applied field, the **B**-field is equal to the sum of the **B**-field in free space and the magnetization field (**M**-field):

$$\mathbf{B} = \mu_0 (\mathbf{H} + \mathbf{M}) \qquad \textbf{eq 3.2}$$

M-field in any material is defined by:

$$\mathbf{M} = \chi \mathbf{H} \qquad \textbf{eq 3.3}$$

Where χ is the susceptibility of the material, which measures the strength of the **M**-field within the material, under an applied **H**-field. Alternatively, the above equations can be rewritten into the following form:

$$\mathbf{B} = \mu_0 (\mathbf{H} + \chi \mathbf{H})$$
$$\mathbf{B} = \mu_0 (1 + \chi) \mathbf{H}$$

$$\mathbf{B} = \mu_0 \mu_r \mathbf{H} \qquad \textbf{eq 3.4}$$

Where μ_r is a dimensionless parameter that defines the magnetic permeability of the material compared to that of free space, thus it is called the relative permeability of the material.

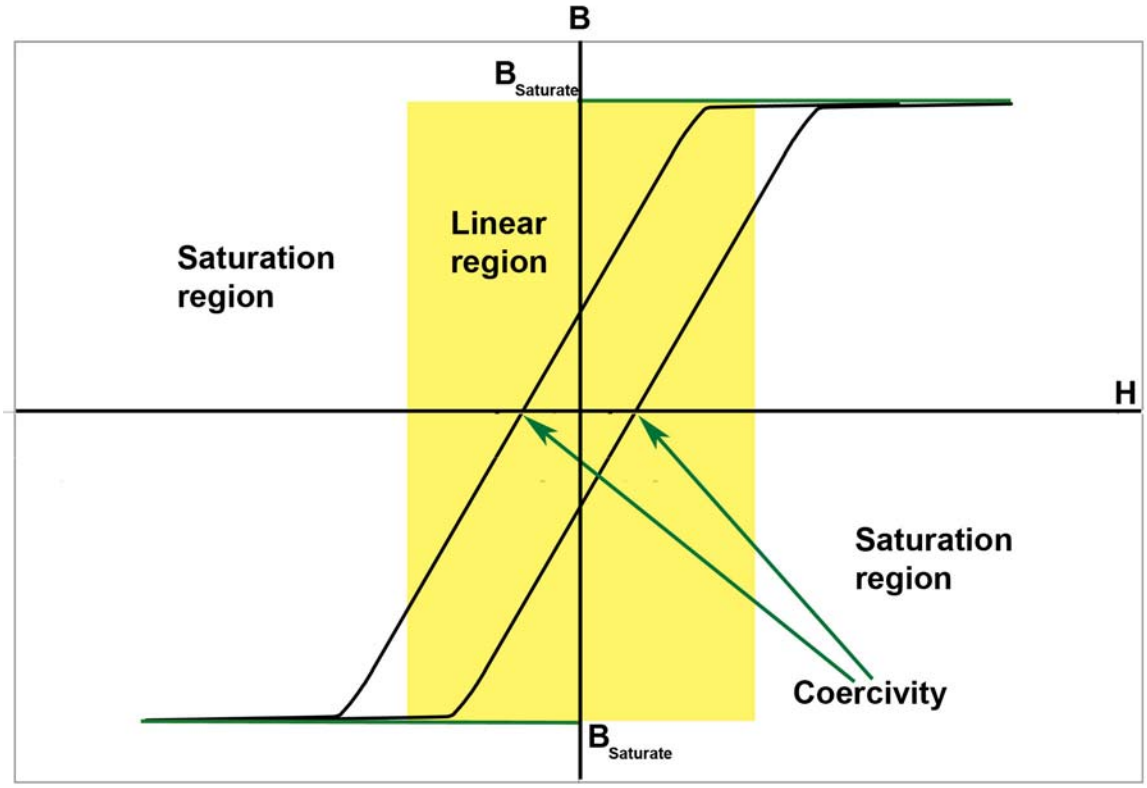

Figure 3-1 B-H plot of typical ferromagnetic materials. Note the linear region is highlighted in yellow.

In general, susceptibility and relative permeability are functions of the applied **H**-field and the temperature. Therefore a **B-H** plot is very useful when describing the magnetic properties of certain material. Fig. 3-1 shows a classic **B-H** plot of a typical ferromagnetic material. Notice that the magnetic response is not linear. Instead, it consists of a linear region at a low applied **H**-field and a saturation region at a high applied **H**-field. Some materials, such as ferromagnetic and ferrimagnetic materials,

exhibit hysteresis while demagnetized. Hysteresis refers to the phenomena where the **M**-field, as well as the **B**-field, does not return to zero even when the **H**-field is completely removed. An indication of the strength of the hysteresis effect is the coercivity, which specifies the magnitude of the **H**-field that would have to be applied, in opposite direction of the **B-**field, to completely cancel the **B**-field inside the material.

3.2 Magnetic Force on Magnetic Particles

Magnetic particles are widely used in the separation and sorting of biological cells. Extensive research has been done on the magnetic actuation force that can be achieved by these magnetic particles [41-45]. The magnetic force is generated by a non-uniformly distributed magnetic field. The exact derivation of the mathematical representation is lengthy and not easy to use. Fortunately, for sub-micron magnetic particles that are suspended in a weakly magnetic medium, the mathematical expression can be simplified to:

$$\mathbf{F} = \frac{1}{2\mu_0}\Delta\chi V \nabla \mathbf{B}^2 \qquad \textbf{eq 3.5}$$

Where $\Delta\chi$ is the difference in the magnetic susceptibility between the particles and the medium, V is the volume of the particle and **B** is the **B-**field. As shown in the above equation, magnetic force is proportional to the difference in magnetic susceptibility, volume, and the magnetic flux density field gradient. When suspended in a weakly magnetic medium, such as water, a piece of paramagnetic or ferromagnetic material will experience force in the direction of the gradient of the magnetic flux density field. A diamagnetic material in the same medium will experience force in the opposite direction. In other words, paramagnetic or ferromagnetic materials will be attracted toward the

maxima of the magnetic flux density field, while diamagnetic materials will be attracted toward the minima of the magnetic flux density field [36, 41-42].

3.3 Magnetic MEMS

Magnetic MEMS devices are usually used as transducers. This kind of actuation offers several advantages over other MEMS actuation technology. For example, they can provide large effective actuation distance, action without physical contact and absence of a high potential electric field [46-48]. These advantages also coincide with the requirements of cell manipulation. A number of fabrication techniques and materials are used for realizing magnetic MEMS devices. These techniques and materials are described in the following sections.

3.3.1 Magnetic Material in MEMS

Applications of magnetic materials in micro-devices are not new. Engineers have been using magnetic materials in micro-magnetic data storage devices, such as computer hard disks, for decades. A number of alloys and rare-earth materials have been developed for magnetic data storage applications. MEMS designers took advantage of these early developments and extended the use of these materials to other MEMS applications. In general, all materials respond to magnetic field to a certain degree. Depending on the behaviour of the material under an external magnetic field, magnetic materials can be classified into paramagnetic, diamagnetic, ferromagnetic, ferrimagnetic and anti-ferrimagnetic. This difference in behaviour is due to the structure of the material on the atomic and sub-atomic level, which is beyond the scope of this paper. Alternatively, materials can be loosely classified as weakly magnetic materials, soft magnetic materials

and hard magnetic materials based on the susceptibility and the coercivity of the material. The following sections will illustrate each class of materials.

3.3.1.1 Weakly Magnetic Materials

The majority of materials are weakly magnetic, which include both paramagnetic and diamagnetic materials. In general, materials of this class have an extremely low susceptibility, 10^{-6} to 10^{-1} in magnitude. Moreover, the B-H curve of materials of this type is purely linear, i.e. straight line with negligible hysteresis. Hence, they exhibit no saturation and zero coercivity. The only difference between paramagnetic materials and diamagnetic materials is the sign of their susceptibility. Paramagnetic materials have positive susceptibility (ranging from 10^{-6} to 10^{-1}), on the other hand, diamagnetic materials have negative susceptibility (ranging -10^{-6} to -10^{-3}), which makes the two types of material behave oppositely under an applied H-field.

3.3.1.2 Soft Magnetic Material

Soft magnetic materials are defined as materials that have high susceptibility and low coercivity. They are commonly used as core materials for electromagnetic coils for enhancing flux density. Since changing the magnetic polarity in these materials requires very little energy, these materials are ideal for power transmission, data read/write heads, actuators and sensors. Soft magnetic materials used in MEMS are usually alloys of nickel, cobalt and iron. For example, Ni80Fe20 permalloy is commonly used in the read/write head of hard disks [48]. The electrical, magnetic and mechanical properties of NiCoFe alloy vary based upon the alloy's composition. Designers will often balance the trade offs between electrical, magnetic and mechanical properties to get the optimal performance for a particular application. The relationship of the alloying content ratio in

NiCoFe alloys and the major material properties are reported by Myung et. al. [49]. Soft magnetic alloys that have other alloying agents are reported by Andricacos and Robertson [50]. Alloys with up to 2.4 times the saturation magnetization of Ni80Fe20 permalloy are reported in their paper.

3.3.1.3 Hard Magnetic Material

Compared to soft magnetic materials, hard magnetic materials have a much higher coercivity, thus they are harder to demagnetize. They are used in large force micro-actuators, since they are capable of providing much higher flux density than an electromagnetic coil at the same size [48]. Moreover, they are used in applications where a large continuous field is needed, since no power source is needed for sustaining the field from a permanent magnet. Depending on the alloying ratio, it is possible to obtain hard magnetic NiCoFe alloy. Materials such as CoPt alloy, FePt alloy, and rare earth compounds have been investigated and have given promising results in hard magnetic applications [49].

3.3.1.4 Super-paramagnetic Materials

As mentioned in previous sections, ferromagnetic and ferrimagnetic materials usually exhibit hysteresis magnetization after the H-field is removed. In general, hysteresis effect will become more intense as the particle decreases in size, however, there is a size below which the hysteresis effect will drop to zero. Materials exhibiting this property are said to be super-paramagnetic. Materials that exhibit super-magnetism are, in general, small particles that are smaller than the width of the wall of a magnetic domain. Because of their size, each particle is essentially a single magnetic domain particle. In the absence of an applied H-field, the orientation of the magnetic domain is random due to the thermal

excitation. Thus, super-paramagnetic particles exhibit zero coercivity like the paramagnetic materials. However, under an applied H-field, the particles will exhibit a much higher susceptibility than paramagnetic materials, until they reach saturation.

3.3.2 Permalloy

Permalloy of various formulations has been used in many different applications since the early 20th century. Its magnetic properties have been investigated by many researchers over the past. Traditionally, permalloys are have been prepared thermally, since the magnetic properties of these alloys are affected by the different forming processes, such as rolling processes and heat treatment, in addition to alloy composition. This was done to control the resulting grain size and the microscopic structure of the materials.

In recent years, permalloys have also been applied to MEMS devices, due to their superb mechanical properties, anti-corrosion properties and magnetic properties. Since MEMES devices are the extremely small in size, permalloy features are usually fabricated by an electroplating process or by vacuum deposition, instead of the traditional thermal process. As a consequence of these new fabrication methods, these alloys have drastically different magnetic properties from those of the thermally prepared macro-scaled permalloys. This is due to the differences in their size and micro-structure. For example, the magnetic permeability of commercial permalloys is on the order of 10^4 [51], while permeability of micro-scaled electroplated permalloys is in the range of 500-1000 [52]. In comparison with other soft magnetic materials that are commonly used in MEMS, such as Orthonol (Ni51Fe49) and CoFeCu alloy, permalloys have a lower coercivity and higher permeability, though the saturation magnetization is lower than the

other two alloys [53]. In addition, it has been reported that the magnetic properties of permalloys are also affected by film stress, grain size, crystal structure, surface roughness and film thickness [49].

3.3.3 Fabrication of Magnetic MEMS

There are a number of ways to fabricate magnetic MEMS devices, including electrodeposition, vacuum deposition and screen printing. The most common fabrication method is with an electrodeposition process. Electrodeposition was originally developed for the magnetic data storage industry for electroplating permalloy (soft magnetic alloy of nickel and iron) onto the micro-coil of a data read/write head. The electrodeposition process consists of a number of steps. Firstly, a conducting substrate is submerged in an electrolyte solution that contains the ions of the material that is to be plated onto the substrate. Next an electrode is submersed in the electrolyte, and an electric potential is applied across the substrate and the electrode. This causes an electric current to flow through the electrolyte to the substrate, which causes the ions in the solution to be deposited onto the surface of the substrate. This technique is very versatile, and is capable of fabricating structures with very fine features and high aspect ratio [54]. This process also works at a low temperature (close to room temperature) and hence makes it compatible with integrated circuit fabrication. In addition to soft magnetic alloys, it is also possible to use electrodeposition to fabricate hard magnetic materials, such as CoPt and FePt alloy. Recently, researchers have successfully introduced rare-earth hard magnetic particles into the electroplated metal matrix by a technique called Magnetic Composite Electroplating (MCE) [55]. This technique is capable of producing a much stronger permanent magnet due to the high coercivity of the rare-earth particles.

Another method for depositing magnetic materials onto MEMS device uses is the use of vacuum deposition. This includes processes, such as evaporation, sputtering, molecular beam epitaxy crystal growing and chemical vapour deposition [56]. Generally, these types of processes have higher process temperatures and slower deposition rates than electrodeposition. These techniques are capable of making magnetic layers with excellent magnetic properties. However, due to their high process temperatures, vacuum deposition has compatibility issues with other micro-fabrication process. Also, the layer thickness of vacuum deposition processes is usually limited to 2 microns, due to the very slow deposition rates.

An alternative low costs thick layer fabrication process, is based upon screen-printing of magnetic polymers [53]. This method involves printing polymers that contain magnetic particles onto the chip surface through a patterned screen. It is capable of producing layers of over 100 microns in thickness, in a relatively short processing time. However, the minimum feature size is limited to 100 microns. Like electrodeposition, the process temperature of screen printing is relatively low, thus it is compatible with most micro-fabrication processes.

3.3.4 Electroplating Permalloy

With accurate control of electroplating process parameters, the electroplated alloy composition can be controlled precisely. Electroplating can yield magnetic material layers that are up to several hundred microns thick. Moreover, the low process temperature of electroplating also makes the process preferable for integration with other integrated circuit fabrication process [54]. Generally, electroplating is used for depositing layers of pure (single element) metals. However, alloy deposition is possible with a

process called anomalous codeposition. To achieve nickel-iron anomalous codeposition, the plating bath is formulated in such a way that the more preferable nickel deposition is inhabited, while at the same time promoting the deposition of the less noble iron [57]. The composition of the resulting alloy layer is thus mainly controlled by the bath composition, current density and agitation rate. A number of researchers [52-53, 58-62] have investigated the effect of each of these parameters. Generally, the iron content increases with an increase in the agitation rate, regardless of the bath composition. The iron content will increase with an increase in the current density for low current densities. However, iron content falls continuously after peak the iron content is reached at a specific current density. Moreover, the presence of boric acid and dissolved oxygen levels, can affect the layer composition under different conditions [58]. Like other material deposition methods, the electroplating process is often used in combination with photolithography to fabricate a patterned layer. In electroplating process, the wafer is often masked with photoresist, thus only the exposed area will be electroplating. In comparison with directly platting on patterned electrodes, through mask electroplating technique would yield better layer evenness due to the consistent conductivity across the entire substrate. However, slight layer unevenness is still observed in through mask electroplated layer due to the edge effect on the electric field [54,57]. Since the path to the electrode is blocked, the electric field lines near the edge of the photoresist mask will bunch up and form a region of high current density. Therefore, the thickness of the layer around the edges is often higher than the rest of the layer, and the composition may be different. The edge effect can be minimised in a few ways, such as, using a bath recipe

that is less sensitive to change in electric field, designing the geometry to accommodate the edge effect, using a "frame mask" to reduce the edge effect [47].

3.3.5 Magnetization of Magnetic MEMS

The most direct way to magnetize a micro-structure is to fabricate micro-magnet on the surface of the device. This type of structures generally allows very high field resolution. Permanent magnets are usually used because of their simplicity, since no electrical connections are needed, and their high magnetic field strength. However, for certain application where active control of the magnetization is required, electromagnets are favourable.

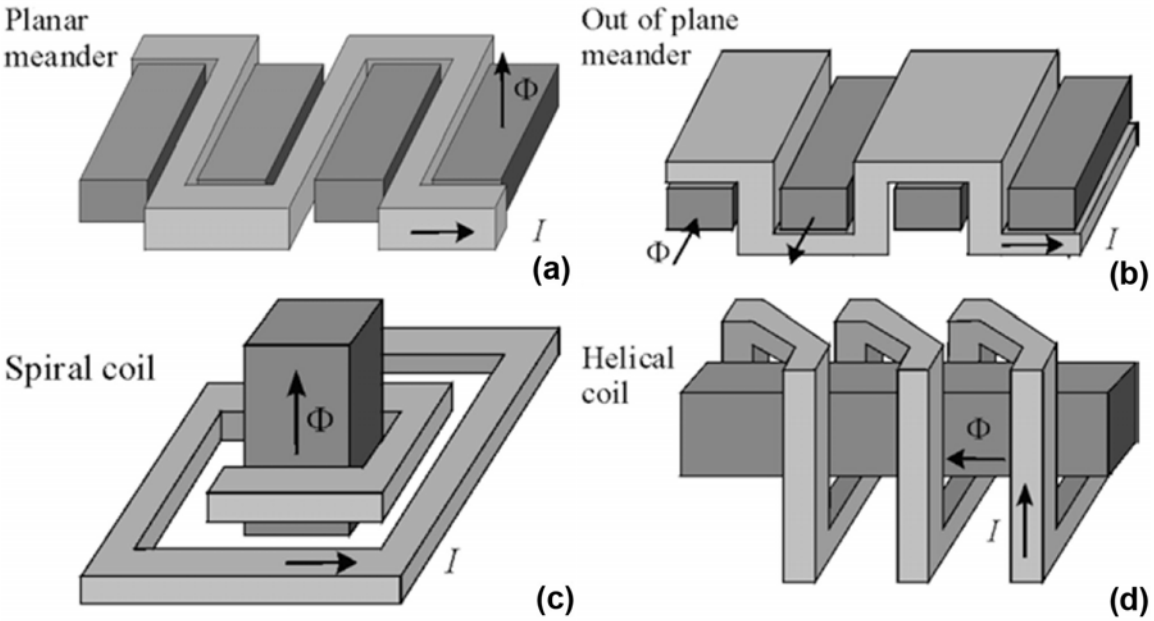

Figure 3-2 various form of micro-electromagnets.

Micro-scaled electromagnets can be fabricated in a number of ways, as shown in Fig. 3-2. They usually consist of electrical current conductors (Aluminum, Copper or Gold) and a soft magnetic core (usually Permalloy), encapsulated in insulating materials (SU8 polymer, polymide etc.). The most straight forward realization of an electromagnet is a "helical coil" as shown in Fig. 3.2(d) [63]. Micro-helical coils usually consist of a

soft magnetic core deposited in the middle of a multilayer conductor structure. This results in the closest approximation to a macro-scaled helical coil electromagnet, however, the fabrication of this type of coil is time consuming and expensive, due to the numerous layer required for fabrication. A simpler design, called a “meander coil”, has a set of serpentine electrical conductors wound around a serpentine soft magnetic coil as shown in Fig. 3.2(a-b) [63]. Meander coils are simpler to fabricate, and offer similar performance to the helical coil [63]. The simplest coil designs are spiral coils as shown in Fig. 3.2(c) [63]. Spiral coils can be made in one layer at the minimum, and are thus cheaper and easier to fabricate than the other two designs. However, the spiral coil produces a weaker magnetic field than the other two. Although, this can be solved by stacking up a number of coils, stacking up the spiral coil will add process time and complexity, thus making the device more expensive. Although micro-electromagnets offer high field resolution and active field strength control, the design of the current conduction path tends to make the design of these devices complicated. Additionally, the conductors may be required to carry relatively high current, and hence generate a lot of heat during operation. This becomes a problem when temperature control is important for the device.

Another way in which to design micro-magnetic structures is to make use of magnetic field that is generated “off chip”. In a device that uses “off chip” magnetization source, macro-scaled electromagnets or permanent magnets are situated off the chip, and generate magnetic flux in close proximity to the chip. This magnetic flux can be guided into the micro-magnetic structure to the desired locations, by creating a suitable soft magnet pattern on the substrate. Such a concept is realized by Do *et al*. [40] in their

design of a magnetic particle separator. In their design, the electromagnets are situated off chip, and the external magnetic flux is guided into the flow chamber by a permalloy pattern on the substrate. This type of design is much simpler than micro-electromagnets, since it does not need a current conducting path. Moreover, no electrical heating will occur, thus the temperature control problem can also be eliminated.

3.4 Immunomagnetic Technology

Biological cells are generally diamagnetic [64], with a few exceptions such as red blood cells (erthrocytes) and magnetotatic bacteria. Thus the $\Delta\chi$ term in Eq. (1) is extremely small, and hence the magnetic force in response to a magnetic field is extremely small. In order to manipulate biological cells with magnetic force, immunomagnetic labels are often attached to cells to increase the difference in magnetic susceptibility between the cells and the buffer solution. Immunomagnetic labels have been used for Magnetic Activated Cell Separation (MACS) for decades. Its effectiveness makes it the technology of choice for many cell researchers. This technology has recently been used by researchers to manipulate individual cells. Its effectiveness is shown by Ino *et al*. [15] and Lee *et al*. [38]. Immunomagnetic labels usually consist of two parts, the antibody and the magnetic particles. The following sections will illustrate the two parts respectively.

3.4.1 Immuno-labelling

Immuno-labelling is a common process used in cell separation and sorting. Using this labelling technique, researchers can artificially introduce fluorescence, magnetic and electric properties to a specific population of cells. The labelling process is a result of the chemical interaction between the antibody binding site on the surface of the cell and the

antibody on the label. When the appropriate antibody binding site and the antibody meet each other, a chemical bond will form, which allows the labels to attach to the cell membrane [65]. The number of labels that can be bonded to a cell is characterized by:

$$ABC = n\theta\lambda \qquad \textbf{eq 3.6}$$

Where n is the number of receptors or antibody binding sites, θ and λ are the parameters specific to the label used. The product of these three parameters is commonly referred as the Antibody Binding Capacity (ABC) [64]. In some cases, secondary labelling maybe added to the primary labels. In these cases, the total number of binding capacity is multiplied by [64]:

$$\psi = n_2\theta_2\lambda_2 \qquad \textbf{eq 3.7}$$

3.4.2 Types of Magnetic Particle

The second part of the immunomagnetic label is the magnetic particle that is conjugated to bind to the antibody. Based on the size the magnetic particles, they can be classified into one of three categories:

1. Particulate (1-5 microns)
2. Colloidal (on the order of 100 nm)
3. Molecular (on the order of 10 nm)

The first two types are commercially available, while molecular particles are only available in research laboratories [41].

The magnetic force exerted on the particle, as described by eq. 3.5, is proportional to the volume of the particle. Thus the force that can be generated by a single particulate label is the highest among the three types. However, the number of labels that can be attached onto the cell membrane is inversely proportional to the size of the label. Fig. 3-3 shows a plot of the maximum number of labels allowable on a cell, for different label

sizes. Note that the number of colloidal labels that can be coated onto a given cell is 2 to 3 orders of magnitude higher than that of the particulate labels. As McCloskey *et al*. [64,66] showed in their experiments, the number of particles that are attached to the surface of a cell does not increase linearly with the number of receptors when it is approaching the geometrical limit. However, the particulate labels are still capable of generating higher force overall, since a particulate label can generate force that is 4 to 5 orders of magnitude larger than that of the colloidal labels due to the size difference. Although particulate labels are capable of generating higher force, this force may be strong enough to detach the label from the cell, due to the limit of the strength of the antibody-receptor complex. In more extreme cases, the force may even rupture the cell due to the enormous stress that can be created within the membrane [64]. The maximum force has been determined to be between 10 pN and 80 pN in the experiments performed by Orsello *et al*. In addition, if secondary labelling is used, the maximum force limit will be reduced by 85% [65].

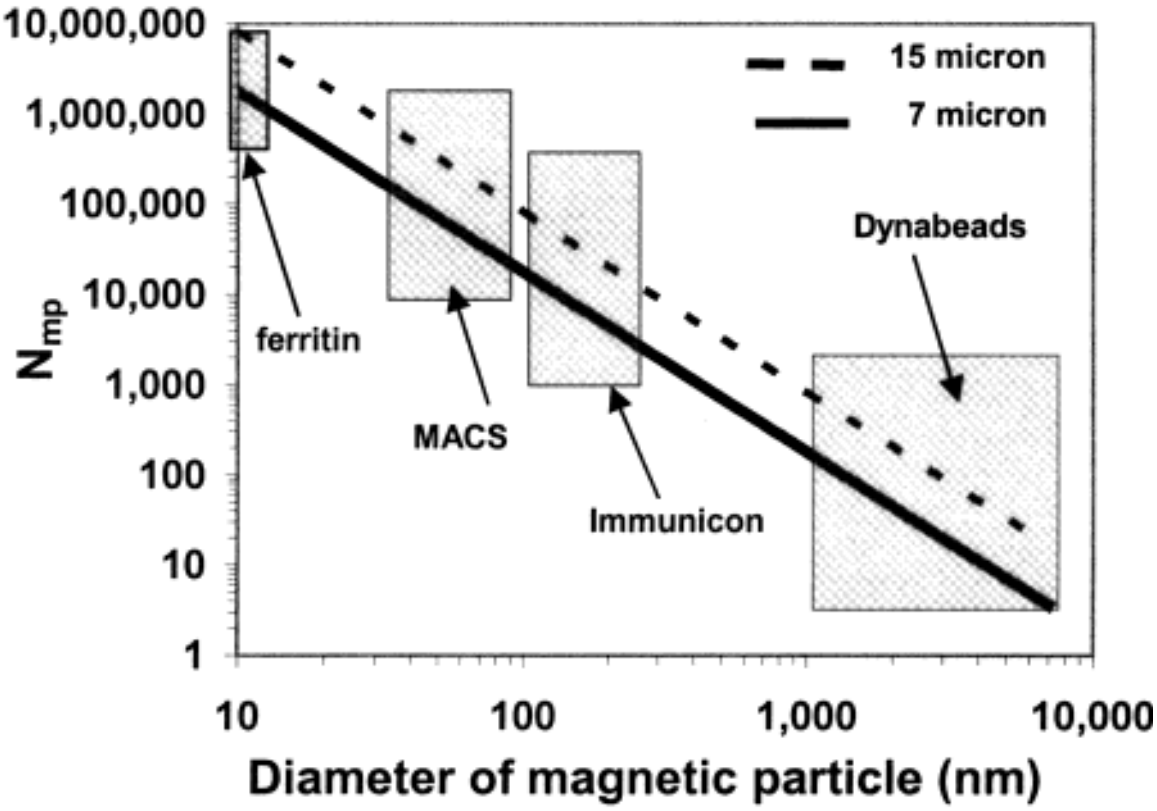

Figure 3-3 Logarithmic plot of the maximum number of magnetic particles that can bind to the surface of a spherical cell (N_{mp}) based on the geometric estimation. The solid line represent the relationship between the diameter of the magnetic particle and N_{mp} of a 15 µm wide cell (15 µm in diameter). The dashed line represent the relationship between the diameter of the magnetic particle and N_{mp} of a 7 µm wide cell (7 µm in diameter). The size range of several commercially available magnetic particles is highlighted in the diagram [64].

Chapter 4 MSCMA

Various types of immunomagnetic technologies have been used for cell enrichment and isolation for many years. The simplest method is to immobilize labelled cells using a high gradient magnetic field, while rinsing the samples. In this way, the unlabelled cells will be rinsed away while the labelled cells are held in the container by the magnetic field. A more sophisticated machine developed by Zborowski *et al*. [67], can separate magnetic particles in a continuous stream by a radial magnetic field gradient, thus, increasing the throughput from the traditional batch method. The separation method developed by Todd *et* al. [68] can separate particles according to their magnetophoretic mobility (mobility of particles under a given magnetic field) by varying the strength of the applied field.

In recent years, researchers have been looking into the possibility of combining the idea of immunomagnetic technology with MEMS technology. Thus far, devices have been made for separating magnetic particles and manipulating magnetic particles [45]. These devices have also been proven to be effective for bulk cell separation and individual cell manipulation. However, not many researchers have tried to combine the concepts of cell separation and precision positioning of cells. The purpose of the Magnetic Single Cell Magnetic Array (MSCMA) as proposed in this thesis is to bridge this gap. In other words, the idea of the MSCMA is to develop a device that can separate magnetically tagged cells from the bulk population of cells, and also array them on a surface after separation. The cells can then be individually evaluated and identified by their location on the array. To achieve this, the MSCMA must employ a method to produce **B**-field peaks of sufficient magnitude, at pre-designed locations. In doing so,

capture cells can be positioned at these pre-designed location. The theory, design issues and the design will be discussed in the following sections.

4.1 Forces on Cells and Velocity of Traveling Cells

A magnetically labelled cell that is moving through a medium in a magnetic field will experience four different forces:

1. Gravity
2. Buoyancy
3. Hydrodynamic drag
4. Magnetic force

Due to the small Reynolds number associated with a micro-scaled biological cell, the hydrodynamic drag on a cell can be modeled as Stokes drag on a sphere, which can be estimated:

$$\mathbf{F}_{drag} = -6\pi\mu R\mathbf{v} \qquad \textbf{eq 4.1}$$

Where $\mathbf{v}$ is the cell velocity, R is the radius of the cell, and μ is the viscosity of the fluid. By combining the terms to the left of $\mathbf{v}$, eq. 4.1 can be rewritten as:

$$\mathbf{F}_{drag} = -D\mathbf{v} \qquad \textbf{eq 4.2}$$

where D is the drag coefficient of the cells. The magnetic force acting on a cell is given by:

$$\mathbf{F}_{magnetic} = ABC\mathbf{F}_b \qquad \textbf{eq 4.3}$$

where ABC is the antibody binding capacity, $\mathbf{F}_b$ is the force on a single magnetic particle. $\mathbf{F}_b$ can be calculated from eq. 3.5 i.e.:

$$\mathbf{F} = \frac{1}{2\mu_0}\Delta\chi V\nabla\mathbf{B}^2 \qquad \textbf{eq 3.5}$$

At any given time, the motion of a magnetically labelled cell in a magnetic field is governed by Newton's second law:

$$ma = \mathbf{F}_{gravity} + \mathbf{F}_{buoyancy} + \mathbf{F}_{drag} + \mathbf{F}_{magnetic} \qquad \textbf{eq 4.4}$$

By combining $\mathbf{F}_{gravity}$, $\mathbf{F}_{buoyancy}$ and $\mathbf{F}_{magnetic}$ into the same term, eq. 4.4 becomes:

$$ma = \mathbf{F} + \mathbf{F}_{drag} \qquad \textbf{eq 4.5}$$

Therefore:

$$m\mathbf{v}' = \mathbf{F} - D\mathbf{v}$$

Solving this differential equation for **v** gives:

$$\mathbf{v} = e^{\int \frac{-D}{m} dt} \left(\int e^{\int \frac{D}{m} dt} \frac{\mathbf{F}}{m} dt + C \right) \qquad \textbf{eq 4.6}$$

If it is assumed that the **B**-field is static and the gradient of the **B**-field is linear, then, **F** is constant with respect to *t*, since gravity and buoyancy are both constant. Therefore:

$$\mathbf{v} = e^{\frac{-D}{m}t} \left(\frac{\mathbf{F}}{m} \frac{m}{D} e^{\frac{D}{m}t} + C \right)$$

Which is simplified to:

$$\mathbf{v} = e^{\frac{-D}{m}t} \left(\frac{\mathbf{F}}{D} e^{\frac{D}{m}t} + C \right) \qquad \textbf{eq 4.7}$$

If it is assumed that the cell is starting from a stationary state, then **v**=0 at time *t*=0, and hence we can solve for the constant to get:

$$C = \frac{-\mathbf{F}}{D}$$

Substituting this back into eq. 4.7, the expression becomes:

$$\mathbf{v} = e^{\frac{-D}{m}t} \left(\frac{\mathbf{F}}{D} e^{\frac{D}{m}t} - \frac{\mathbf{F}}{D} \right)$$

Which is simplified to:

$$\mathbf{v} = \frac{\mathbf{F}}{D}\left(1 - e^{\frac{-D}{m}t}\right) \qquad \textbf{eq 4.8}$$

Thus, when a static **B**-field with linear gradient is applied to a stationary cell, the cell will move at the velocity given by eq. 4.8 at any given time. As time approaches infinity, the velocity of the cell would approach its terminal velocity $\mathbf{v}_0$, where $\mathbf{v}_0$ is given by:

$$0 = \mathbf{F} - D\mathbf{v}_0$$

$$\mathbf{v}_0 = \frac{\mathbf{F}}{D} \qquad \textbf{eq 4.9}$$

From a stationary position the time that the cell will take to reach 99% of $\mathbf{v}_0$ is given by:

$$0.99\frac{\mathbf{F}}{D} = \frac{\mathbf{F}}{D}\left(1 - e^{\frac{-D}{m}t}\right)$$

$$0.99 = 1 - e^{\frac{-D}{m}t}$$

$$t = -\frac{m}{D}\ln 0.01$$

$$t \approx \frac{4.6m}{D} \qquad \textbf{eq 4.10}$$

Thus, regardless of the magnitude of the magnetic force, the time required for the cell to reach its terminal velocity only depends on the ratio between its mass and its drag coefficient, and thus, its radius. For cells in the size range of 5 to 30 microns, the mass of the cell is in the order of 10^{-15} kg (Assuming the density of cells is similar to the mass of water), and the drag coefficient D is on the order of 10^{-7}. Thus the acceleration time for the cell to reach 99% of the terminal velocity is in the range of 10^{-8} to 10^{-7} seconds. In other words, the cell will accelerate to the terminal velocity in the medium very rapidly, and will move at the terminal velocity during most of its travel. Thus, velocity of the cell at any given time can be defined as:

$$\mathbf{v} \approx \frac{\mathbf{F}}{D} \qquad \textbf{eq 4.11}$$

If the effect of gravity and buoyancy is ignored, the velocity of the cell is strictly proportional to the instantaneous magnetic force on the cell, and the cell velocity equation becomes:

$$\mathbf{v} \approx \frac{\mathbf{F}_{magnetic}}{D} \qquad \textbf{eq 4.12}$$

Therefore, the velocity of a cell, like the force, is directly proportional to the gradient of the **B**-field. As a result, cells that are labelled with super-paramagnetic particles will be attracted toward and trapped at the peak of the **B**-field.

4.2 MSCMA Design Consideration

In addition to the profile of the **B**-field on the MSCMA, several other design issues should be considered in the early design stage. First of all, the MSCMA needs to be compatible with current experimental equipments. Meyvantsson *et al*. [69] has suggested that the incompatibility of equipment has hindered the use of MEMS devices in life science research. For example, the fluid delivery system is the major hurdle in the application of micro-fluidic systems in life sciences. The proposed MSCMA must be compatible with various biological experimental equipments, such as the microscopy system, the cell manipulation system and the incubation system. Many microscopy systems that are used in life science have transmitted light configuration. Therefore, the MSCMA device has to be transparent in order to be compatible with these types of imaging systems. In addition, many cell manipulation systems and incubation systems require an open cell array chamber design to allow access to the cells. Having an open cell array chamber will allow the use of, for example, micro-injection pipette manipulator for cell injection [70] and CO_2 perfusion system for incubation of mammalian cells.

The MSCMA must also be biocompatible for experiments using live cells. Therefore, the cell array chamber must be constructed from materials that present no toxicity to the cells, so that the cells can survive for the duration of the experiment and respond normally to the applied stimuli. In order to obtain biocompatibility, Bio-MEMS usually use biocompatible glass, SU-8, Polydimethylsiloxane (PDMS), and polystyrene in the area that comes into direct contact with the cells. Additionally, enclosing the magnetic micro-structures with these materials also protects the metal components on the device from corrosion and other chemical reactions with the buffer solution.

In addition, fabrication constraints also need to be considered during the design stage. It would be meaningless to propose the best possible theoretical design, if it is impossible to be fabricated. Typical considerations for the fabrication of MEMS devices include:

1. Materials should be chosen carefully to ensure compatibility between all materials on the device, and compatibility between the device and other peripheral equipments.
2. Deposition methods should be chosen to ensure the good quality of the deposited materials, such as good adhesion and low residual stress. Moreover, deposition method of each step must not damage the rest of the material on the device.
3. Patterning methods should be chosen to ensure compatibility with every other fabrication steps, yet still give good resolution so that the performance of the device would not be affected.

While designing the MSCMA, the fabrication constraints were taken into consideration by both picking the right fabrication process, and designing the MSCMA within the constraints of the selected fabrication process.

4.3 Design of MSCMA

In order to achieve cell arraying, an array of local maxima in the **B**-field has to be generated on the surface of the MSCMA. So that the gradient vectors of the **B**-field, as well as the force and velocity vectors of the cell, are pointed toward the **B**-field maxima in the array. In addition to the ability of creating the **B**-field with the desired profile, the MSCMA must also satisfy several performance requirements:

1. Activation of the MSCMA should be controllable, so that the operators can ensure an even distribution of cells in suspension before activating the device. Moreover, deactivation of the device could allow for cells to be removed and collected.
2. The MSCMA must allow for integration with a transmitted light microscope, as it was discussed previously that transmitted light microscope is a widely use and important equipment for cell biology research
3. The MSCMA design should allow for a high density of cell capture sites. Since millions of cells are usually examined in typical cell experiments, the higher the cell density on the device the smaller the device can be, thus easier to handle.

The next sections will describe the design of the MSCMA.

4.3.1 Device Magnetization

Magnetization of magnetic MEMS devices can be done in a number of different ways, as was described in Section 3.3.5. This includes the use of either electromagnets or

permanent magnets, which can be either micro-magnet that are fabricated directly on the devices, or macro-magnets that are placed around the devices. One of the original ideas of creating the MSCMA was to put micro-permanent magnets on the surface of the cell containers. When cells are introduced into the container, they would be drawn toward these micro-magnet. However, a device of this configuration may not be deactivated when needed, since the permanent magnets are fixed on the surface of the containers. In contrast, using micro-electromagnets or soft-magnets would allow the operator to deactivate the magnetic field when needed.

Fig. 4-1 shows four possible configurations using either micro-electromagnets or soft-magnets. Micro-electromagnets can be a powerful tool for this application, since they may be actively controlled to adjust the strength of the magnetic field and could be used for cell manipulation [38]. However, the electrical connections required to construct an individually addressable array of micro-electromagnets would be highly complex, and due to the number of conductors required, may prevent its use with a transmitted light microscope. Moreover, the heat dissipated from the conductors of the electrical current in the micro-electromagnet, may cause problems with biological cells. Therefore, such a design would need some type of cooling system to dissipate the heat. Therefore, complexity of the system is further increased.

On the other hand, using micro-sized soft-magnets provides a design alternative of MSCMA. The most straight forward configuration would be to place the soft-magnets directly under the cells and magnetize the soft-magnets during operation, as shown in Fig. 4-1(b). However, with this configuration, the use of a transmitted light microscope is still not possible, since the structure would be completely opaque. Therefore, an

alternative configuration that would permit the transmission of light has to be considered for the design of the MSCMA that is presented here. Other researchers have shown that magnetic-based cell arrays can be designed to be compatible with a transmitted light microscope. This can be done by properly arranging the soft magnetic materials and orienting the magnetization field so that they would not obstruct the light path. For example, in other reported magnetic cell arrays, researchers use lines of magnetic elements [10,40] on the surface of a cell container to create a local non-uniformity in the **B**-field. Therefore, cells that are magnetically labelled will be drawn toward the local maxima of the **B**-field. Both devices were proven to be effective in aligning cells and magnetic bead into lines, however, they were incapable of position the cells at the pre-defined locations along the lines. In an alternative approach, Tanase *et al*. [28] fabricated permalloy ellipses on the substrate instead of lines. This resulted in cells that are collected at either end of the major axis of the ellipses, thus, creating a 2-dimensional array. However, the device used by Tanase *et al*. requires that the cells are labelled with nickel nano-wire instead of the super-paramagnetic immunomagnetic labels. Since the nano-wire carries a small remanent magnetization, it acts like a nano-scaled permanent magnet. Therefore, the nano-wire will tend to align itself along the major axis of the permalloy ellipses, and attach to the ellipses with a tip to tip configuration. However, super-paramagnetic immunomagnetic labels would react quite differently if they were used with the permalloy ellipses. Do *et al*. [71] showed that the particles are collected around the edge of the permalloy island instead of a specific location like the nano-wire. In order to achieve the desired performance specification, some preliminary designs of the MSCMA are investigated.

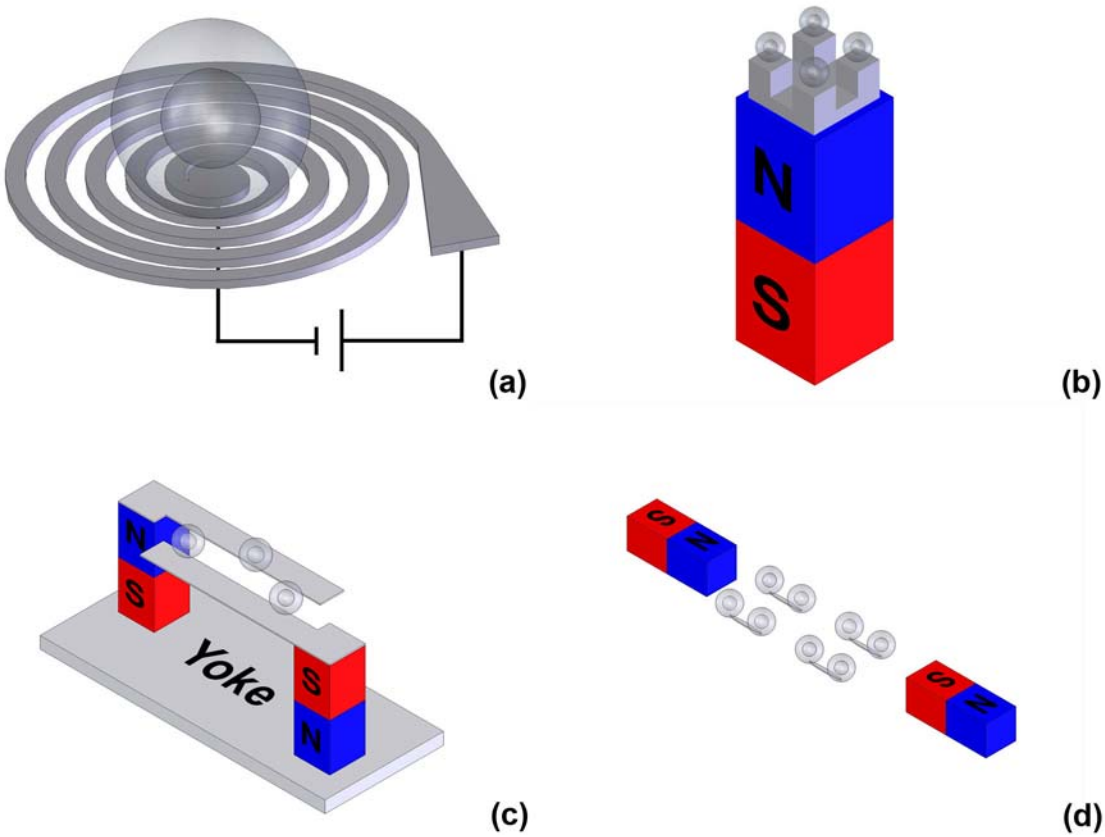

Figure 4-1 different previously reported magnetic cell trap configurations. (a) Illustration of the active micro-coils configuration by Lee *et al.* [38]. (b) Illustration of passive soft magnetic micro pillars by Ino *et al.* [15]. (c) Illustration of passive soft magnetic interdigitated comb by Do *et al.* [40]. (d) Illustration of passive soft magnetic micro ellipses by Tanase *et al.* [28].

4.3.2 Overall Configuration

Given the performance requirements described in the previous sections, the initial proposed design of the MSCMA, shown in Fig. 4-2, was investigated. This design consists of a modified permalloy interdigitated comb. This design was an improved variation of the permalloy comb design of the Do *et al.* [40]. The proposed improvement uses "tooth" like features, which are spaced at regular intervals along the comb, as shown in Fig. 4-2(a). The idea was to use these tooth features to channel the magnetic flux at to their tips, and hence create an array of points of **B**-field maximum. In this configuration,

the poles of the external excitation magnet are sitting at the two flux collection pads at either end of the combs. To complete the magnetic circuit, the magnetic flux must travel from one of the poles to the other pole on the other magnet. Since the magnetic permeability of the permalloy is higher than that of the surrounding medium, the magnetic flux will travel from the pole of one of the magnet to the finger of the comb structure, then jump across the gap into the comb of the other half of the structure, and finally into the pole of the other magnet. As Fig. 4-2 shows, tooth shaped pattern is created on either side of the permalloy comb finger. The hypothesis was that since the smaller gap between each pair of tooth features created an easier pathway for the magnetic flux to pass through, the majority of the flux will cross from one comb to the other at the locations near the tooth features. As a result, a local **B**-field maximum is formed at the gap between each pair of tooth features on either side of the magnetic circuit. To verify this hypothesis, Finite Element Method was used to evaluate the magnetic field around the device during operation. Fig. 4-3(a) shows an early FEM model used to confirm this phenomenon. However, it was realized that the simulations assumed linear behaviour of the permalloy was not an accurate representation. Therefore, the FEM model was adjusted to account for the non-linear permeability of the permalloy, which resulted in the profile of the **B-**field becoming drastically different in comparison with the linear model. In the non-linear model, as shown in Fig. 4-3(b), the permalloy became saturated by the external field, and the simulation showed that the points of maximum **B**-field no longer occurred between the tips of each pair of tooth features, but now occurred between the roots of each pair of tooth features.

Based on these early FEM simulations of the interdigitated comb configuration, the comb configuration was further modified into the “straight line” configuration. The shape of the permalloy line, which is shown in Figure 4-4, allows better utilization of the saturated permalloy than the original comb configuration. The permalloy line is basically a long thin rectangular element with tooth-shaped pattern on the side. Each site between each pair of tooth features is essentially one capturing site. While in operation, the permalloy on the device will be magnetically saturated by the external magnetization source. As the magnetic flux passes through the narrow section of the permalloy, it is forced into the surrounding space, thus, creating a region of high magnetic flux density in the surrounding and forming a magnetic trap. As a result, the magnetically tagged cells will be attracted towards that area. If the geometry and the size of the magnetic trap is carefully designed, only one cell can be fit in each trap, thus, achieving a single cell array. FEM models were use to confirm the performance of the device before fabrication. The FEM models and their solution are presented with details in next chapter.

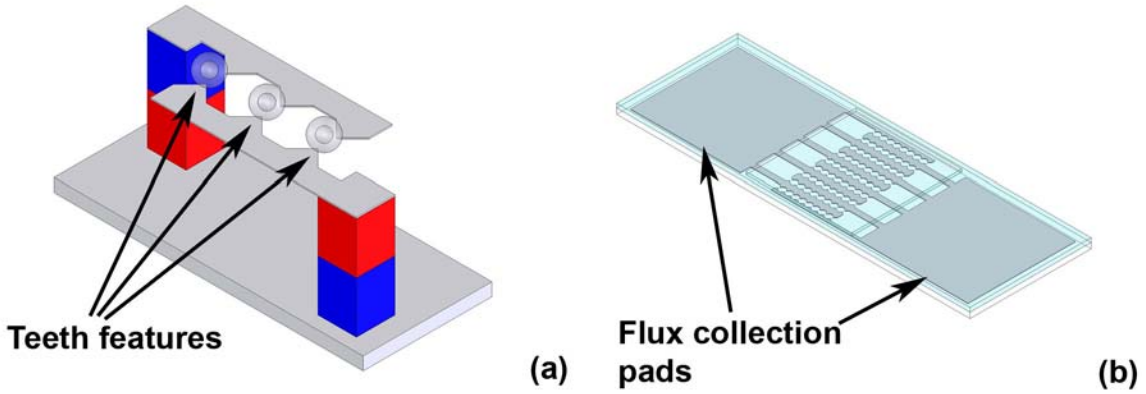

Figure 4-2 (a) Illustration of operation and (b) device construction illustration of the initial MSCMA design.

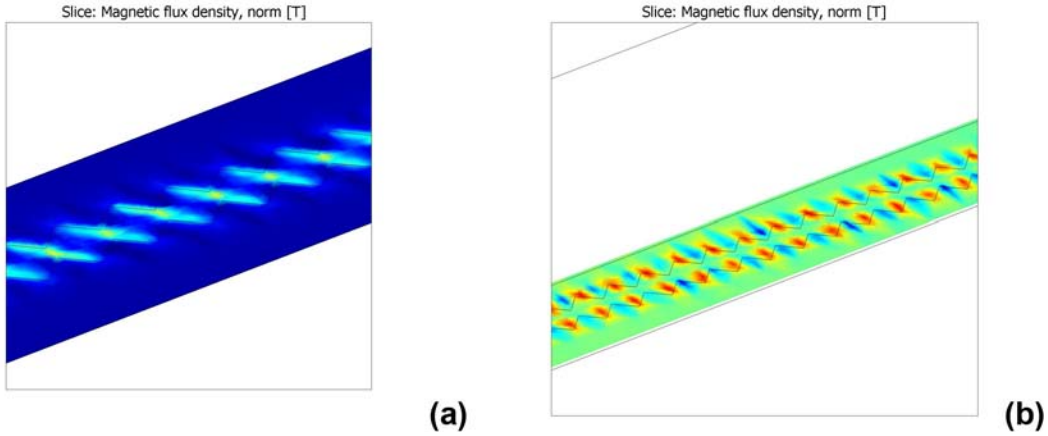

Figure 4-3 (a) FEM simulation of the initial MSCMA concept with linear permeability setting and the (b) the same model with non-linear permeability setting.

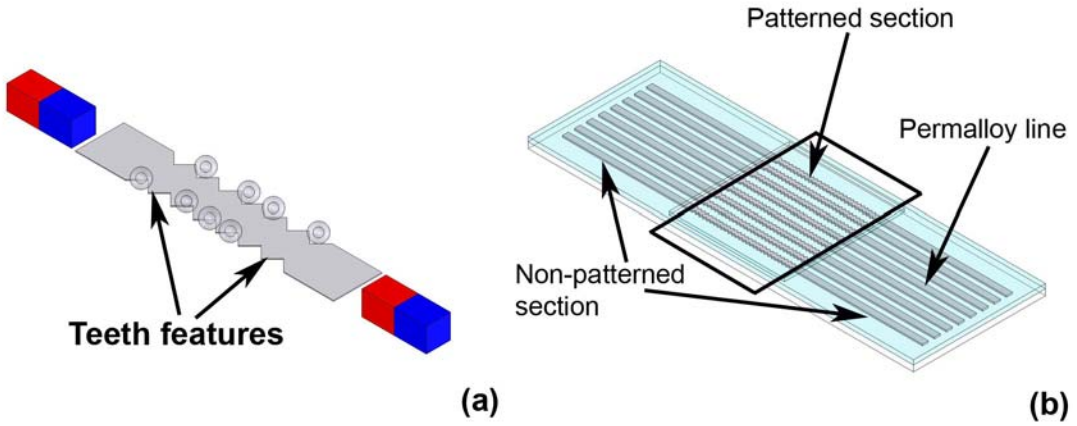

Figure 4-4 (a) Illustration of operation and (b) device construction illustration of the revised permalloy line design.

Chapter 5 FEM Model

In this work, modeling of the magnetic field in and around the MSCMA could only be done using FEM analysis. Like other complex design problems in engineering, the analytical solution is often not practical for complex geometries, such as the features of the MSCMA. Hence, FEM is an essential tool for simulating the magnetic field. Various designs of the MSCMA were simulated using the COMSOL FEM software package, using the AC/DC module.

Ideally, FEM models should simulate the entire MSCMA device using the exact dimensions and details, to yield the most representative result. However, there are physical limitations such as computational power and computer memory that imposed constraints on the fidelity of the model. In general, magnetic FEM models are highly intensive on computational power. Due to the steep gradient of the magnetic field, these models usually need a fine element mesh to accurately model the field, which required many elements. In addition, modelling of the MSCMA is also challenging due to the non-linear magnetic permeability of the permalloy and the high aspect ratio of the geometry of the model. Finally, as with most micro-devices, the scale can vary tremendously over the device model, with tooth features in the range of 10 μm, while the finger features range in size up to 15000 μm. This requires careful element meshing, and/or model sub-division to achieve computationally feasible FEM models. The following sections will illustrate and address these issues with the FEM models of the MSCMA.

5.1 Permeability Model

It is important to precisely model the material properties for an FEM model, to achieve accurate results. Thus, it is important to obtain a representative permeability model for

the permalloy. In COMSOL, the permeability of the material can be entered manually using the material properties setting. Users may enter a constant number (linear model) or a function into the permeability field. This function may either be in an analytical format or in an interpolated curve format (from a set of data points). For the case of using an interpolated curve, a representative set of data points for the material must first be obtained.

As stated previously, many materials exhibit non-linear magnetic behaviour, and permalloy is one such material. In the past, a number of researchers have done experiments to determine the magnetic properties of electroplated permalloys. In general, Ni80Fe20 permalloy has a relative permeability between 500-1000 and a saturation magnetization of about 1 Tesla. Detailed **M vs. H** plots have been developed separately by Taylor *et al.* and Park *et al.* from their experiments [52,53]. These plots were used for graphically determining the relative permeability of the permalloy, when setting up the permeability model for our FEM simulations. To determine the relative permeability from the plots, the magnitude of the **M-**field was measured at different levels of the **H-**field on the curve. At a given **H-**field, the **M-**field and μ_r is given by

$$\mathbf{M} = \chi\mathbf{H} \qquad \textbf{eq 5.1}$$

$$\mu_r = 1 + \chi \qquad \textbf{eq 5.2}$$

Thus

$$\mu_r = \frac{\mathbf{M}}{\mathbf{H}} + 1 \qquad \textbf{eq 5.3}$$

Using this equation, μ_r data points can be obtained from the plot. These data points are then entered into MatLab for further processing. In order to complete the interpolated curve, two assumptions were made:

1. The **M-H** curve is perfectly linear in a weak **H**-field, meaning that the μ_r is constant in a weak **H**-field.
2. Magnitude of the **M**-field remains constant once saturation is reached. Thus μ_r is approaching 1 as the ratio **M/H** approaches zero.

Based on these assumptions, the μ_r-**H** curve is filled in such that:

1. The linear region is filled in with a constant μ_r straight line.
2. The saturated region is filled in with the curve of eq. 5.3, with **M** held at a constant value.
3. The transition regions between the linear and saturated regions is filled in by extra points using a clamped cubic spline to ensure a smooth transition from the linear to the saturated region. This is reasonable since μ_r changes very rapidly in the transition region.

This set of interpolation curve data points is shown in Appendix A. The data points were then imported into COMSOL to be used as the permeability model for the FEM analysis.

5.2 Boundary Conditions

Using appropriate boundary conditions is very important for a FEM model. Not only are the appropriate boundary conditions important for a proper result, but they also reduce the required computational power by partitioning the area of interest, from the rest of the model, and thereby reduce the model complexity. While analysing the MSCMA, several boundary conditions were applied to partition the model and reduce the model complexity. This section describes the boundary conditions that are used in FEM model, and discusses how these boundaries can improve the efficiency of the mesh.

5.2.1 Use of Symmetry Conditions and Magnetic Shield Elements

Consider the example models illustrated in Fig. 5-1 (a). Model A is a magnetic setup that consists of two N40 neodymium magnets sitting on either side of a permalloy block. The two N40 neodymium magnets are each 6.35 mm × 6.35 mm × 19.05 mm in size. The permalloy block is 0.5 mm × 15 mm × 10 mm in size. Using the standard "mesh" menu of COMSOL, with a "finer" mesh setting, a mesh having a total of 168352 elements and 232266 degrees of freedom was generated. The model was then initially simulated with a linear permeability model. The result of the linear permeability model was then used as the initial approximation for solving main the model with a non-linear permeability setting. This was done to avoid a singularity in the initial approximation expression of the solver of COMSOL. The two models took 75 seconds and 1200 seconds to be solved respectively. A plot of the result of the simulation is shown in Fig. 5-1 (b).

Although Model A is not particularly complex, the computational power required to solve the model can be reduced by partitioning and simplifying the model by appropriately applying certain boundary conditions. It is not hard to notice that Model A is geometrically symmetric about the $x = 0$ plane, the $y = 0$ plane and the $z = 0$ plane, as shown in Fig. 5-1(a). This geometrical symmetry created a symmetric magnetic field about these planes. As shown in Fig. 5-1(b), the magnetic flux lines near the $y = 0$ plane and the $z = 0$ plane are parallel to the planes, and the flux lines crossing the $x = 0$ plane are normal to the plane. Therefore symmetry conditions can be applied at these planes to partition one eighth of the model. As a result, the "zero potential" condition can be assigned to the $x = 0$ plane to indicate that all magnetic flux crossing this plane is normal to the plane, and no flux is tangential to the plane. On the other hand, the "magnetic insulation" condition can be assigned to the $y = 0$ plane and $z = 0$ plane to indicate that

the magnetic flux on these planes is tangential to the planes, and no flux is crossing these planes. Fig. 5-2 shows the updated Model A, renamed as Model B, where only one eighth of the original domain is modelled. As Fig. 5-2(b) shows, the profile of the magnetic flux lines closely resembles that of Fig. 5-1(b). Also the magnetic potential and the magnetic flux density plots are quite similar between Model A and Model B.

In addition to applying the symmetry conditions, Model B can be further simplified by eliminating the thin permalloy block domain. For FEM simulations of MEMS devices, the high aspect ratio of parts, will often lead to meshes with a large number of elements. The high aspect ratio refers to the fact that one dimension of a MEMS part may be two or more orders of magnitude higher than the smaller dimensions. Since it is good practice to use FEM elements with roughly equal sides, the size of the elements should not be larger than the smallest dimension of the domain. As the size of the elements is limited by the smallest dimension of the part, it would take a large number of elements to fill up the domain. For example, number of elements in the permalloy block domain of Model B is 1662. In contrast, number of elements in the domain of the magnet is only 353. Due to the lower aspect ratio of the magnet, bigger elements can be used in that domain. Thus, it takes much fewer elements to fill up the magnet than to fill up the permalloy block, even though the magnet is larger than the permalloy block. To resolve the high aspect ratio part problem, COMSOL offers a “magnetic shield element” option for modeling thin sections of magnetic material. The magnetic shield element is essentially a 2-D boundary that allows the user to specify the thickness and the permeability of the material to the boundary. Using this type of element to replace the permalloy block in Model B greatly simplified the mesh by eliminating the high aspect ratio domain of the permalloy block.

Model C, shown in Fig. 5-3(a), is derived from Model B, where the permalloy block is replaced by the magnetic shield element. Meshing with the standard “mesh” menu under the same settings, the total number of elements in the mesh reduces from 111595 in Model B, to 104675 elements in Model C. The solution time is also reduced from 284 seconds to 224 seconds. While the mesh size and the computation time were reduced, the solution was not altered significantly. As Fig. 5-3(b) shows, the flux profile, the measured magnitude of the magnetic flux line, the magnetic flux density plot and the magnetic potential plot are similar to those in Fig. 5-2(b). Note that the values of the magnetic flux density at the edge of the permalloy block are almost 50% different in magnitude. This is likely to be caused by the replacing the permalloy block, which has a finite thickness, with a “magnetic shield” boundary that has no thickness. Accuracy of the magnetic shield approximation will improve as the thickness of the material (i.e. the permalloy block in Model B) approaches zero.

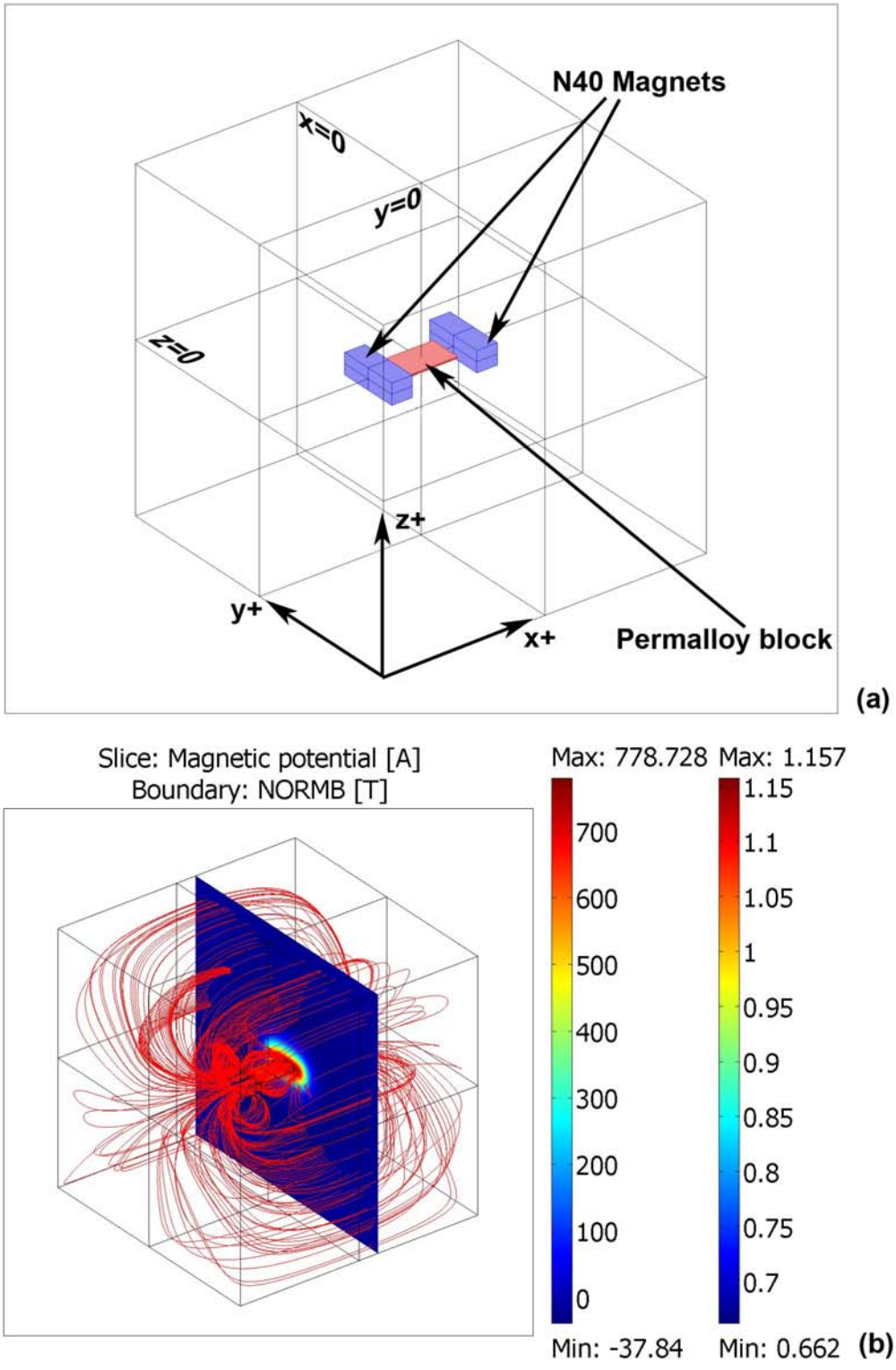

Figure 5-1 (a) Model A with the magnets labelled in blue and the permalloy layer labelled in red, and plots of the solution to the right. (b) Magnetic potential plot at x = 8 mm, magnetic flux density plot inside the permalloy block and the magnetic flux line plot.

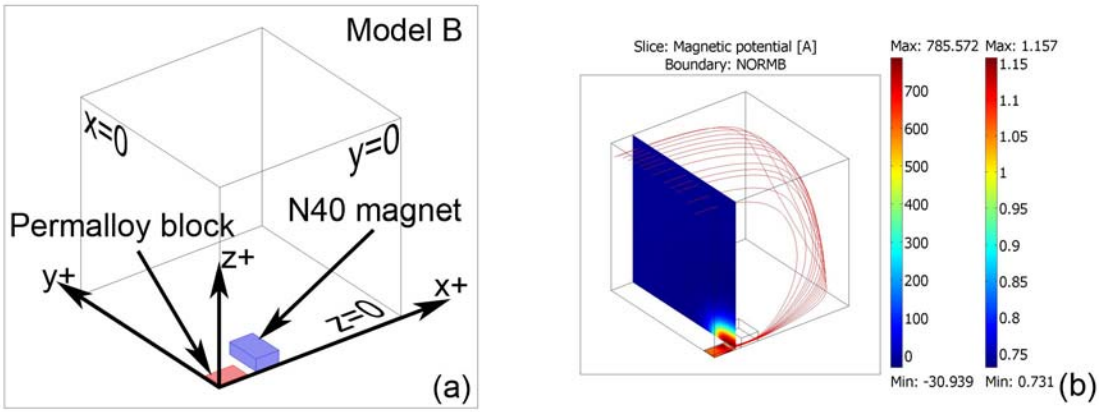

Figure 5-2 (a) Model B with the magnets labelled in blue and the permalloy block labelled in red. (b) Magnetic potential plot at x = 8 mm, magnetic flux density plot inside the permalloy block and the plot of selected magnetic flux line.

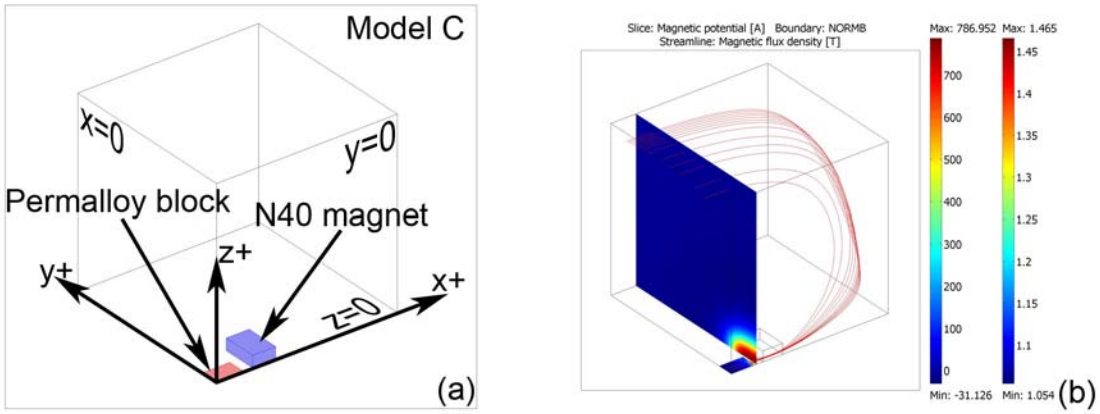

Figure 5-3 (a) Model C with the magnets labelled in blue and the permalloy layer labelled in red, and plots of the solution to the right. (b) Magnetic potential plot at x = 8 mm, magnetic flux density plot inside the permalloy block and the plot of selected magnetic flux line.

5.2.2 Partitioning the Permalloy Line in the FEM Model

Fig. 4-4(b) showed that the MSCMA device consists of a set of parallel permalloy lines. Since the permalloy lines are all exactly the same, and all parallel with each other, only one permalloy line is needed to be analysed to get the magnetic field profile. The magnetization configuration of the MSCMA actually provides a nice property for partitioning the model to contain only a single permalloy line. This property can be illustrated by using Model B as an example. As Fig. 5-4(a) shows, in the absence of the

permalloy block, the magnetic field around the $y = 0$ symmetry plane is uniform, and the flux lines are parallel to each other and the symmetry plane. As shown in Fig. 5-4(b), only the magnetic field near the top surface of the permalloy block is disturbed by its presence, while the flux lines away from permalloy block remain parallel to the symmetry planes. Therefore, a strip of the permalloy block can be partitioned from the rest of the block by applying the "magnetic insulation" boundary around the strip to simulate the surrounding parallel flux lines.

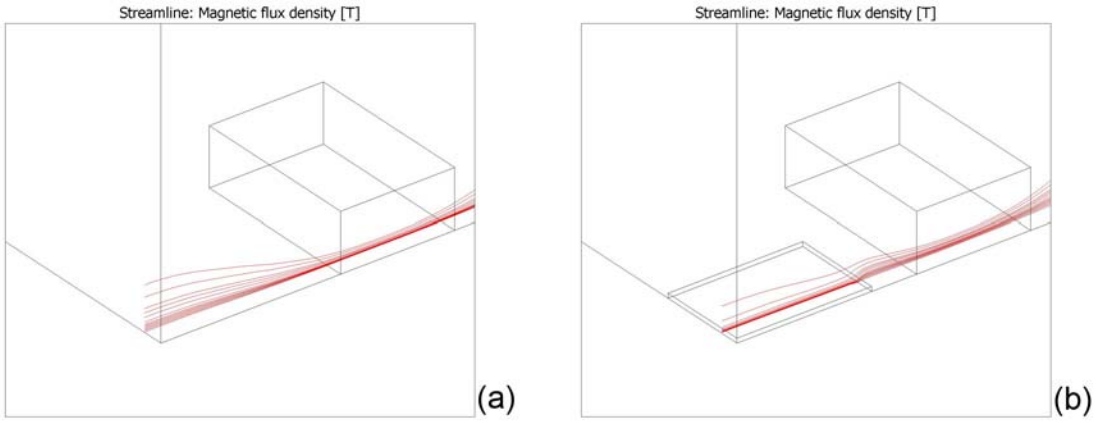

Figure 5-4 (a) Plot of selected magnetic flux line in Model B absence of the permalloy block. (b) Selected magnetic flux lines with the presence of the permalloy block.

Model D, shown in Fig. 5-5(a-b), simulates only a strip of the permalloy block. As Fig. 5-5(c) indicates, the magnetic flux density measurement inside the permalloy block is consistent with the result that is obtained in Model B. Notice that the height of the domain should be set in a way so that the permalloy block has negligible effect on the magnetic field near the top boundary of the model. As Fig. 5-5(b) shows, the magnetic flux lines flatten out at a height of over 1 mm, indicating that the influence of the permalloy block on the magnetic field has diminished at this height. If the top boundary is too close to the permalloy block, the "magnetic insulation" boundary condition will not be valid and will cause an error while solving the model. This is because the magnetic

field near the permalloy block is disturbed by the presence of the permalloy block, which causes the flux lines to bend toward the permalloy block, instead of passing over the permalloy block parallel to the top boundary. For Model D, it was determined in simulation that the solver would fail to converge if the height of the domain is lower than 500 μm.

As shown in the illustration of Model D, it is possible to partition a strip of the permalloy block by using the "uniform magnetic field property" between the magnets. Therefore, a single permalloy line can be partitioned from the rest of the MSCMA by the same procedure. This greatly reduces the model size and complexity for the FEM analysis of the MSCMA.

5.3 Layer Thickness

The electroplating fabrication process to create the permalloy layer is subject to variability. The thickness of the permalloy layer may not be perfect across the whole device due to edge effects of the electric field [54,57]. Since the electroplating current path is blocked by the non-conducting photoresist mask, current lines will tend to bunch up at the edges of the mask. Thus, the current density at the mask edges is often higher than the surroundings, which causes a higher deposition rate around the edges. To investigate the effect of the thickness variation on the performance of the MSCMA, several FEM simulations were conducted with thickness variations. The layer thickness in a regular model is 5 μm, but the thickness was varied between 5 μm to 6 μm for the sensitivity analysis. The thickness variation was defined by an analytical function based on the model coordinates, given as:

$$T = 2.5 * 10^{-6}(1 + 1777.78x^2)(1 + 4 * 10^7 y^2)$$

This function gives roughly a bowl shape with minimum thickness T at the origin, $(x,y)=(0,0)$, and maximum thickness around the edge of the of the layer.

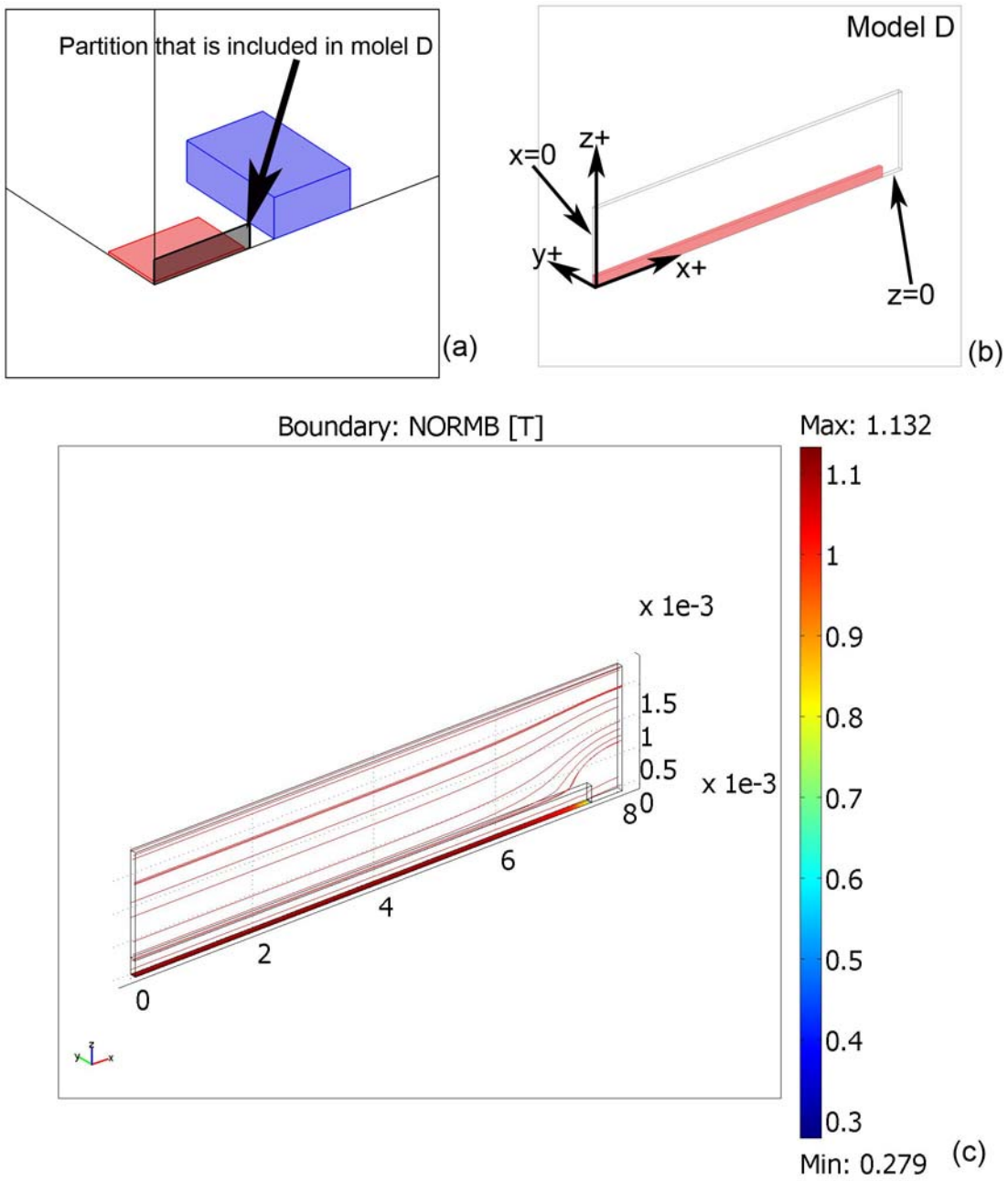

Figure 5-5 (a) The partition simulated by Model D. (b) Model D with the permalloy layer labelled in red, and (c) Magnetic flux density plot inside the permalloy block and the plot of selected magnetic flux line.

5.4 Gradient Calculation

The magnetic force on any material is proportional to the gradient of the **B-**field around it. Therefore, it is desirable to have a plot of the gradient of the **B-**field, however, the post-processing function of COMOSOL does not calculate the gradient field data directly. However, COMSOL does allow users to export the simulation solution to MatLab, where further processing can be done. The program code used for the gradient plotting function is attached in Appendix B. In order to make the gradient plot, the plotting function first reads the solution of the FEM model and obtains the values of magnetic flux density at the points that are specified by the array grid. The gradient of the **B-**field is then calculated with the standard "gradient.m" function in MatLab. This new data is then plotted with a 3-D arrow plot. Since the 3-D plot is sometimes difficult to visualize, additional 2-D plots of planes parallel to the substrate are made at 1, 6 and 16 microns above the surface. The arrows in these 2-D plots represent the gradient in the x and y-directions and the contour plots represent the gradient in the z-direction.

5.5 FEM Results

In order to limit the computational requirements, only the necessary details were modelled in the FEM model of the MSCMA. The MSCMA was modelled at two scale levels. The first simulations were a series of macro-scaled models that were used for determining the magnetic potential near the pole surface of the magnets and the effect of the yoke design. These models were simplified by applying the boundary conditions that were discussed in section 5.2.1 at the symmetry planes of the model. Furthermore, the MSCMA was simplified to a rectangular magnetic shield.

The second series of simulations were micro-scaled models that were used for evaluating the design of the permalloy line. In these models, the permalloy line is

partitioned from the rest of the model by using the same boundary condition as Model D in section 5.2.2. Only one quarter of the permalloy line is modelled, as the permalloy line is symmetric about the major axis and the minor axis, as shown in Fig. 4-4(a). Since the permalloy line is only 5 μm thick but 1.5 mm in length, it is model as a "magnetic shield" boundary to avoid the use of high aspect ration domain. The magnetization source is simulated by applying a magnetic potential on the boundary at the end of the permalloy line. The magnitude of the applied magnetic potential is determined from the macro-scaled model. The following sections will present and discuss the results from the models.

5.5.1 Macro-scaled Models

Two magnetization directions were examined with the macro-scaled models, which were: (i) perpendicular to the MSCMA and (ii) along the major axis of the MSCMA. Figure 5-6 shows the configuration of both models. Models with N-40 neodymium magnets of different size and yoke design were constructed. As Fig. 5-7(a-d) shows, regardless of the magnet size and the yoke design, the flux density in the middle part of the permalloy layers reaches about 1 Tesla. The simulations also showed that placing the magnets directly under the permalloy will cause a band of high magnetic flux density region near the edge of the magnets. This may pull the cells toward the sides of the MSCMA, thus away from the cell array in the middle portion of the MSCMA. On the other hand, placing the magnets with their magnetization axis aligned with the major axis of the MSCMA will only cause a narrow band of high magnetic flux density region near the edge of the permalloy layer. The gradient of the **B**-field is relatively small in the direction of the major axis of the MSCMA. Moreover, it was also noticed that the yoke

that connects the magnets on either side of the MSCMA does not have a significant effect on the magnetization of the MSCMA. As Fig 5.7(e-f) shows, removing the yoke does not affect the magnetic flux density in the middle portion of the MSCMA, while the magnetic flux density at the edge is significantly reduced. This is because the thickness and the volume of the MSCMA are very small. The permalloy is only 5 μm thick in the model, and hence the MSCMA can be easily saturated by the macro-size magnets. Therefore, the permalloy layer is saturated by the magnets with the yoke or not. Once the MSCMA is saturated, any further increase in the magnetic field strength will cause very little change on the flux density within the MSCMA. Similarly, the distance between the magnet pole surface and the MSCMA does not have a significant effect on the flux density in the MSCMA as well. As Fig 5-7(c-d) shows, whether the magnet is several millimetres away from the MSCMA, or right at the edge of the MSCMA, the magnitude of the magnetic flux density in the middle portion of the MSCMA in the two cases is about the same.

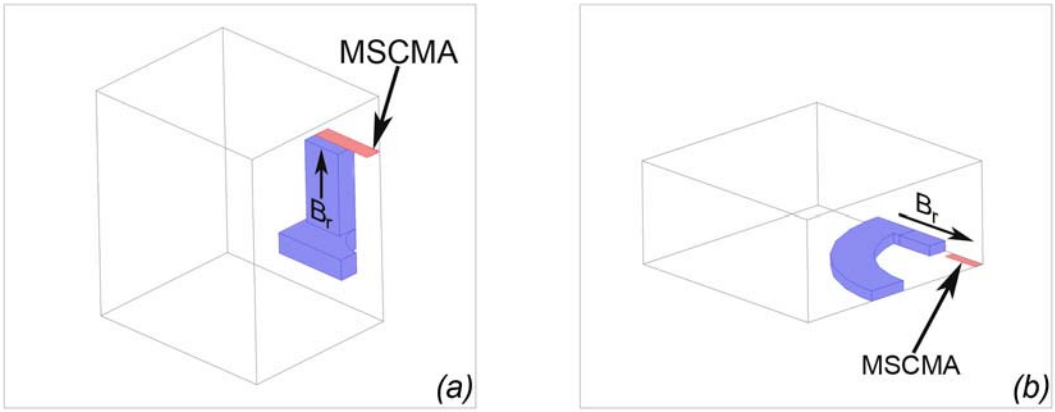

Figure 5-6 Magnetization configuration of macro-scaled models, the permalloy layer is labelled in red, magnets and yoke are labelled in blue. (a) The permalloy layer is magnetized from the bottom. (b) The permalloy layer is magnetized from the side.

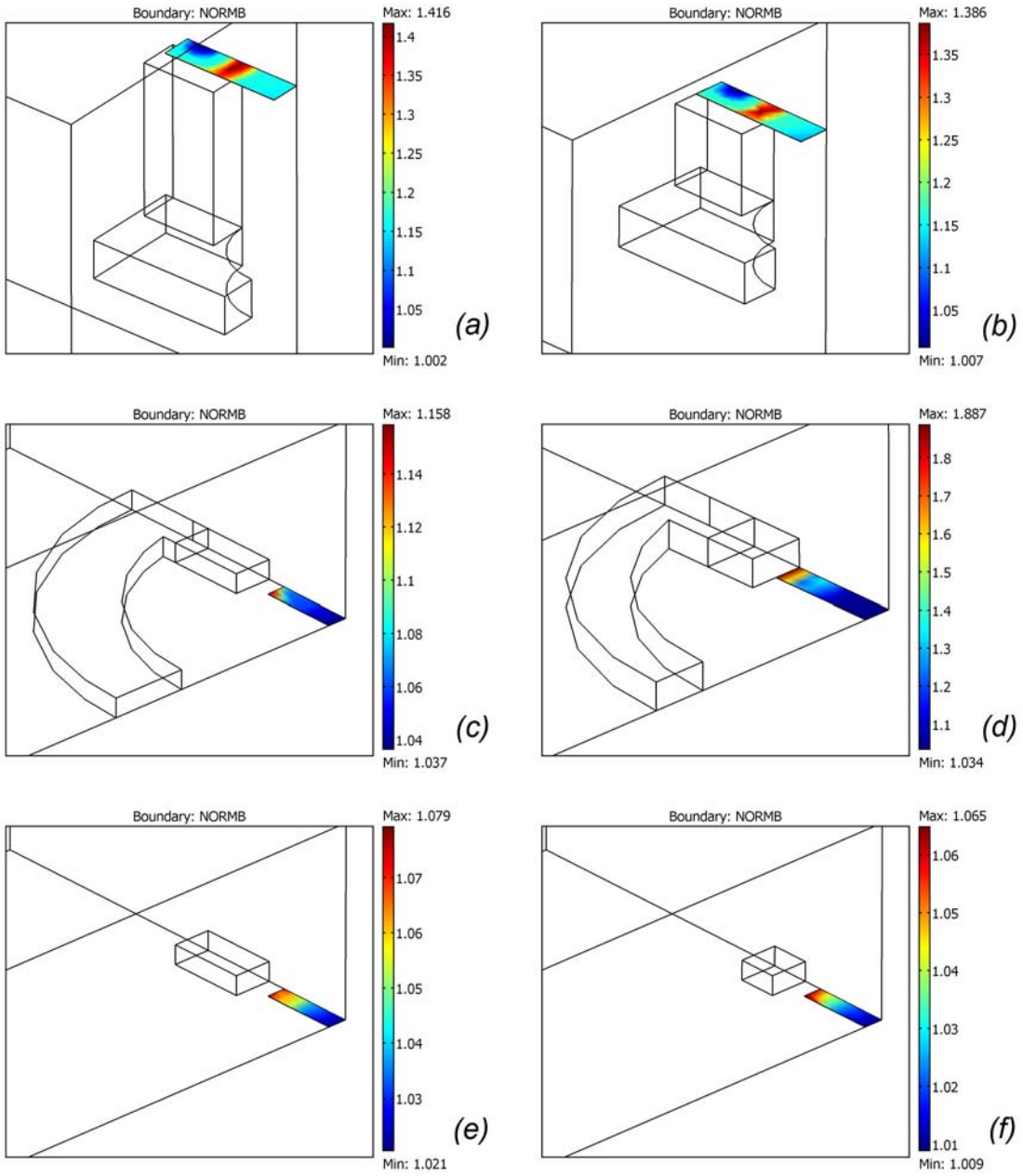

Figure 5-7 Magnetic flux density plots of the permalloy layer of the macro- scaled models.

5.5.2 Micro-scaled Models

Placing and shaping the permalloy correctly is an important factor in the performance of the MSCMA. Using the micro-scaled FEM models, the various designs of the permalloy lines were evaluated. The simulation solutions of these models are showed and discussed in this section. Fig. 5-6 shows magnetic flux density plots of various 2-D

planes that are parallel to the chip surface, and located at different z-axis heights above the surface. Each magnetic flux density maxima, the spot of warm colour, is a magnetic trap. As it was suggested, these magnetic traps are located above the area between each pair of tooth features. Notice that the magnetic traps remains distinguishable even at the height of 26 μm.

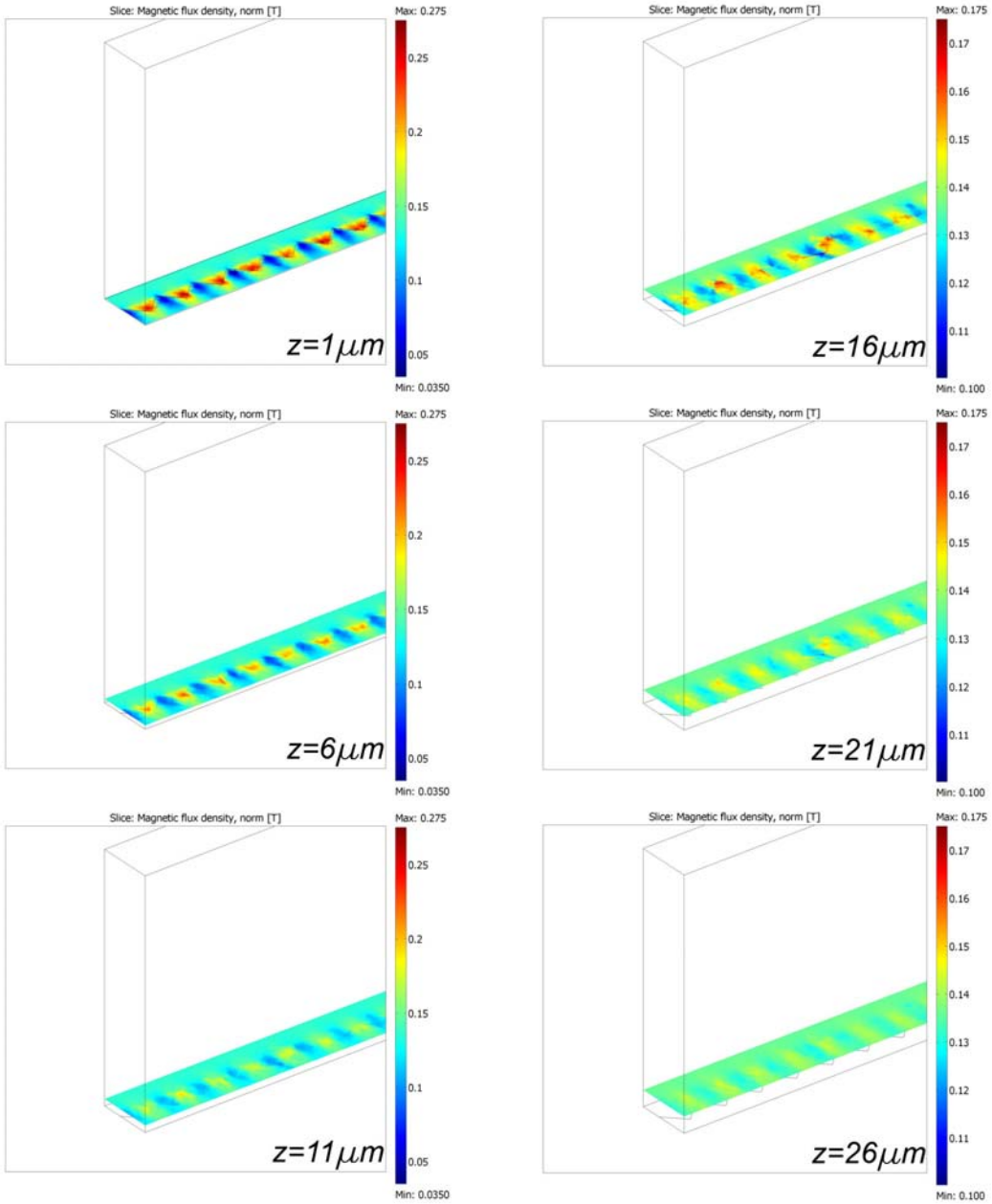

Figure 5-8 Magnetic flux density at different height above the permalloy line. Note the colour scale is different on the plots on the left and on the right.

Fig. 5-9 shows the low magnetic flux density region, the blue region, around the traps essentially forms a magnetic wall to stop any captured cell from moving away from the traps. Regardless of the profile of the tooth features, the gradient of the **B**-field is steepest on the sides of the traps. The gradient at the top of the magnetic traps second steepest direction, while the gradient toward the bottom of the magnetic traps is the shallowest. Comparing Fig. 5-10(a) to Fig. 5-10(c), and Fig. 5-10(b) to Fig. 5-10(d) shows that the field around the traps scales according to the geometry. Thus, scaling the pattern does not affect the profile of the magnetic traps, but only affects the size of the magnetic traps, since the fringing magnetic flux does not stretch as far into the space above the permalloy. As a result, the cells around the device will not experience the influence of the MSCMA until it comes closer to the magnetic trap. Scaling the geometry also affects the magnitude of the **B**-field around the traps. However, if a smaller scale pattern is used, the gradient and the magnetic force around this region are not affected as much as the magnitude of the **B**-field.

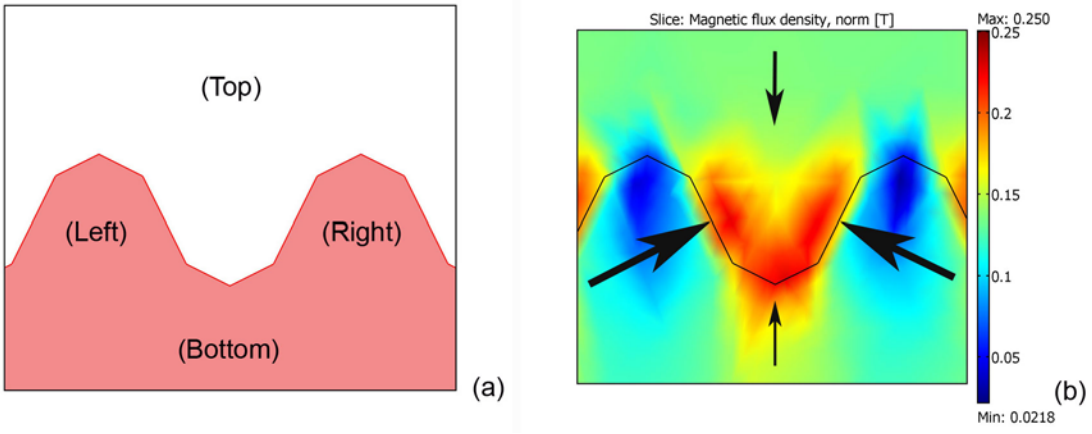

Figure 5-9 (a) Shape of the permalloy is shown in red. The orientation with respect to the magnetic trap is indicated. (b) Magnetic flux density plot of a magnetic trap. The general direction of the gradient of the B-field is indicated by the arrows, where the size of the arrows indicates the relative slope of the gradient.

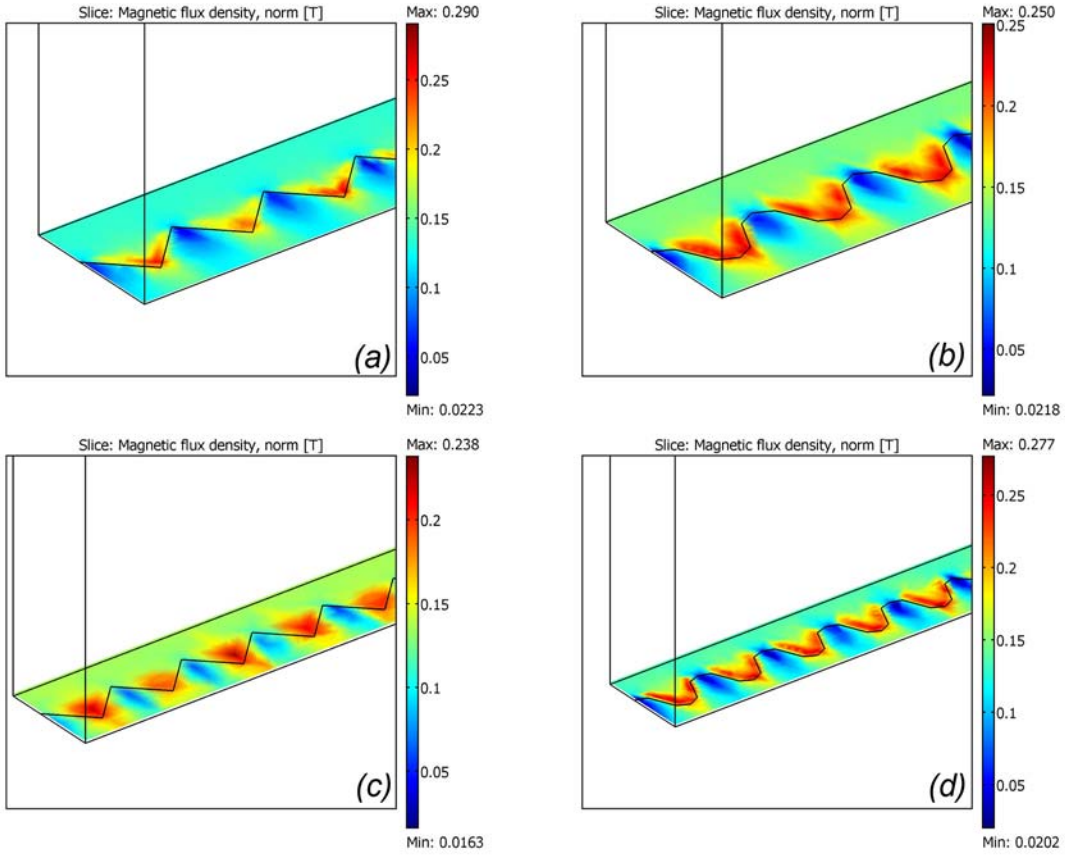

Figure 5-10 Magnetic flux density plots over two set of permalloy lines. Where (c) is the half size version of (a), and (d) is the half size version of (b). The tooth pitch of (a)(b) and (c)(d) are 60μm and 30 μm respectively.

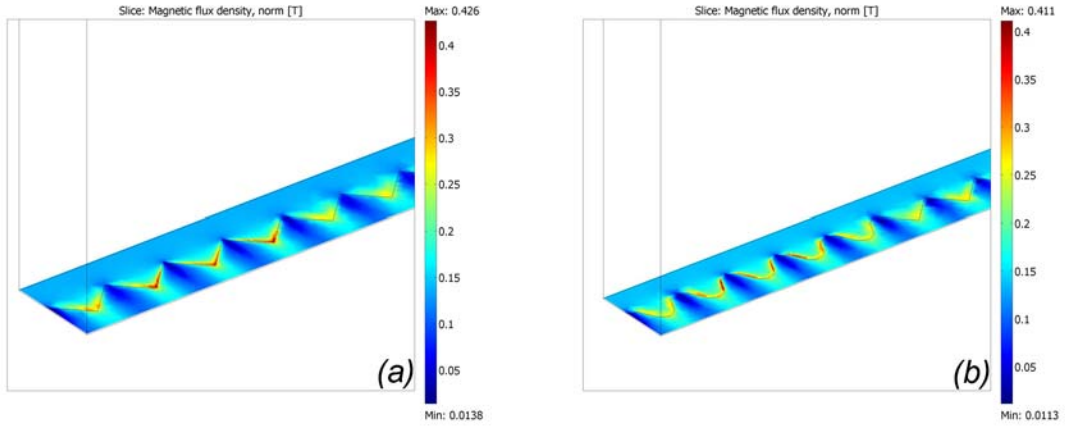

Figure 5-11 Magnetic flux density plots over the same permalloy pattern of that in Fig. 5-8 with a finer mesh.

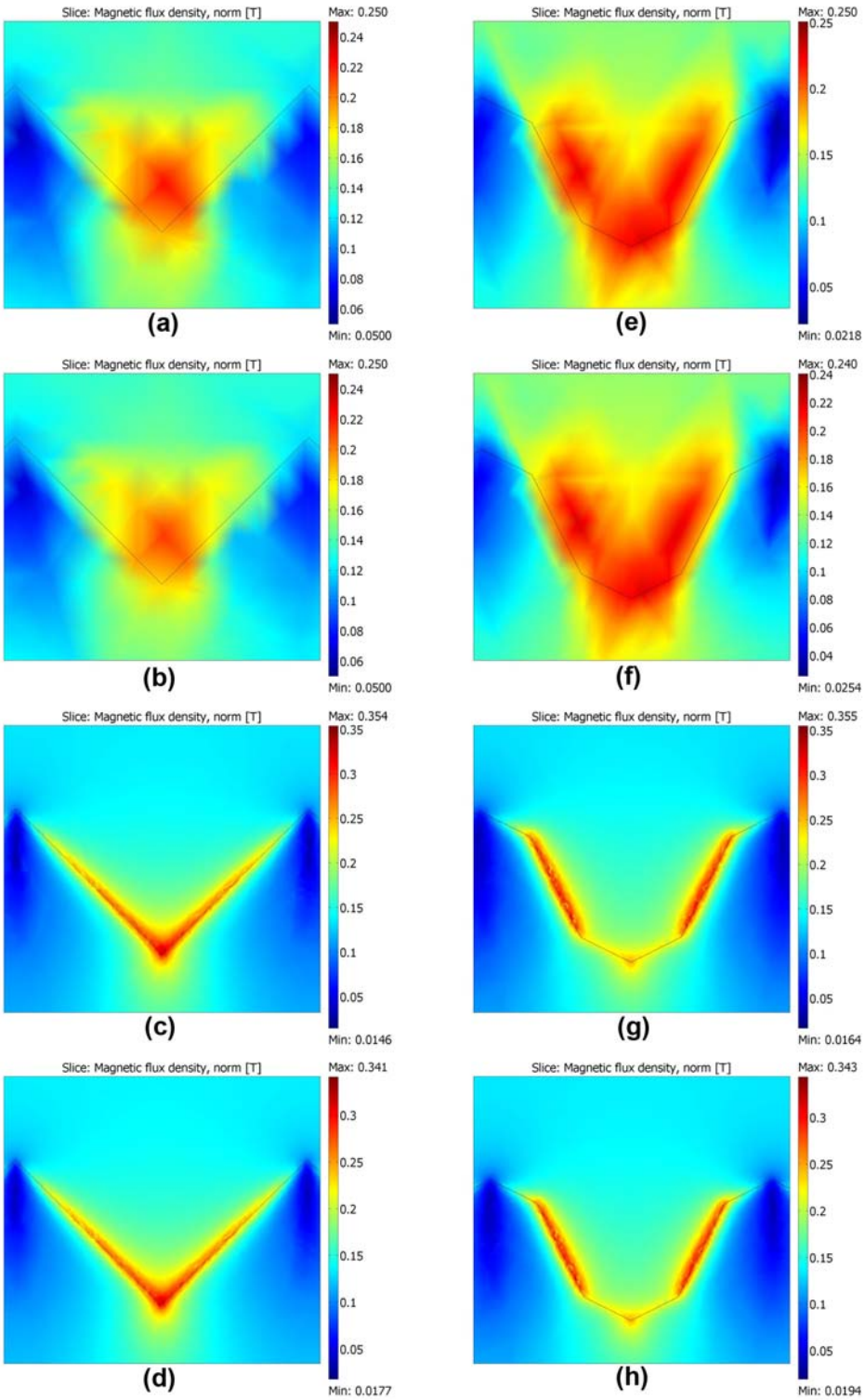

Figure 5-12 (a) and (e) are the B-field plot of a constant thickness models. (b) and (f) are the B-field plot of the variable thickness models. (c)and (g) are the same plot of the constant thickness models at fine mesh setting. (d) and (h) are the variable thickness models at a fine mesh setting.

Fig. 5-11 shows the same models as those in Fig. 5-10(a-b), however it uses a finer mesh setting. Notice the concentration of the magnetic flux along the side edge of the trap. This is the location where fringing magnetic flux escapes from the permalloy layer, since the permalloy is saturated. Moreover, in the model of the permalloy line that has the tooth features that have a variable side wall slope pattern, such as the pattern that is shown in Fig. 5-9(b), the concentration of magnetic flux is higher on the edges that have the steeper slope than the edges that have the shallower slope relative to the major axis. This is because the edges that have the steeper slope intercept more flux line than the edges that have the shallower slope. The effect of the thickness non-uniformity is also investigated in simulation. Fig. 5-10 shows that the profile and magnitude of the **B**-field is not affected even when using different designs and different mesh sizes. By importing the data form these models into MatLab, and using the plotting function of Appendix B, the **B**-field gradient can be calculated for visualizing the force field around the magnetic traps. As shown in Fig. 5-11, the **B**-field gradient vectors are generally pointing into the magnetic trap. In the plot of Fig. 5-11(a-b) the **B**-field gradient vectors are generally pointing into the magnetic trap, but the magnitude and direction of the vectors are not quite coherent with each other. This is due to the use of a coarse mesh size during simulation., Fig. 5-11(c-d) show that the magnitude and direction of the vectors are more coherent with each other when the FEM model makes use of a fine mesh size.

Lastly, the effect of the length of the non-patterned-section of the permalloy line is also evaluated and shown in Fig. 5-12. As shown in Fig. 5-7 (c-d), the distance between the magnets and the MSCMA does not have a big effect on the **B-**field in the middle portion of the device. Similarly, as shown in Fig. 5-12, shortening the non-patterned-section of

the permalloy line, which effectively lengthen the distance between the magnets and permalloy line, does not have a significant effect on the strength of the **B**-field in the magnetic traps. Hence, the length of the non-patterned-section of the permalloy line, and the position of the magnets with respect to the permalloy line, only have a minor effect on the **B-**field in the magnetic traps, as long as the distance between the magnet and the permalloy line is within a few millimetre.

5.6 Discussion

As determined from the macro-size model FEM simulations, neither of the placement magnets nor the yoke has a significant effect on the performance of the device. This is because of the small thickness of the permalloy layer, which can easily become saturated. The micro-size model simulations show the effectiveness of the patterned permalloy design of generating a set of **B**-field maximum points in an array format. During simulation, using a low resolution mesh setting will hide some details of the field profile of the magnetic traps. However, this coarse mesh resolution is generally adequate for predicting the location of the magnetic trap. In contrast, fine mesh resolution is needed for calculating the field gradient, since the gradient of the **B**-field changes very rapidly from point to point. Fig. 5-11(a) illustrates that a mesh that is too coarse may lead to misleading gradient calculation. Though a finer mesh is always desirable, consideration of computation time and computation capability has to be considered as well. In addition to increasing the required computation time and power, it was observed that fine meshes also made it harder for the solver to converge.

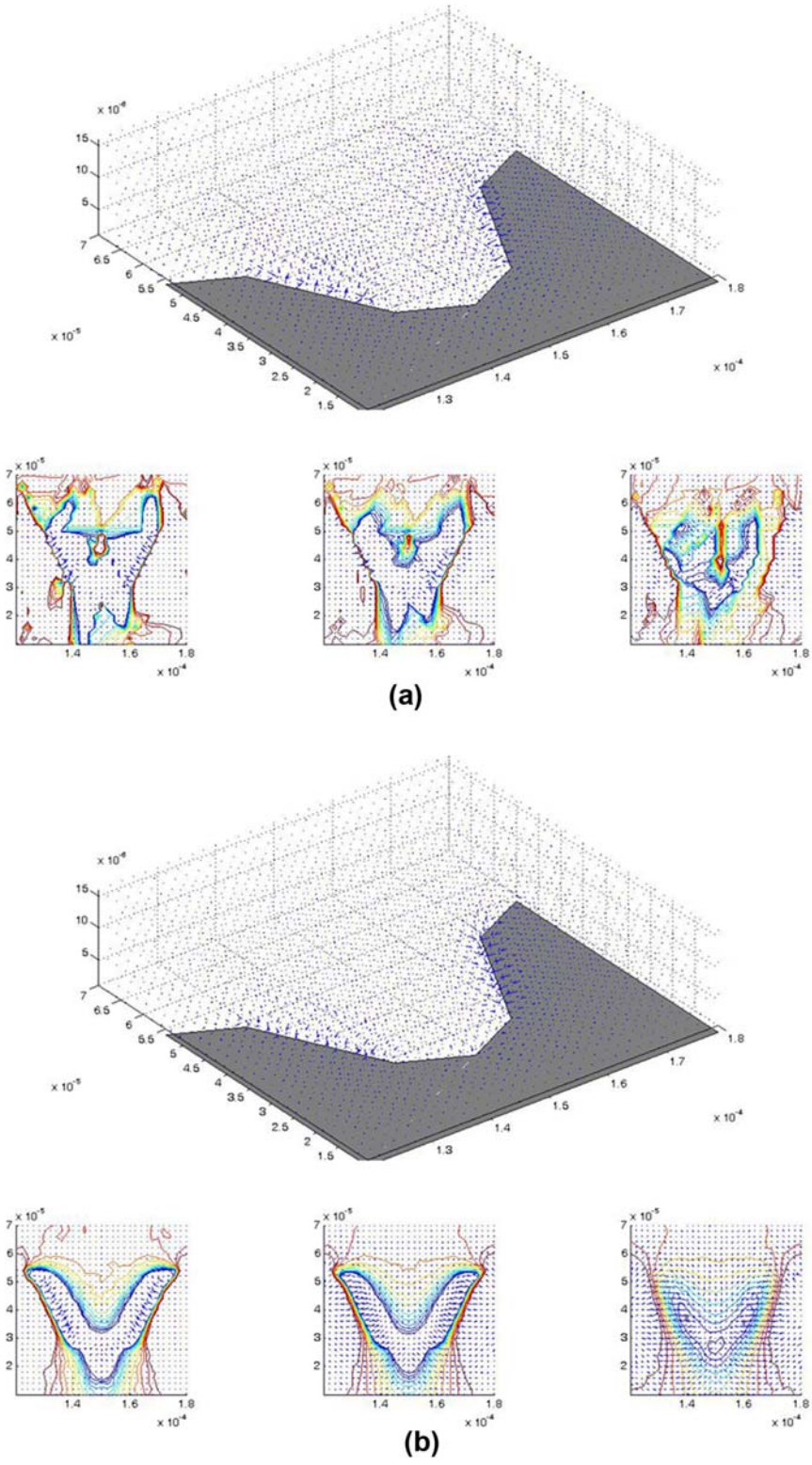

Figure 5-13 (a) The gradient plot of the same model in Fig. 5-12(e). (b) The gradient plot of the same model solved with a fine mesh setting.

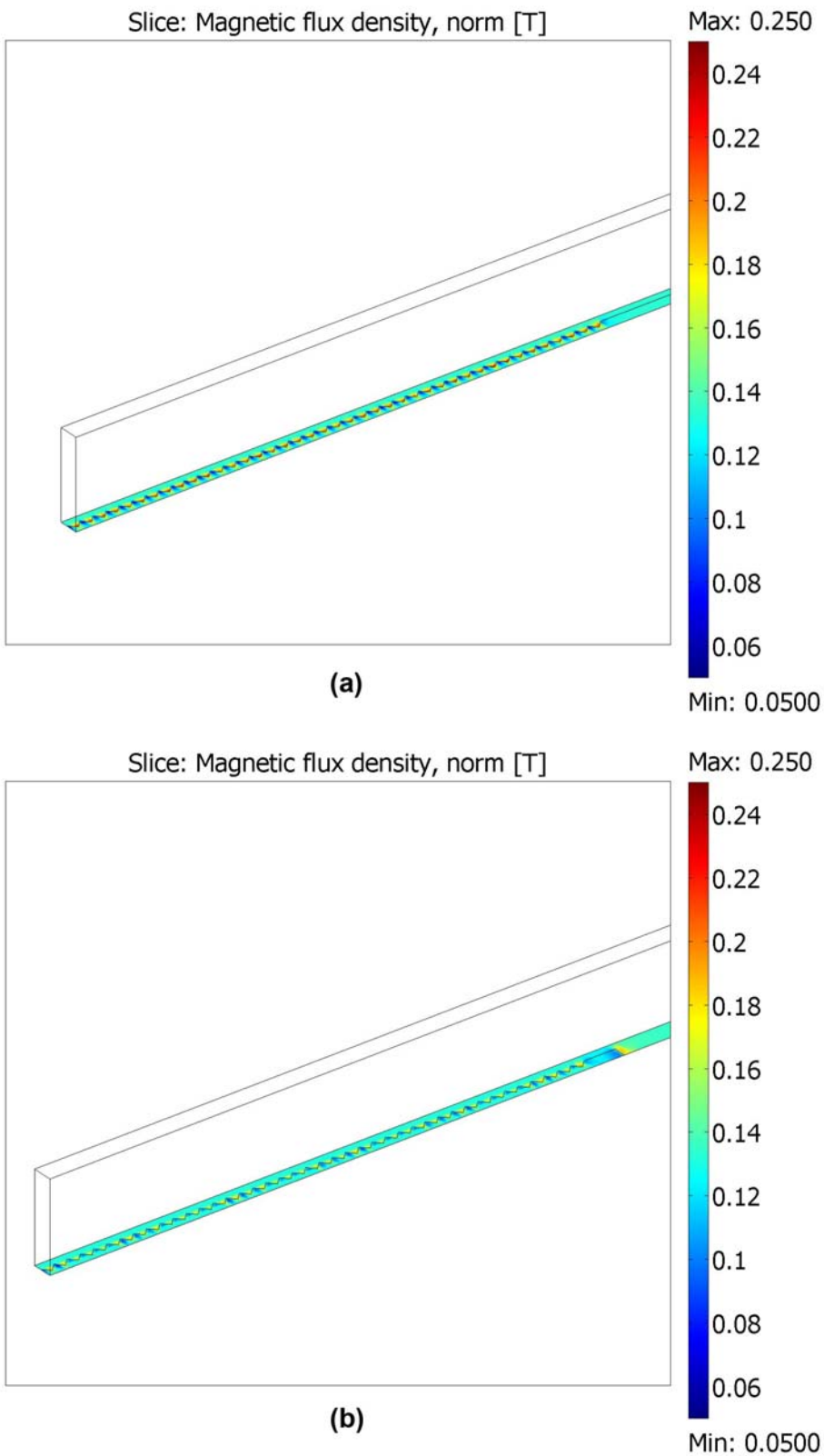

Figure 5-14 (a) B-field plot of the model with a regular non-patterned section, and (b) the model with a shortened non-patterned section .

Chapter 6 Prototype Fabrication

Prototype of the MSCMA were fabricated in order to verify the performance of the proposed MSCMA design, and for proof of concept experiments. The following sections will document the fabrication process and the results of the fabrication of the MSCMA prototypes. Moreover, the problems that were encountered during fabrication will be discussed, along with suggestions for modification to the future fabrication runs are illustrated.

6.1 Overall Fabrication Procedure

The MSCMA prototypes were fabricated using two micromachining methods know as photolithography and through mask electroplating, as shown in Fig. 6-1. The fabrication sequence generally follows the following steps:

Step 1. A 500 μm thick, 100 mm diameter silicon wafer was used as the substrate for the fabrication process. Silicon is an opaque substrate but it was sufficient for the proof of concept experiments.

Step 2. The substrate was coated with a chromium-gold seed layer by sputtering. The seed layer serves as an electric conduction layer for the electroplating process, and as an adhesion layer between the permalloy and the substrate.

Step 3. A layer of AZ-9620 photoresist was spin coated onto the seed layer. This layer was spin coated at 1500rpm for 30 seconds to yield a thickness of 11μm. In addition, the spin rate was ramped up slowly at the beginning to ensure good adhesion between the photoresist and the seed layer. The wafer was soft baked at 110 degrees Celsius for 120 seconds immediately after spin coating to remove the solvent in the photoresist.

Step 4. A Mylar mask, with the permalloy pattern (negative mask pattern) was placed directly on top of the photoresist layer. The mask was made by sending a CAD file of the permalloy pattern to a mask manufacturer.

Step 5. The photoresist layer was then patterned by exposing it under UV light for 4 minutes through a Mylar mask.

Step 6. The exposed wafer was then developed with the AZ-400K developer of the photoresist. The developer would dissolve the exposed portion of the photoresist layer. Therefore, leaving a photoresist mask on the wafer.

Step 7. After photolithography, the wafer was put into the electroplating bath. The bath recipe is shown in Table 6-1. With the seed layer on the substrate connected to the cathode, and a platinized titanium electrode connected as the anode, the wafer was then electroplated for 60 minutes at a current density of 12mA/cm^2.

Step 8. The wafer was then removed from the bath and rinsed with deionised-water. After drying the wafer, the photoresist was dissolved with acetone and the uncovered seed layer was then removed by the gold etchant (Transcence TFA), and the chromium etchant (Transcence Type 1020).

Step 9. A layer of protective SU-8 layer was spin coated onto the device after etching of the gold was completed.

Step 10. Finally, the wafer was diced into die that were 25mm × 15 mm in size. This size is suitable for mounting into the experimental setup.

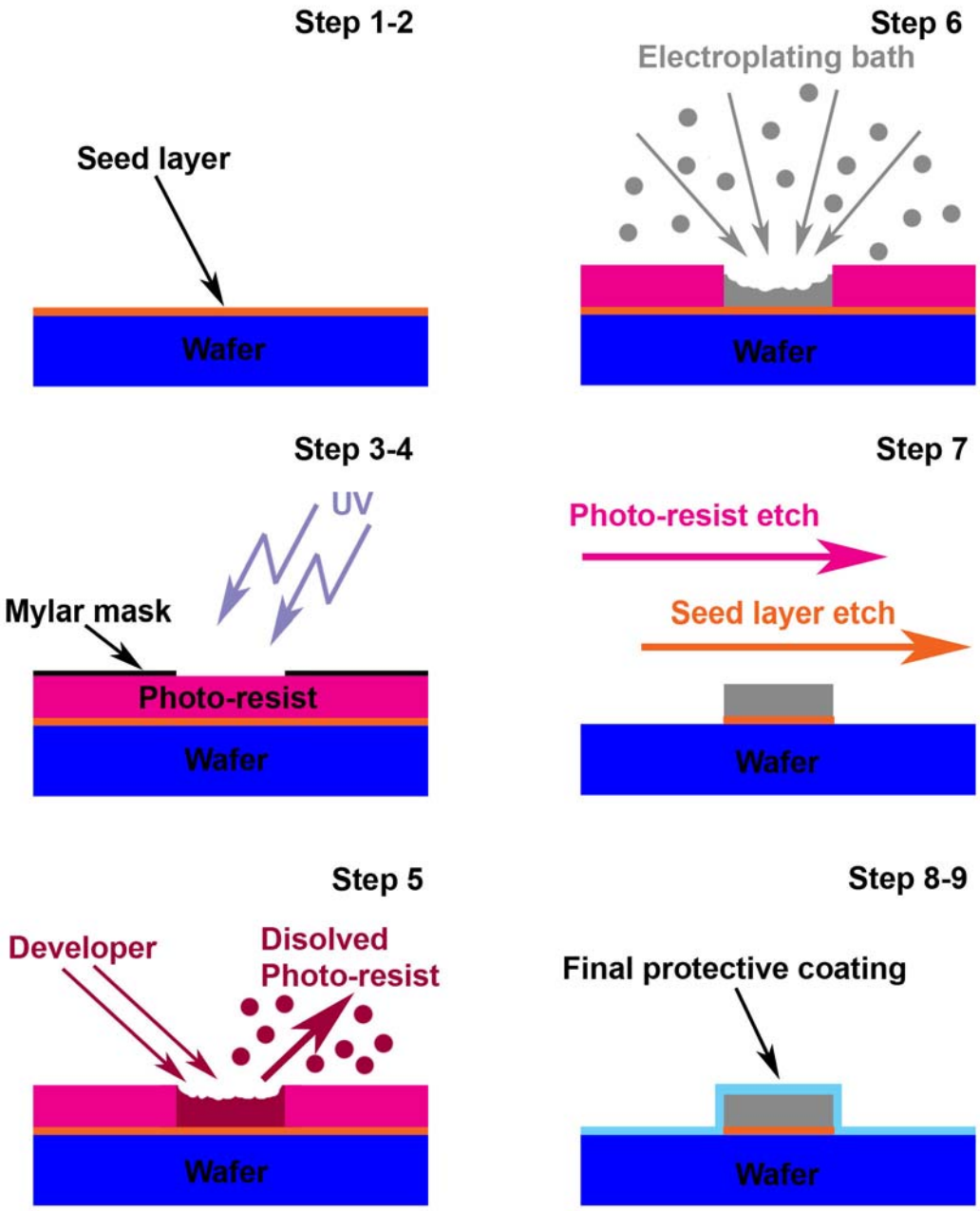

Figure 6-1 graphical illustration of the fabrication process.

$NiCl_2$ $6H_2O$	Nickel(II) chloride hexahydrate	39 g/L
$NiSO_4$ $6H_2O$	Nickel sulfate	16.3g/L
H_3BO_4	Boric-acid powder (Fisher A74-500)	25g/L
	Sodium saccharin, for stress adjustment	1.5g/L
	NaCL, sodium chloride	25g/L
$FeSO_4$ $7H_2O$	Ferrous sulphate crystal	1.4g/L
Note: The solution should have a pH value between 2.7 and 2.8. To lower pH, drop in a small amount of diluted HCL. Ideal current density: 8-12 mA/ cm^2		

Table 6-1 Electroplating bath recipe. This recipe is documented in the textbook by Liu [46].

6.2 Fabrication Result and Discussion

Fig. 6-2 shows the scanning electron microscopy (SEM) images of the prototypes. Fig. 6-2 (b) shows that the permalloy on the an initial prototype that was heavily damaged. This damage was caused by the TFA etchant used for the gold etching step. Due to this damage on the permalloy layer, the gold etching step was skipped in the subsequent MSCMA prototypes, since retaining the gold seed layer on the wafer would not affect the device performance. Ultimately, the MSCMA should be made in such a way that the substrate is transparent. This will require the use of a glass substrate and additionally, it will be necessary to remove the gold seed layer for substrate transparency. Therefore, some other type of seed layer has to be used in the future fabrication runs, which can be etched away without causing damage to the permalloy. For example, Liu [47] reported using a chromium-copper seed layer in the through mask electroplating processes and was able to remove it by etching without damaging the permalloy. On the other hand, Indium Tin Oxide (ITO) may possibly be used as a transparent seed layer for electroplating, and therefore etching would not be needed.

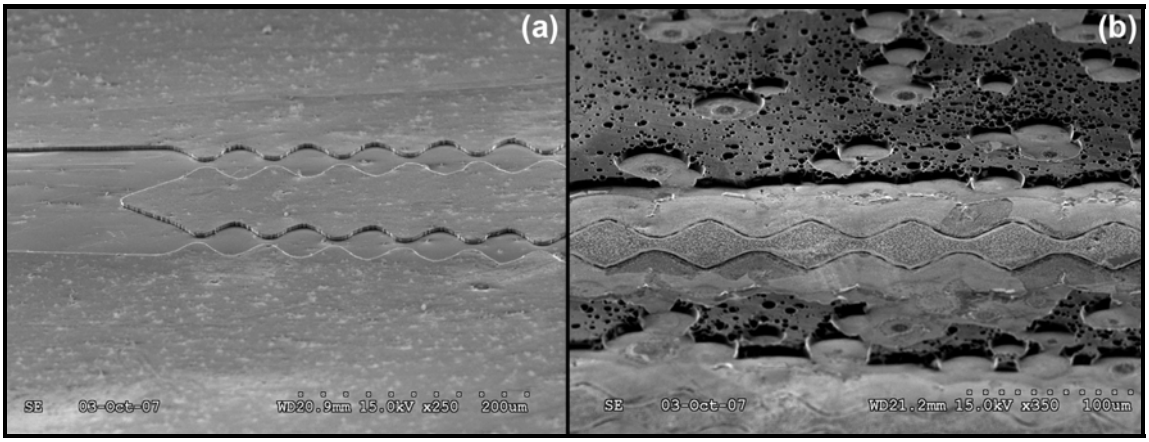

Figure 6-2 SEM image of (a) permalloy layer that has not been etched, and (b) permalloy layer that has been etched. Notice the damage done by the TFA etchant, which almost completely dissolved the permalloy.

In order to fabricate the prototype devices, a physical mask of the permalloy lines had to be made. This is done by sending a CAD (computer aided design) drawing file of the permalloy lines to a mask manufacturer. For the MSCMA prototypes, a Mylar mask was chosen. However, the pattern replication from the CAD design drawings to the actual devices was not exact. All sharp corners in the design were rounded off on the actual devices. Moreover, the dimensions of the features were also slightly altered, while the tooth features on the side of the permalloy lines were slightly wider than the original CAD design. The details from the CAD design were mainly lost in two of the steps of the fabrication process. Firstly, the resolution of the printing process of the Mylar mask is limited, thus, perfectly sharp corners are impossible to obtain. Secondly, due to the fringing effect of light around the opaque edges of the mask, the area of exposed photoresist is slightly larger than the transparent area on the mask. As Fig. 6-4(a) shows, the effect of the fringing light can be minimized by having a tight contact between the mask and the photoresist. Fig. 6-4(b) shows that a poor contact between the mask and the photoresist may result in significant loss of features.

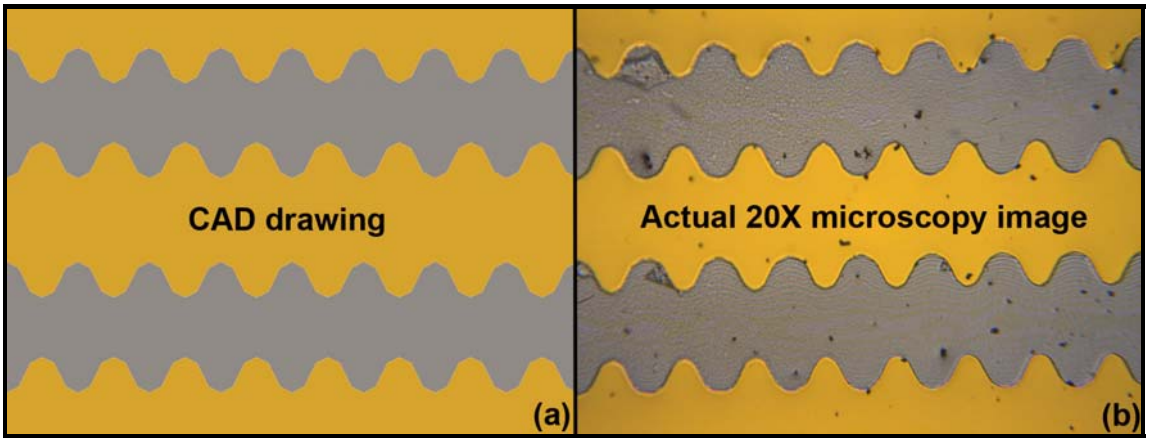

Figure 6-3 Comparison between layer profile in (a) CAD drawing and (b) actual fabricated layer. The grey area is the permalloy layer, and gold area is the underlying gold seed layer.

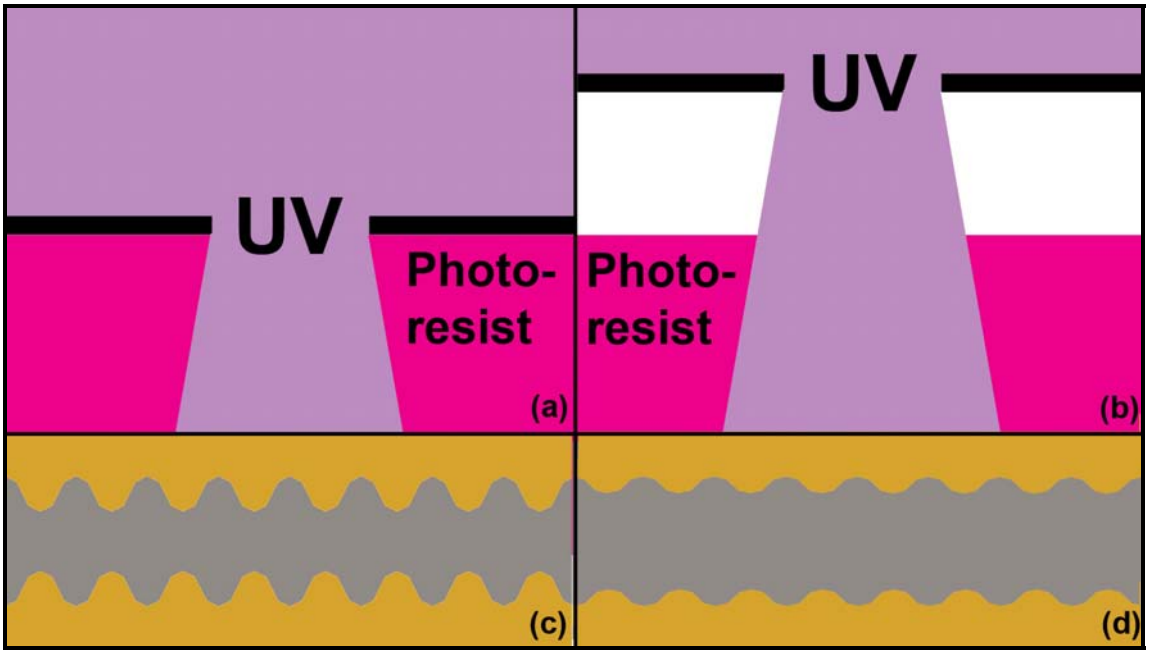

Figure 6-4 Graphic illustration of photolithography, (a) good mask contact gives (c) accurate pattern transfer. Where (b) poor mask contact causes the photoresist to over exposed, thus details in features may be lost, as it is shown in (d).

The composition of the electroplated permalloy on the prototypes was analyzed with Energy dispersive X-ray spectroscopy (EDS). This was done to ensure the prototype material matched the simulation model, as closely as possible. This allows for better evaluation of the prototypes, and for more accurate design iterations for future

prototypes. The EDS analysis result showed that the permalloy on the prototypes consisted of about 94% nickel and 6% iron. Therefore, the iron content of the electroplated material was only about one third of the ideal iron content. This discrepancy may be caused by the dissolved oxygen in the electroplating solution. As Grande and Talbot [58] have shown, the iron content in electroplated nickel-iron alloy can be raised by sparging (A process of bubbling inert gas into the solution, hence removing the dissolved oxygen.) the electroplating solution, regardless of the composition of the solution and the applied platting current density. Therefore, the lack of iron deposition in the plated permalloy can be corrected by removing the dissolved oxygen from the electroplating bath in future fabrication runs.

Another source of error for the permalloy composition may be the control of electric current density during the plating step. During fabrication, it was observed that there was permalloy deposition on the back side of the wafer. This showed that a portion of the current was getting around the edge of the wafer and reaching the back side of the wafer. Moreover, the power supply that was used in the plating step is designed for voltage controlled supply. It has poor accuracy when used in “current control” mode, and hence this also contributed to the error in current density. The composition of the plated permalloy in future devices can be more accurately controlled by using a dedicated power supply designed specifically for the electroplating application, and insulating the back side of the wafer to prevent the current leaking through this route. In addition, switching to a non-conductive wafer, such as glass, can also eliminate the current leakage to the back side of the wafer.

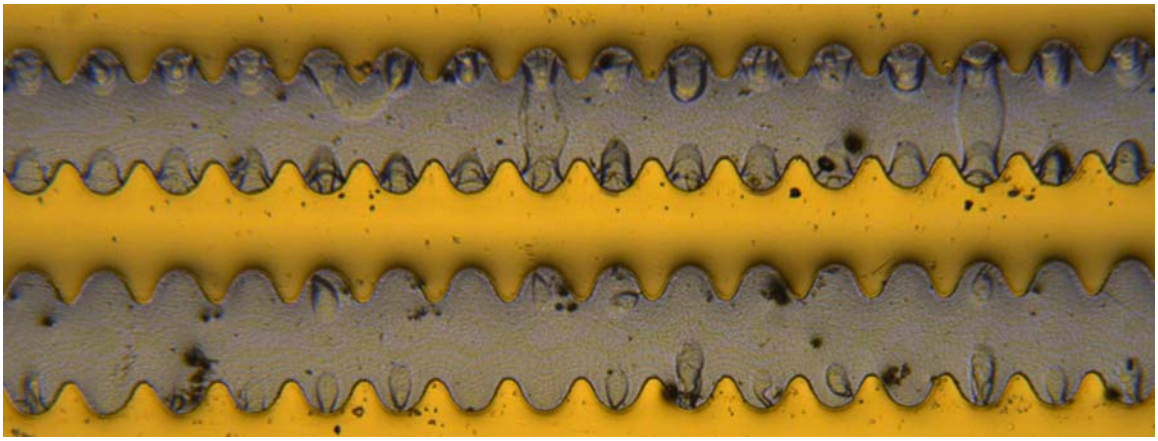

Figure 6-5 Poor SU-8 coating, notice the delaminating SU-8 at the tip of the tooth features.

Another type of defects that was found on the prototype was the shadows seen above the permalloy, as shown in Fig. 6-5. The shadows were most commonly found at the tip of the tooth features. These indicate that there was sudden change in the topography of the permalloy, either pits or humps, near the tip of the tooth features. This was most likely to be caused by the edge effect on the electric field around the tip of the tooth features. Since these features mainly occurred above the permalloy, therefore, they would not obstruct the cells in the magnetic traps optically. The features may be eliminated by lowering current density to obtain a smooth overall finish on the permalloy layer.

The problems that were encountered during fabrication are either easily solvable (seed layer incompatibility, permalloy composition, pits and humps at the tip of the tooth features) or anticipated (feature loss in electroplated permalloy due to mask issues). Some solutions have been proposed to solve these problems and should be implemented in future fabrication runs.

Chapter 7 Experiment

A series of experiments were conducted on the MSCMA prototypes to verify their performance. The results of these experiments are used for evaluation of the various characteristics of the MSCMA prototypes. The main interests include:

1. Comparison of the actual **B**-field profile on the prototype and the theoretical **B**-field profile predicted by FEM.
2. Evaluation of the cell immobilization capability of the MSCMA.
3. Evaluation of the MSCMA operation at different cell densities.

The next section will describe the equipment and materials that were used in the experiments.

7.1 Experimental Setup

In order to conduct experiments, an aluminium fixture was designed to hold the MSCMA prototype, as shown in Fig. 7-1. The purpose of the aluminium fixture was to

(i) Securely hold the two N40 magnets and the MSCMA in the desired orientation with respect to each other

(ii) Allow the assembly to fit under a bright microscope setup

(iii) Retain the fluid containing the test cells or particles on the MSCMA.

The MSCMA was secured onto the aluminium fixture by a pair of screws clamping down onto a clamping plate. In order to magnetize the MSCMA, two N40 neodymium magnets were placed in the pockets of the fixture, on either side of the MSCMA to magnetize the permalloy layer. The two magnets could easily be inserted or removed to magnetize or un-magnetize the device, as required by the experiment. The entire assembly of Fig. 7-1 was mounted on a motorized stage under a brightfield microscope,

as shown in Fig. 7-2. This motorized stage was used to position the MSCMA under the microscope in the lateral plane, with a motion resolution 1 μm. The microscope system was fitted with an infinity corrected 10X objective (Mitytoyo OBJ PLAN APO HR 10X) with a numerical aperture (NA) of 0.28. The objective was connected to a 2/3" colour CMOS camera (PixelLink PL-742) through a 1X camera-objective coupling. The resulting optical system had a field of view of 1280 μm × 960 μm, an optical resolution of 1 μm, and a depth of focus of 3.5 μm.

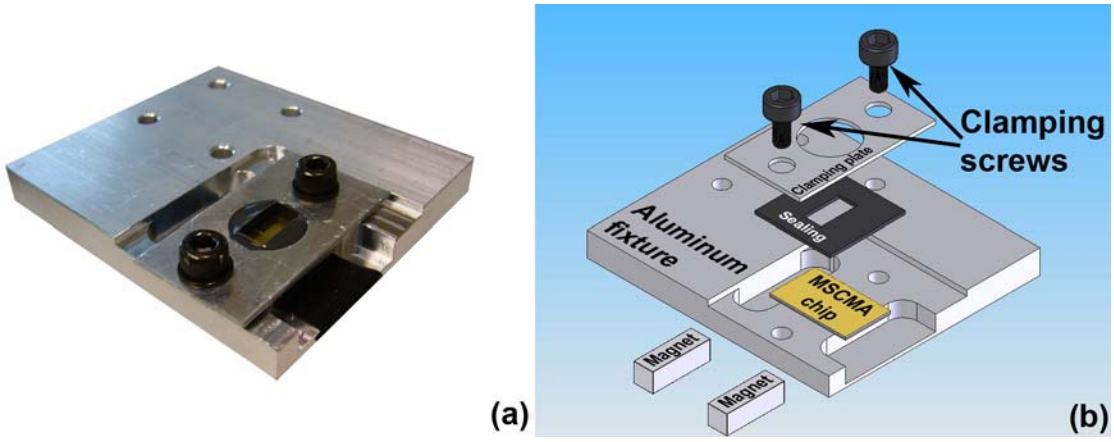

Figure 7-1 (a) The aluminium fixture MSCMA assembly, and (b) the 3D illustration of the same assembly.

In order to place fluid samples onto the MSCMA and to prevent the fluid from spilling over the sides of the device, a 'sealing system' had to be developed. The sealing system consisted of a piece of silicone elastomer sealing (as shown in Fig. 7-1(b)), that was placed between the aluminium clamping plate and the MSCMA. This created a 'side wall' around the perimeter of the MSCMA, and hence would retain the fluid above the device. The silicon elastomer sealing was cast from a Dow-corning Slyguard 170 elastomer resin kit. The resin was dispensed from the package through a mixer tube into the casting mould. The casting mould, was then placed on a hotplate at 70 degree Celsius for 15 minutes to cure the resin.

7.2 Cell Preparation

In order to verify the arraying performance of the MSCMA prototypes, actual biological cells were released over the MSCMA while it was magnetized and non-magnetized. Jurkat cells were used for testing in these experiments, which are a type of specially grown human T lymphocyte cell used for research purposes. Jurkat cells were selected for a number of reasons. Firstly, they are a non-adherent cell type, which is generally the cell type that the MSCMA was designed to work with. Moreover, Jurkat cells are widely used in biomedical research, such as cancer drug research. Thus, they are representative of the cell types that the MSCMA may encounter in future applications. Therefore, it is particularly valuable to prove the operational concept and performance of the MSCMA with Jurkat cells.

The procedure to prepare a sample of live Jurkat cells for testing of the MSCMA is now described A sample of $1x10^6$ cells/100 μL Jurkat cells was cultured in 10% FBS (Fetal Bovine Serum, GIBCO #16000-044), and 90% completed Roswell Park Memorial Institute (RPMI) growth medium (GIBCO, #21870). This was mixed with EasySep® Human CD3 Positive Selection Cocktail (StemCell Tech #18051C.1) at a 1:10 volume ratio and incubated at room temperature for 15 min. Then EasySep® Magnetic Nano-particles (Provided by StemCell Techologies, #18150) were mixed in and incubated at room temperature for another 10 min. Low serum growth medium was then added to the mixture to further dilute the mixture. This mixture was then put through three magnetic activated cell separation cycles. A proper amount of low serum growth medium was added to the enriched cells to recover the cells and re-suspend the cells at the desired cell density.

For some of the experiments, live Jurkat cells were not necessary. In these cases, “fixed cells” were used, which are cells that are preserved with formaldehyde cross linking. These cells were prepared by suspending Jurkat cells in the “fixing solution”, 4% paraformaldehyde in phosphate buffered saline, for 15 minutes. The cells were then taken out and rinsed twice with phosphate buffered saline, before they were stored in the same solution.

7.3 Experiment Procedure

Two different types of experiment were conducted to examine the performance of the MSCMA prototypes. These were (a) particle distribution tests and (b) cell arraying tests.

The particle distribution tests were conducted to visualize the magnetic field around the MSCMA. This experiment was carried out in a similar way as the century old “iron filings around a magnet” experiment. However, instead of large iron filings, micron sized magnetic particles (StemCell Tech #19250) were used. Before a particle distribution experiment, 2.5 μL of the magnetic particle solution was mixed with 0.6 ml of distilled water to reduce the particle density in the solution. The solution was then transferred onto the surface of the MSCMA using a pippettor, while the device was held in the aluminium fixture, under the microscopy system. At time corresponding to $t = 0$, the N40 neodymium magnets were placed on either side of the MSCMA to magnetize the permalloy pattern. The behaviour of the particles was then observed and recorded through the computer that is connected to the microscope camera.

The cell array experiments were conducted to evaluate the performance of the MSCMA. In these experiments, the Jurkat cells were prepared as described in the previous section. The cells were loaded onto the MSCMA prototype using a pippettor,

while the device was held in the aluminium fixture under the microscope. After the solution of suspended cells was loaded onto the MSCMA, the MSCMA was magnetised by putting the neodymium magnets into the pockets on the fixture. The behaviour of the cells was then observed and recorded using the microscope camera.

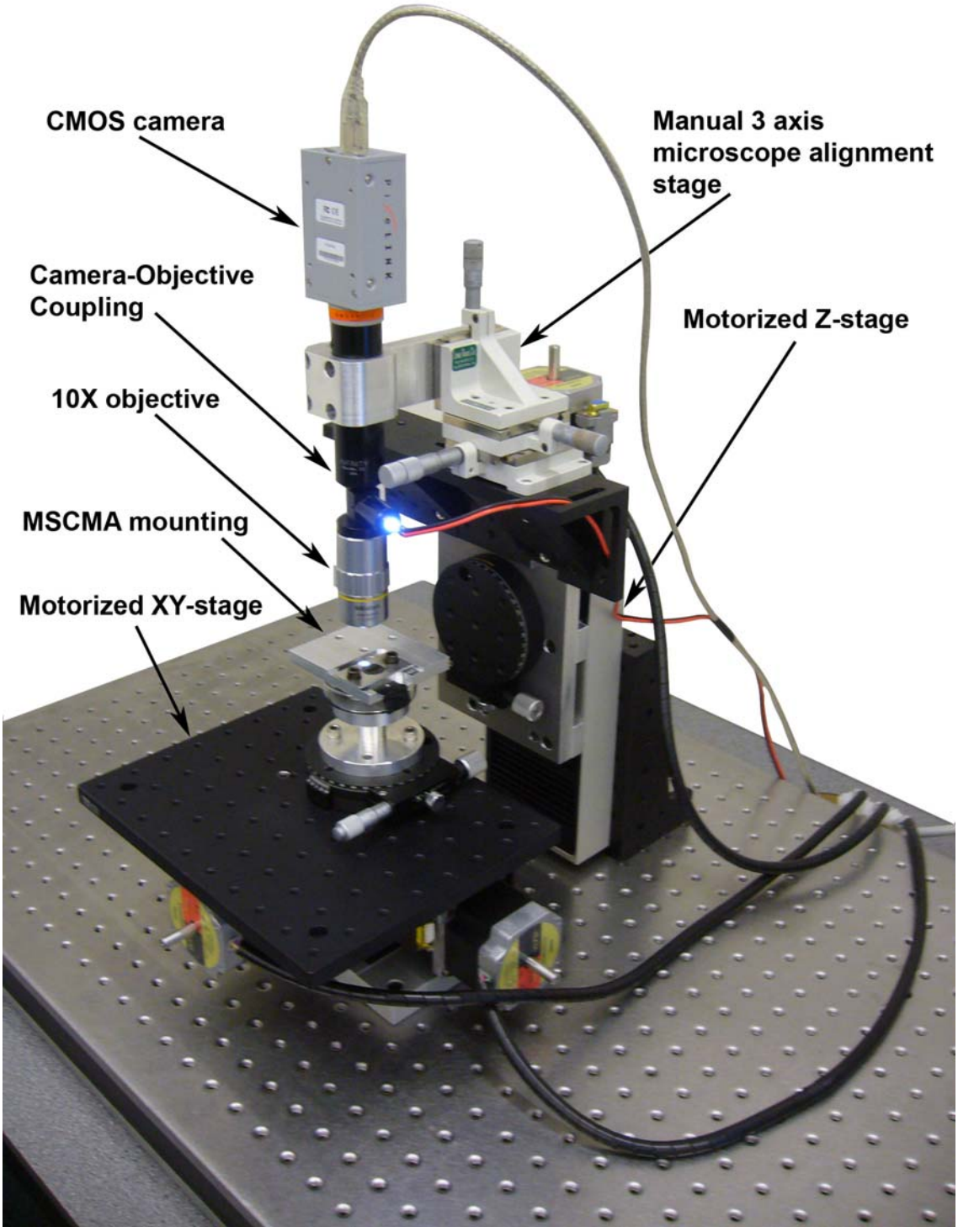

Figure 7-2 Experimental setup.

Chapter 8 Results and Discussion

Experiments performed using the MSCMA prototypes provided valuable information about their operation and characteristics. The results of these experiments are presented in this section, and are discussed and analyzed. Improvements for future revisions of the prototypes are also suggested.

8.1 Magnetic Particle Arraying Experiment

In order to evaluate the magnetic field profile around the magnetic traps, micro-particles, one micron in size, were allowed to collect onto the magnetized MSCMA prototypes. Fig. 8-1 shows two time-lapse microscope images of the MSCMA before and after this experiment. Fig. 8-1(a) was captured just before the MSCMA was magnetized with the particles suspended in solution above the substrate. Fig. 8-1(b) was captured 3 minutes later, when the magnetic particles gathered at the magnetic traps, as was predicted by the FEM result. Fig. 8-2 and 8-3 show a series of time-lapse images of a device during a magnetic particle experiment. As shown in the first few frames of Fig. 8-2, as soon as the MSCMA was magnetized, the particles quickly gathered in the magnetic traps. The particles first clustered around the edges of the magnetic traps, which was the location predicted during FEM simulation to have the most intense **B**-field. Particles that arrived at the magnetic traps subsequently would gather around the existing particles. As more and more particles gathered at the magnetic traps, the magnetic trap would eventually become over-filled with magnetic particles. After it was over-filled, the particles would start gathering over the top of the permalloy lines and cluster between the bottoms of the magnetic traps, shown in the later frames in Fig. 8-2 and Fig. 8-3. This also correlates with the FEM simulation, where these regions have a high magnetic flux

density next to the magnetic traps. As more particles were gathered in this region, the particles would bridge the separation between the magnetic traps on either side of a permalloy line. Notice that, the bridging effect only happened in the direction across the permalloy line. But the same effect was never observed between two adjacent magnetic traps on the same side of the permalloy line. In general, the particles behaved as expected, given the FEM simulations of magnetic field. Note that some particles sunk and stuck to the surface of the gold in the beginning of the experiment, before the magnets were used to magnetize the device. This is evident since they appear at the same location in the frames marked $t = 0$ sec and $t = 135$ sec.

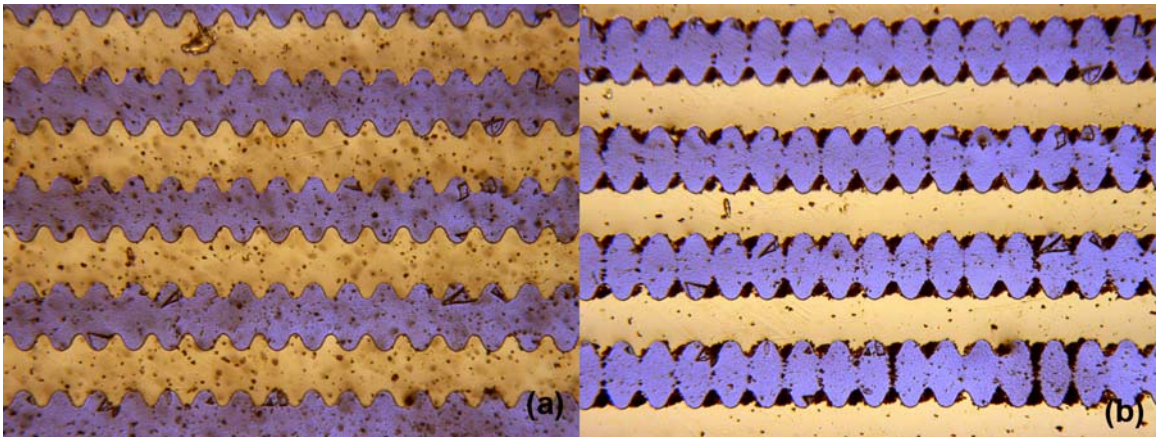

Figure 8-1 (a) Magnetic particles on the MSCMA before magnetization and (b) after magnetization.

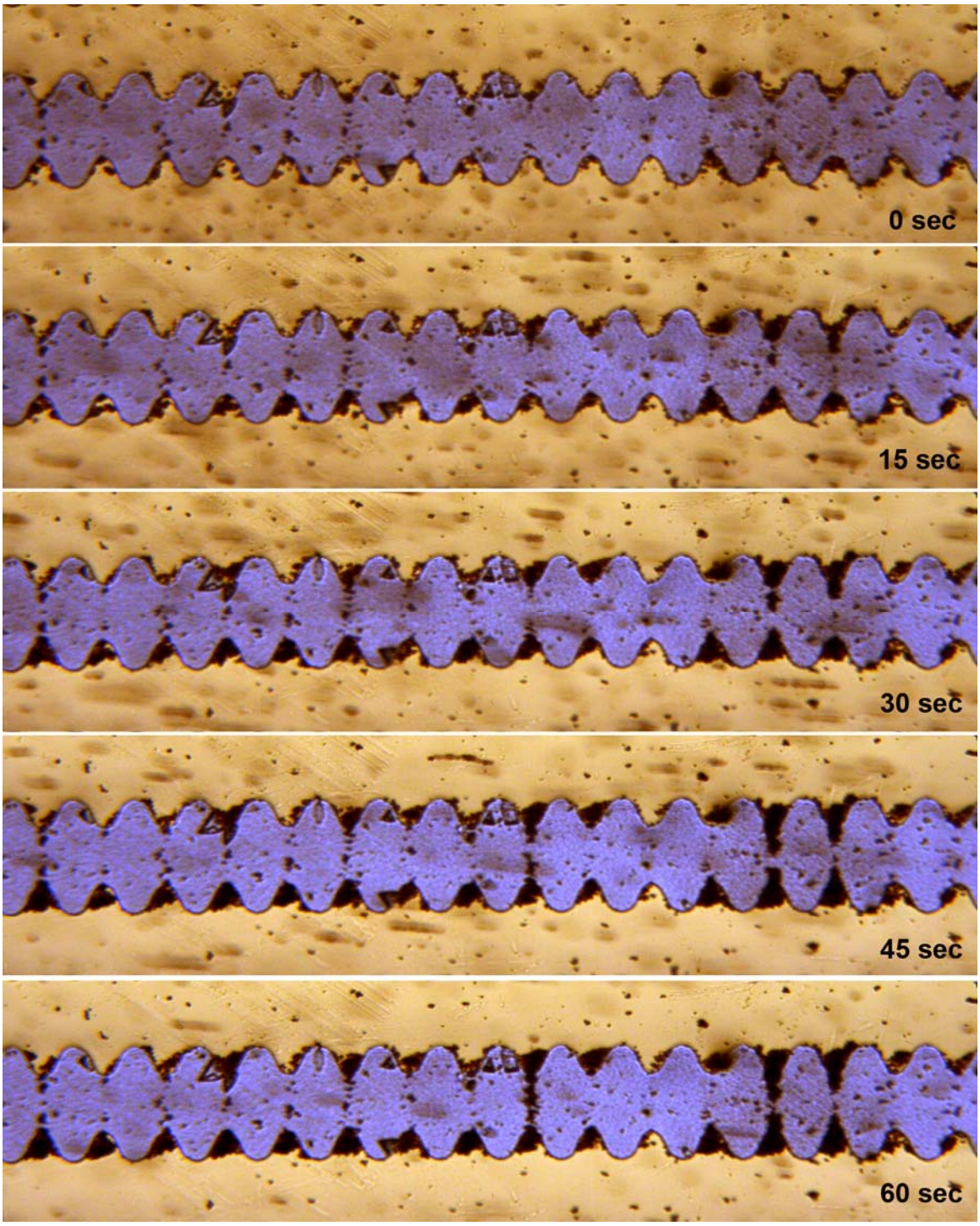

Figure 8-2 Sequence shot, from 0 sec till 60 sec of arraying magnetic particles both design. The first frame was taken shortly after the device was magnetised

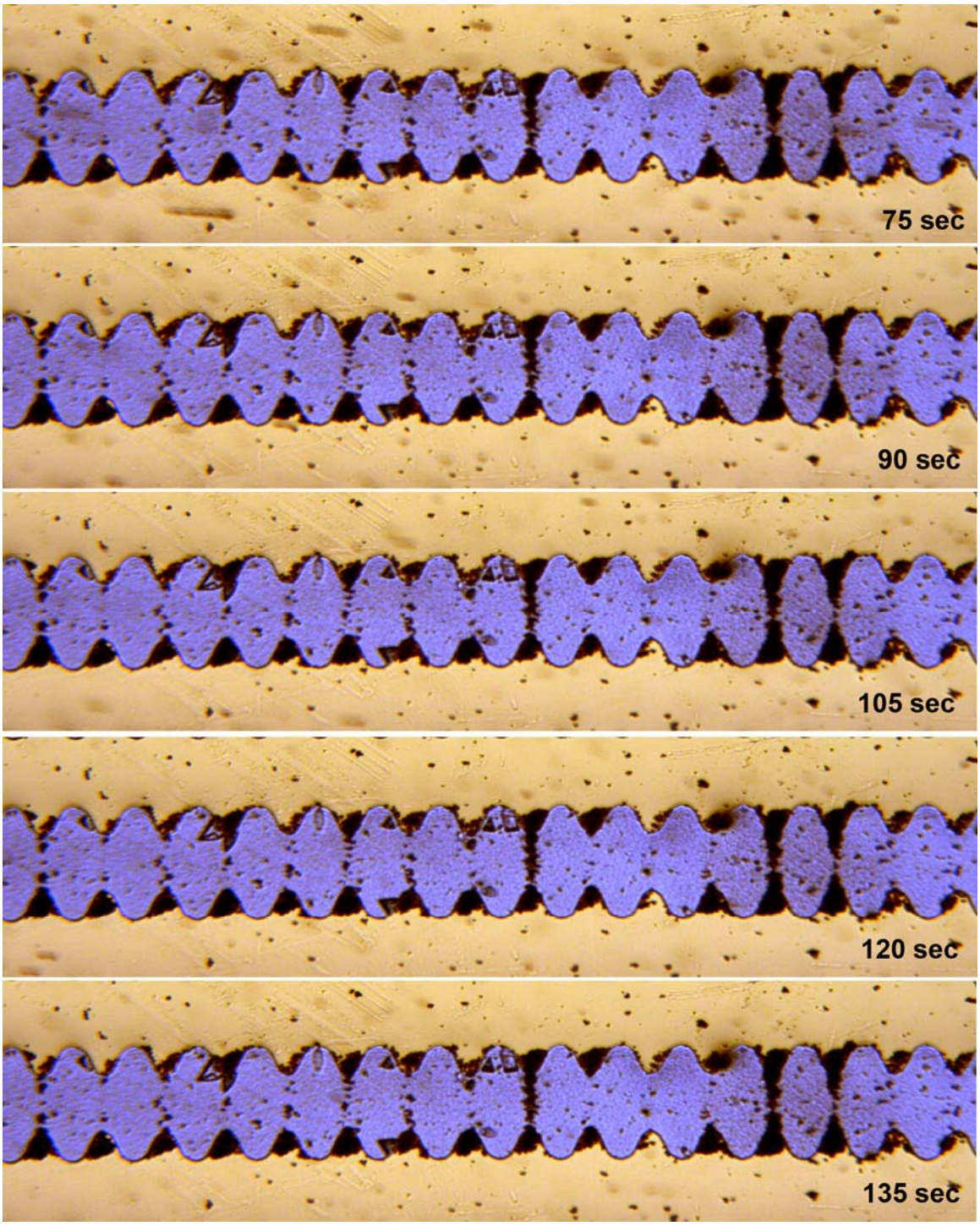

Figure 8-3 Sequence shot, from 75 sec till 135 sec of arraying magnetic particles both design.

8.2 Cell Arraying Experiments

The MSCMA prototypes were also tested for their ability to array Jurkat cells tagged with immunomagnetic labels. Fig. 8-4 shows two images captured during two typical cell arraying experiments. In Fig. 8-4(b), the experiment was ran with Jurkat cells that were not tagged with immunomagnetic labels. The control experiment, shown in Fig 8-4(a), was ran with Jurkat cells that were not tagged with immunomagnetic labels. As the images show, cells that were tagged with the magnetic labels would land on the magnetic traps, while the cells that were not tagged would just land randomly on the surface of the device. During the fabrication of the early MSCMA prototypes, some fabrication defects were present on the devices, as can be seen on the permalloy layer of the MSCMA in Fig. 8-4. It was observed that these defects have little effect on the functionality or performance of the device.

Fig8-4 shows that in the majority of the magnetic traps, more than one cell was captured. There were two scenarios that lead to this consequence. In the first scenario, it was observed that some of the cells were clustered together prior to entering the magnetic traps. Clusters are commonly formed among cells, however, the strength of the bonds that link the cells in a cluster are usually weak. The clusters of cells that are formed prior to the experiment may be broken down by gently and thoroughly aspirating the medium. In the second scenario, multiple cells were progressively trapped in a single magnetic trap over time. This was an accumulative process, like the behaviour of the magnetic particles. At a high cell density, the number of available magnetic traps is far less than the number of cells. Thus cells that cannot reach an empty trap would just attach to the cells that have already settled into a trap. This is similar to the situation of the magnetic particles attach themselves onto other particles that are already in a magnetic trap. In fact, cell clusters

formation in a cell capturing site is a common observation in different types of cell arrays. The average number of cells in a cluster is proportional to the cell density. The distribution of the number of cells per site follows a Poisson distribution in relation to the cell density (volumetric) and the array density (surface). [15,26]

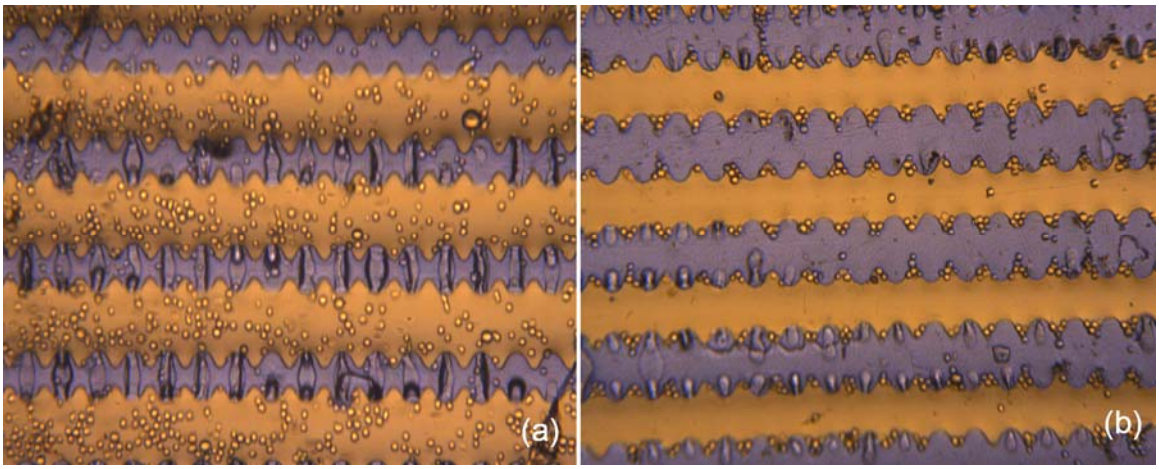

Figure 8-4(a) Cells without immunomagnetic labels and (b) cells with immunomagnetic labels over the magnetized MSCMAs.

Attempts were made to lower the number of cells in each magnetic trap, towards the goal of capturing a "single cell" per magnetic trap. This was done by repeating the experiments with a diluted cell density in the sample solutions. 20 μL of the original solution of evenly suspended cells, as described in section 7.2, was mixed with 250 μL of buffer solution and then put onto the MSCMA prototype. Fig. 8-5 provides a comparison of images of the cells arrays using the two different cell densities. Notice that the reduced cell density shown in Fig. 8-5(b) significantly reduced the number of cells at each magnetic trap. Except for the big cell cluster in one of the traps, majority of the traps had one to three cells in the trap. Inspection of the time-elapsed images of this experiment, shown in Appendix D, reveal that the big cell cluster was likely formed prior to entering the magnetic trap, since it appears suddenly at time t = 15 sec. As the images sequence in Fig. 8-6 shows, the cells were generally captured one at a time in each trap. Cells that

subsequently flowed by the occupied magnetic traps might be pulled into the traps under the influence of the magnetic field around the magnetic traps. No significant difference was observed on the strength of magnetic influence between occupied and empty magnetic traps. Cells seemed to fall into an occupied or an empty magnetic trap by chance, with no observable preference for cells to fall into either an empty trap or an occupied one. In fact, after 8 minutes into the experiment, there were still empty magnetic traps in the array, though most of magnetic traps were occupied. After the 8 minutes, there were no longer an observable cells settling out of the solution, and hence it was presumed most of the cells had settled out of the solution.

Another observation to be made about these images is that, like the magnetic particle experiments, a small number of cells landed outside of the magnetic traps. Some of these cells had sunk randomly and stuck to the surface of the device before the device could be magnetized. However, some cells did land on the surface of the device and became stuck during the experiment. It is evident that the strength of the **B**-field gradient in these locations is insufficient to "pull" the cells into the traps. Since the cells remained stuck to the bottom through out the experiment, there was some amount of adhesion force between the SU-8 surface and the cell membrane, which prevented the cells from rolling or sliding along the surface under the influence of the magnetic field. This effect was particularly noticeable in the area between the two permalloy lines, since the gradient of the **B**-field is the shallowest in this area, as predicted by the FEM simulations. Given the shallow **B-**field gradient, and thus the weak magnetic force on cells, cells that landed in this "dead zone" would very likely stick due to surface adhesion and never move again.

Overall, this adhesion between the SU-8 and the cells may hamper the performance of the device as the cells are prevented from reaching the desired location in an array.

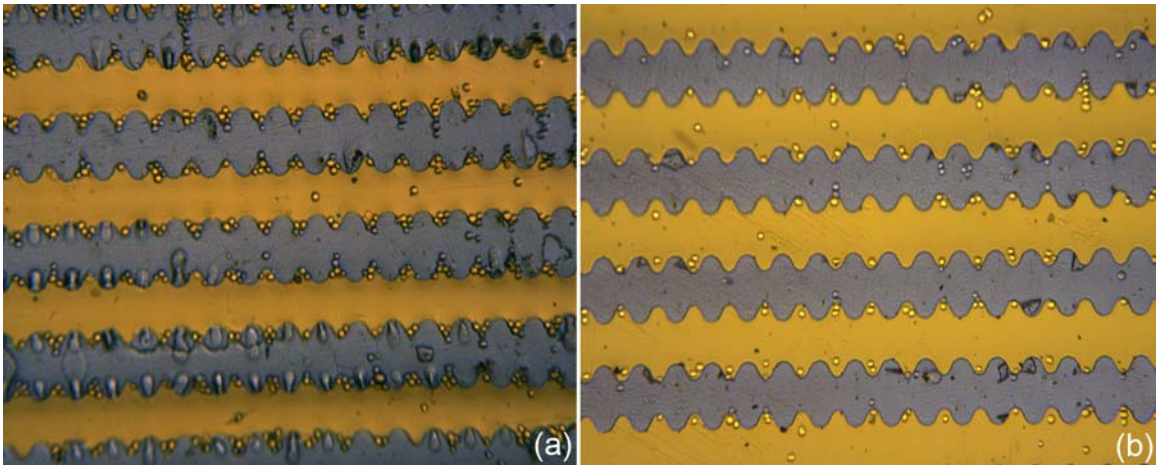

Figure 8-5 Comparison of MSCMA cell arrays that operate at (a) original cell density, (b) diluted cell density.

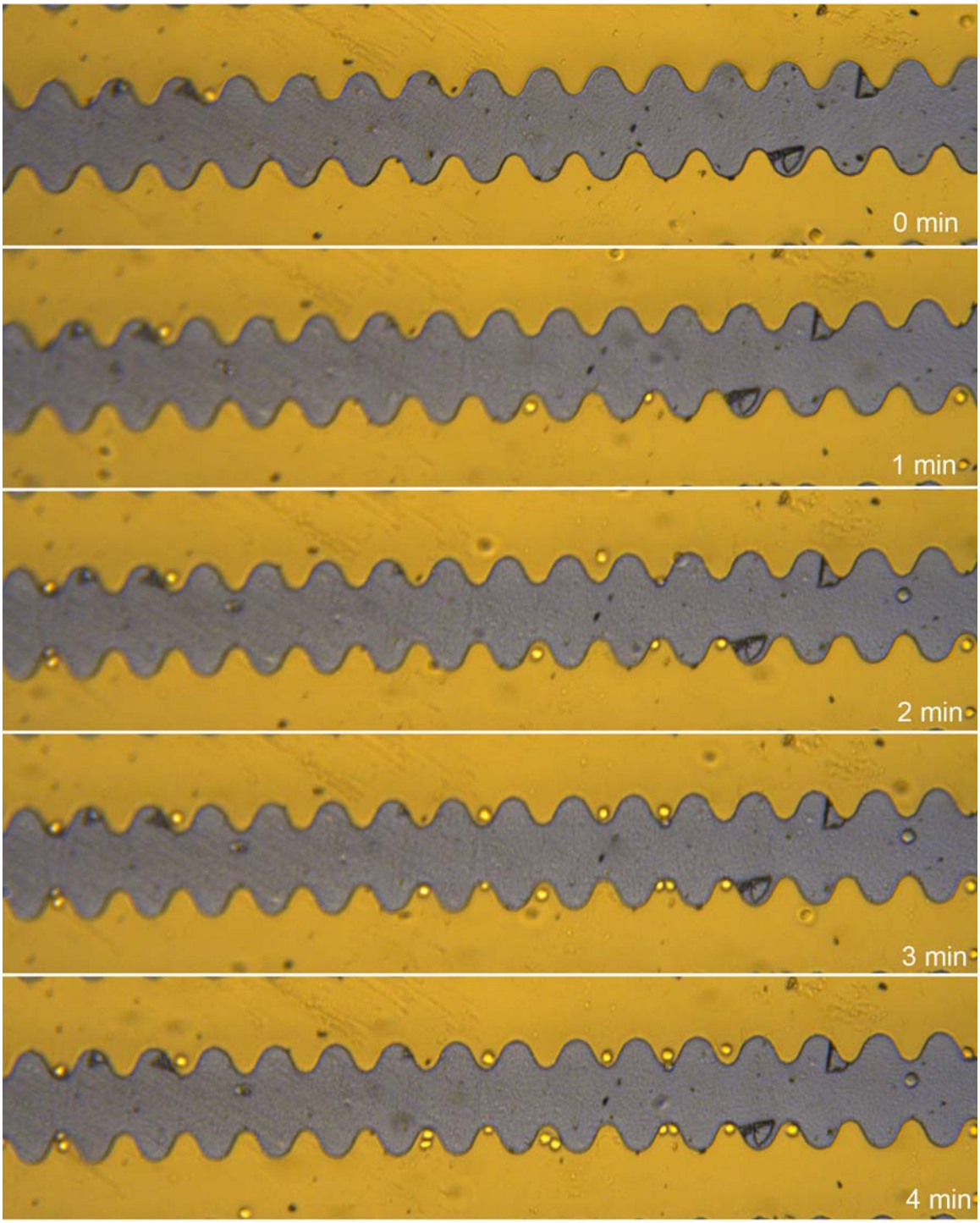

Figure 8-6 Time-lapsed images, from the beginning of the experiment, to 4 minutes, taken over a single permalloy line of the MSCMA. The 0 minute image was taken right before the device was magnetized.

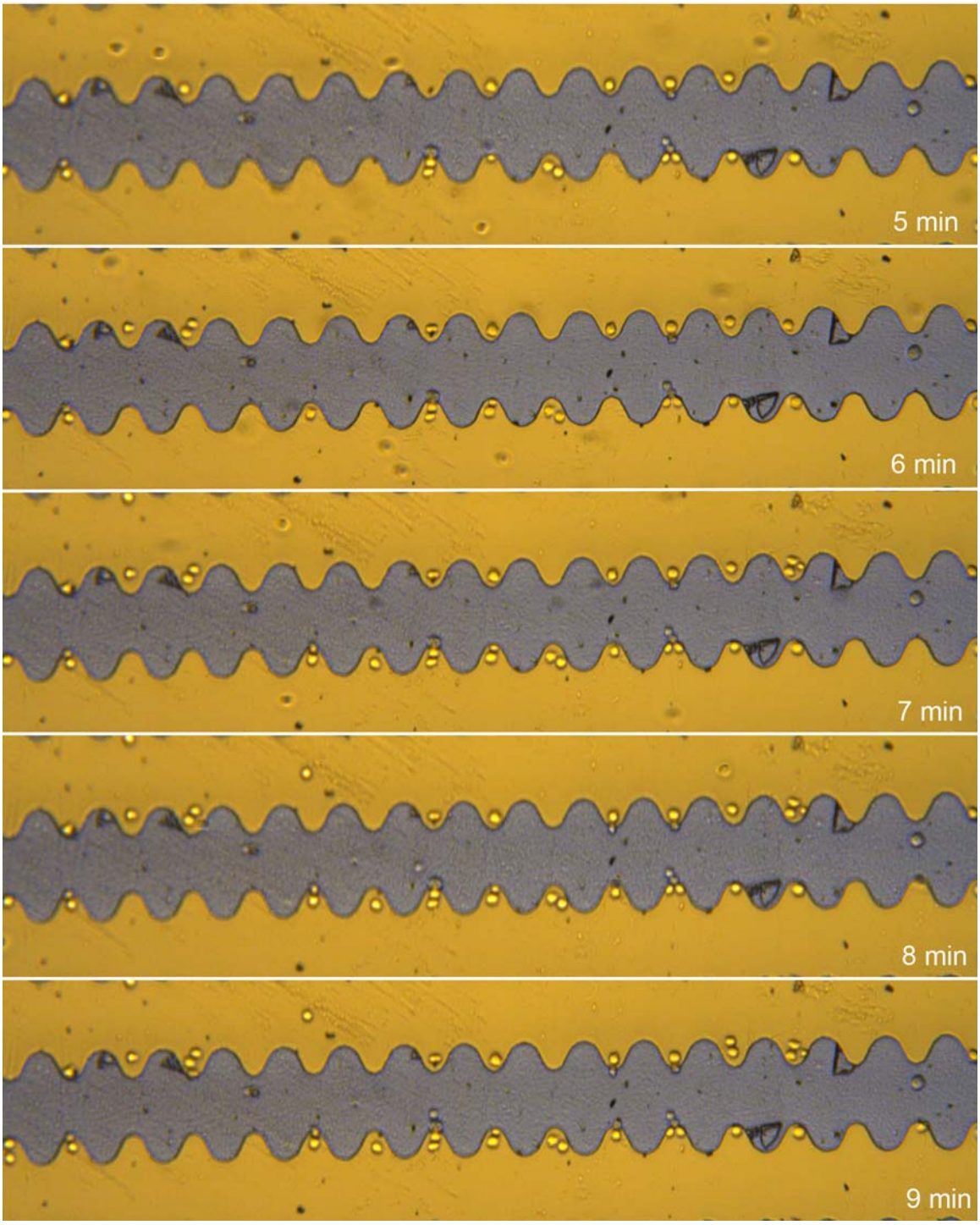

Figure 8-7 Time-lapsed images, from 5 minutes to 9 minutes during the experiment, taken over a single permalloy line of the MSCMA.

When an experiment was completed, the N40 magnets were removed from the MSCMA, and hence the device was demagnetized. The device was then rinsed by using a pippettor filled with buffer solution, and successively draining and filling the MSCMA.

This was done to rinse the surface of the MSCMA in an effort to remove the cells from the magnetic traps. Although the cells did not immediately move away from their traps upon the removal of the magnets, most of the cells were successfully removed during the rinsing process. Some of the cells were left on the surface of the device, but were nonetheless removed from the magnetic traps. This is because the pipette was not able to completely remove the fluid from the chamber, thus the cells that were suspending in the left over fluid sank to the surface of the chamber after the fluid stopped flowing. This result shows that it is possible to remove the cells from the MSCMA after demagnetizing the device.

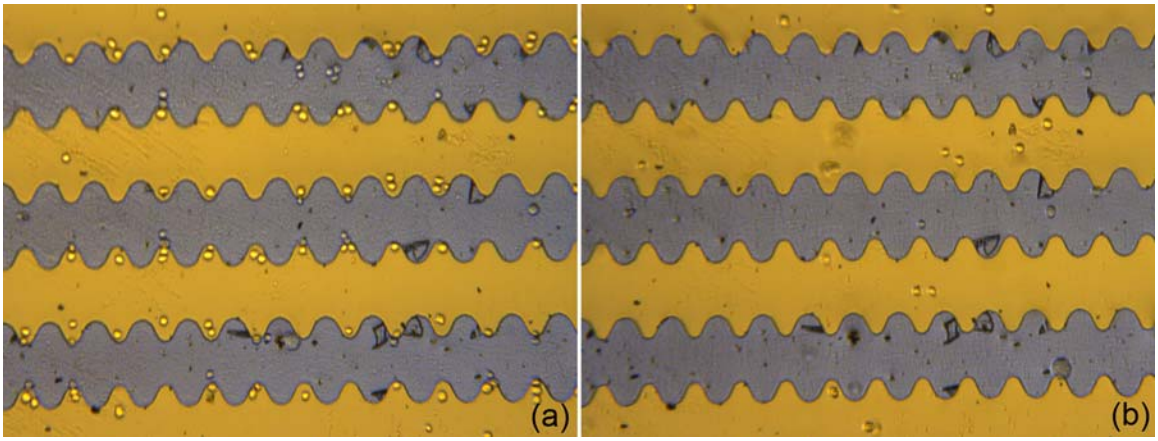

Figure 8-8 Cells on the MSCMA (a) before and (b) after it was rinsed with the buffer solution.

8.3 Discussion

In general, the MSCMA prototypes preformed as anticipated. Both the magnetic particles and immuno-magnetically labelled cells were collected at the magnetic traps, as predicted by the FEM analysis. Although both the magnetic particles and the immuno-magnetically labelled cells settled at the magnetic traps under the influence of the applied magnetic field, the movement of the cells was noticeably slower than the magnetic particles. As discussed in section 4.1, a micro-object that is suspended in a fluid medium

will experience hydrodynamic drag that is proportional to its size. On the other hand, the magnetic force on any material is proportional to its volume and magnetic susceptibility, as discussed in section 3.2. Since the cells are generally diamagnetic, their magnetic susceptibility is negligibly small. Therefore, the magnetic force on the immuno-magnetically labelled cells is contributed solely by the nano-particles that are attached to the cell surface, as it was proved by the above experiments. Since the volume of the nano-particles (nominal diameter = 170nm) is considerably smaller than that of the micro-particles (nominal diameter = 1μm), the magnetic force that a nano-particle is capable of generating is also considerably smaller than that of the micro-particles. On the other hand, the nominal diameter of the cells is roughly 15 times that of the micro-particles, thus the hydrodynamic drag on the cells is considerably higher than that of the micro-particles. The combined effect of the higher drag and lower magnetic force means that the cells could only travel at a fraction of the speed of the micro-particles. Therefore, the response of the cells to the applied magnetic field was a lot slower than the micro-particles, as was observed during the experiments, and shown in Fig. 8-2 and 8-6.

As mentioned by other researchers, the distribution of the number of cells at a cell capturing site, on a cell array, follows a Poisson distribution in relation with the cell density and array density. [15,26] Therefore, the mean number of cells at each cell capturing site increases with the cell density, and decreases with increase in the array density. In other words, the chance of getting only one cell in each array site increases with the ratio of cell capturing site density to cell density, since there is a better chance for a cell to come across an empty array site. Fig. 8-5 shows that lowering the cell density does lower the number of cells at each magnetic trap. However, it also increases the

likelihood of empty magnetic traps at the end of the experiment. This will effectively reduce the efficiency of the MSCMA since it reduces the number of cells that can be held on the MSCMA in each experiment. In order to maintain the number of cells that can be held on the MSCMA, while also achieving single cell array, it is necessary to increase the array density as well as decreasing the cell density.

In order to increase the array density, modifications must be made to the current design of the permalloy lines, such as shrinking the size of the tooth features on the side of the permalloy lines and placing the permalloy lines closer together. As described in Section 5.5.2, shrinking the size of the tooth features has very little effect on the profile of the **B**-field around the magnetic traps other than scaling it down. Therefore, the tooth features that are scaled down should theoretically maintain their function, while increasing the array density. An additional benefit may be that by increasing the array density the chance of cells sticking in the **B**-field "dead zone" between the permalloy lines is reduced. Since the permalloy lines could be placed closer together, consequently, the "dead zone" is effectively shrunk since the size of the cells remains the same. Therefore, the cells are more likely to come within the influence of the high gradient field around the magnetic traps. However, there are also draw backs of shrinking the features on the permalloy line. First of all, shrinking the features means the fringing magnetic flux, as described in Section 5.5.2, would stay closer to the surface of the permalloy. Therefore, the influence of the fringing magnetic flux would be more confined and hence less able to "pull" cells in from a distance, than that of the permalloy lines that have larger features. Secondly, the physically distance between the magnetic traps will become smaller, therefore, it is easier for the cells to bridge across the separation between the traps. This

effect could be minimized by ensuring that the width of the permalloy lines is designed sufficiently large, since the bridging effect has only been observed in the direction across the permalloy lines.

8.4 Future Work

In order to further develop the MSCMA device, it is recommended that the prototypes be revised and that further experimentation should be done to characterize the relationship between number of cells per magnetic trap and:

1. Cell density
2. Array density
3. Tooth and line features geometry
4. Tooth and line features dimensions

Characterization of these parameters will involve fabricating new prototypes, conducting experiments and collecting statistical information. The information that is particularly valuable to the development of the MSCMA design includes:

1. The number of cells per magnetic trap
2. The number of cells per magnetic trap in relation with the location of the trap on the device
3. Length of time required for the completion of a cell array

There are also other issues that should be considered in further development of the MSCMA. First of all, the SU-8 polymer used to coat and protect the MSCMA created significant cell adhesion. This adhesion force prevented some cells from reaching a magnetic trap, therefore reduced the overall number of cells reaching the magnetic traps. In order to prevent the cells from sticking to the surface of future prototypes of the

device, different coating materials and surface treatment should also be tested on the future prototypes.

Secondly, effort should be made into developing a transparent version of the MSCMA. This should be done so that the MSCMA would be compatible with transmitted light optical microscopy systems, as well as reflected light systems. Modifications for creating the transparent version were discussed and documented in Chapter 6. The modified fabrication process, along with the modified design should be implemented, and evaluated in future fabrication runs.

If a transparent version of the MSCMA can be developed, it can provide expanded functionality when integrated other tools, in addition to transmitted light microscopes. Recently, Sakaki *et al*. [70, 72] developed a robotic micro-manipulator for handling and injecting various materials into biological cells over a transmitted light microscope. A system that combines the MSCMA and the robotic micro-manipulator would be able to assign addresses to captured cells, and track their response to various stimuli over time, using the microscopy system. In addition, the cell can also be manipulated and injected depending on the type of research required. The two systems would be complimentary, because the structured environment created by the MSCMA (i.e. anchoring the cells at know locations) can reduce the computational load of the control system of such an automated system.

As described in Section 8.2, removal of the cells from the MSCMA was shown to be possible after the magnetic field was removed, and a rinsing process used. However, merely removing the cells provides little value for biological experiments, since the whole MSCMA will quite likely be discarded after an experiment. In contrast, being able

to collect viable cells after an arraying experiment and culturing them for further experiments is extremely valuable for biological experiments. Ino et. al. [15] have demonstrated the possibility of collecting cells with a glass micro-pipette. Alternatively, cells can be encapsulated, transported and incubated in hydrogel encapsulation without the use of a micromanipulator. Albrecht et al. [26] has successfully used hydrogel to encapsulate and incubate cells in their DEP cell array. However, they have used UV in curing the hydrogel, which means their process may not be suitable for all cell types. Regardless, it is recommended that a cell recovery protocol should be developed for the MSCMA prototypes, since this can be a very valuable process for many biological experiments.

Due to the lack of suitable equipments, viability of cells in the MSCMA was not evaluated during the experiments. Moreover, all the experiments discussed in this work were conducted in an environment where the temperature, humidity and carbon dioxide content were not controlled. The lack of controlled in these parameters would kills the live Jurkat cells very quickly. Therefore, the cells would never last long enough for evaluation of long-term viability in the MSCMA. Further experiments should be conducted to evaluate the short-term and long-term viability of cells in the MSCMA. In many cell experiments, researchers are interested in observing the cell behaviours over a period of time, for example the response of the cells to the introduction of a drug. There is little value in having the cell array for such experiments, if the cells cannot stay alive in the array for the length of the experiment. These viability experiments should be done in conjunction with the development of the cell recovery protocol, since there is no point of recovering the cells if the recovery process may kill the cells itself. Ultimately,

integration of the MSCMA with cell incubation equipment is necessary to fully explore the potential of single cell experiments on the MSCMA.

Chapter 9 Conclusion

In the past, researchers have invested a lot of time and effort toward studying single cell behaviour. Single cells have been shown to exhibit behaviour which is quite different than the data that was provided by averaged measurements of bulk cell samples. With advances in technology, more and more tools have become available for studying single cell behaviour. For example, flow cytometry, the more advanced laser scanning cytometry, and automated microscopy, have all expanded the research capability of researchers. However, with all these advances in technology and equipment, localizing individual cells and identifying them still remained difficult.

In recent years, researchers have developed various forms of cell arraying devices using micro-fabrication technology. With these cell arrays, localizing cells became less of a problem, since the location of the cells can be predetermined. Moreover, as the cells are immobilized on the array, it becomes possible to identify each cell by its location on the array. In addition, cells are usually physically isolated from each other in these arrays. Therefore cell to cell interaction can be eliminated, thus it is easier to control the experimental environment.

Magnetic field induced force is commonly used as a mechanism of cell manipulation. By attaching immunomagnetic labels to biological cells, cells can be magnetized and manipulated with an applied magnetic field. This thesis has presented the development of a novel Magnetic Single Cell Micro Array (MSCMA). The design, FEM simulations and experimental verification of the proposed MSCMA were presented.

The MSCMA is able to capture cells that are suspended in the medium above the device, and place them into an array by using a magnetic field that becomes concentrated

at specific points. The MSCMA was designed to create this suitably shaped **B-**field profile to fulfill this purpose. The proposed MSCMA design utilizes an "off-chip" magnetization source and the "on-chip" permalloy lines to generate the suitable magnetic field profile for the cell arraying task. Not only is this configuration simple to fabricate, it also allows for the future possibility of a transparent substrate. Therefore the use of transmitted light microscope may be possible.

The design of the MSCMA was analysed thoroughly in a series of FEM simulations before the prototypes were fabricated. From these simulations, it was determined that simply placing the magnets on the side of the MSCMA, with the north pole of one magnet facing the south pole of the other, would provide adequate magnetization to the MSCMA. The geometry of the permalloy lines was also analysed in these FEM simulations. It was found that non-uniformity in the thickness of the permalloy lines has very little effect on the magnetic field around it. Moreover, size of the features on the permalloy lines also has little effect on the magnetic field profile. Therefore, these features can be scaled easily without affecting the functionality of the device.

A batch of prototypes of the opaque version of the MSCMA were fabricated and experimentally tested to evaluate the concept and the performance of the device. In the experiments, the prototypes of the MSCMA preformed as expected. Tests using simple magnetic particles revealed the behaviour of the magnetic field created by the MSCMA, which matched the simulation results very well. Cells were also used in experiments, and were successfully captured on the prototypes. Cells were generally found in the magnetic traps that were predicted by the FEM simulations. Experiments with the first batch of prototypes showed that the magnetic traps will often capture multiple cells. Tests showed

that the number of cells in each magnetic trap can be controlled by the cell density. To improve the MSCMA, some proposals for future work were made based on the above experimental results. This includes: (a) modifications to the design of the permalloy lines to improve the ability of the device in creating a single cell array, (b) a transparent version of the MSCMA to allow for integration with other experimental equipment such as a micromanipulator, (c) the development of a cell recovery system to collect cells from the MSCMA, and (d) the development of a cell incubation system to maintain cell long-term viability on the MSCMA.

It is also recommended that further experiments be conducted to further characterize the single cell arraying performance of the revised MSCMA designs in relation to: (i) cell density, (ii) array density, (iii) tooth and line feature geometry, and (iv) tooth and line feature dimensions.

The MSCMA presented in this paper is a valuable tool for conducting single cell experiments, which has the potential to widen our view and understanding of cell behaviour. Its functionality and potential is shown in this thesis. With the proposed future work, the MSCMA can be turned into a complete and versatile single cell analysis and manipulation system. Such system will be greatly beneficial to cell biology and biomedical research.

Reference

[1] D. Di Carlo, and L.P. Lee, "Dynamic single-cell analysis for quantitative biology," Analytical Chemistry, vol. 78, pp. 7981-7925, 2006.

[2] B.P. Helmke, and A.R. Minerick, "Designing a nano-interface in a microfluidic chip to probe living cells: Challenges and perspectives," PNAS, vol. 103, no. 17, pp. 6419-6424, 2006.

[3] A. Deutsch, N. Zurgil, I. Hurevich, Y. Shafran, E. Afrimzon, P. Lebovich, and M. Deutsch, "Microplate cell-retaining methodology for high-content analysis of individual non-adherent unanchored cells in a population," Biomedical Microdevices, vol. 8, pp. 361-374, 2006.

[4] H.A. Svahn, and A. van den Berg, "Single cells or large population?" Lab on a Chip, vol. 7, pp. 544-546, 2007.

[5] W. Huang, F. Ai, Z. Wang, and J. Cheng, J., "Recent advances in single-cell analysis using capillary electrophoresis and microfluidic devices," Journal of Chromagtography B, vol. 866, pp. 104-122, 2008.

[6] Z.E. Perlman, M.D. Slack, Y. Feng, T.J. Mitchison, L.F. Wu, and S.J. Altschuler, "Multidimensional drug profiling by automated microscopy," Science, vol. 306, pp. 1194-4498, 2004.

[7] X. Li, and P.C.H. Li, "Microfluidic selection and retention of a single cardiac myocyte, on-chip dye loading, cell contraction by chemical stimulation, and quantitative fluorescent analysis of intracellular calcium," Analytical Chemistry, vol. 77, no. 14, pp. 4315-4322, 2005.

[8] D. Castel, A. Pitaval, M. Debily, and X. Gidrol, "Cell microarrays in drug discovery," Drug Discovery Today, vol. 11, pp. 616-622, 2006.

[9] A. Gomez-Hens, and M.P. Aguilar-Caballos, "Modern analytical approaches to high-throughput drug discovery," Trends in Analytical Chemistry, vol. 26, no. 3, pp.171-182, 2007.

[10] G.J. Tibbe, B.G. de Grooth, J. Greve, G.J. Dolan, C. Rao, and L.W.M.M. Terstappen, "Magnetic field design for selecting and aligning immunomagnetic labelled cells," Cyctometry, vol. 47, pp.163-172, 2002.

[11] J. Voldman, M.L. Gray, M. Toner, and M.A. Schmidt, "A microfabrication-based dynamic array cytometer," Analytical Chemistry, vol. 77, pp. 7976-7983, 2002.

[12] B.M. Taff, and J. Voldman, "A scalable addressable positive-dielectrophoretic cell-sorting array," Analytical Chemistry, vol. 77, pp. 7975-7983, 2005.

[13] H. Kim, R.E. Cohen, P.T. Hammond, and D.J. Irvin, "Live lymphocyte arrays for biosensing," Advanced Functional Materials, vol. 16, pp. 1313-1323, 2006.

[14] V.R. Daria, P.J. Rodrigo, and J. Gluckstad, "Dynamic formation of optically trapped microstructure arrays for biosensor applications," Biosensors and Bioelectronics, vol. 19, pp. 1439-1444, 2004.

[15] K. Ino, M. Okochi, N. Konishi, M. Nakatochi, R. Imai, M. Shikida, A. Ito, and H. Honda, "Cell culture arrays using magnetic force-based cell patterning for dynamic single cell analysis," Lab on a Chip, vol. 8, pp. 134-142. 2008.

[16] M. Deutsch, A. Deutsch, O. Shirihai, I. Hurevich, E. Afrimzon, Y. Shafran, and N. Zurgil, "Anovel miniature cell retainer for correlative high-content analysis

individual untethered non-adherent cells," Lab on a Chip, vol. 6, pp. 995-1000, 2006.

[17] E. Bedner, X. Li, W. Gorczyca, M.R. Melamed, and Z. Darzynkiewicz, "Analysis of apoptosis by laser scanning cytometry," Cytometry, vol. 35, pp. 181-195, 1999.

[18] X. Chen, X. Zhou, and S.T.C. Wong, "Automated Segmentation, classification, and tracking of cancer cell nuclei in time-lapse microscopy," IEEE Transactions on Biomedical Engineering, vol 53, no. 4, pp. 762-766, 2006.

[19] M. Halter, A. Tona, Kiran, Bhadriraju, A.L. Plant, and J.T. Elliott, "Automated live cell imaging of green fluorescent protein degradation in individual fibroblasts," Cytometry Part A, vol. 71A, pp. 827-834, 2007.

[20] R., Johann, "Cell trapping in microfluidic chips," Analytical and Bioanalytical Chemistry, vol. 385, pp. 408-412, 2006.

[21] A. Neild, S. Oberti, G. Radzill, and J. Dual, "Simultaneous positioning of cells into two-dimensional arrays using ultrasound," Biotechnology and Bioengineering, vol. 97, no. 5, pp. 1335-1339, 2007.

[22] A. Khademhosseini, J. Yeh, G. Eng, J. Karp, H. Kaji, J. Borenstein, O.C. Farokhzad, and R. Langer, "Cell docking inside microwells within reversibly sealed microfluidic channels for fabricating multiphenotype cell arrays," Lab on a Chip, vol. 5, pp. 1380-1386, 2005.

[23] S. Yamamura, H. Kishi, Y. Tokimitsu, S. Kondo, R. Honda, S. Rao, M. Omori, E. Tamiya, and A. Muraguchi, "Single-cell microarray for analyzing cellular response," Analytical Chemistry, vol. 77, pp. 8050-8056, 2005.

[24] D. Di Carlo, L. Y. Wu, and L.P. Lee, "Dynamic single cell culture array," Lab on a Chip, vol. 6, pp. 1445-1449, 2006.

[25] F. Greve, J. Lictenberg, and A. Hierlemann, "Precise cell placement by pneumatic anchoring," Sensors, 2004. Proceedings of IEEE, vol.1 , pp. 80-82, 2004.

[26] D.R. Albrecht, V.L. Tsang, R.L. Sah, and S.N. Bhatia, "Photo- and electropatterning of hydrogel-encapsulated living cell arrays," Lap on a Chip, vol. 5, pp. 111-118, 2005.

[27] A. Revzin, K. Sekine, A. Sin, R.G. Tompkins, and M. Toner, "Development of a microfabricated cytometry platform for characterization and sorting of individual leukocytes," Lab on a Chip, vol. 5, pp. 30-37, 2005.

[28] M. Tanase, E.J. Felton, D.S. Gray, A. Hultgren, C.S. Chen, and D.H. Reich, "Assembly of multicellular constructs and microarrays of cells using magnetic nanowires," Lab on a Chip, vol. 5, pp. 598-605, 2005.

[29] P.Y. Chiou, A.T. Ohta, and M.C. Wu, "Massively parallel manipulation of single cells and microparticles using optical images," Nature, vol.436, pp. 370-372, 2005.

[30] X. Hu, P.H. Bessette, J. Qian, C.D. Meinhart, P.S. Daugherty, H.T. Soh, "Marker-specific sorting of rare cells using dielectrophoresis," PNAS, vol. 102, pp. 15757-15761, 2005.

[31] R.A. Flynn, A.L. Birkbeck, M. Gross, M. Ozkan, B. Shao, M.M. Wang, S.C. Esener, "Parallel transport of biological cells using individually addressable VCSEL arrays as optical tweezers," Sensor and Actuators B, vol. 87, pp. 239-243, 2002.

[32] A.L. Birdbeck, R.A. Flynn, M. Ozkan, D. Song, M. Gross, and S.C. Esener, "VCSEL arrays as micromanipulators in chip-based biosystems," Biomedical Microdevices, vol. **5**, no. 1, pp. 47-54, 2003.

[33] F. Arai, C. Ng, H. Maruyama, A. Ichikawa, H. El-Shimy, and T. Fukuda, "On chip single-cell separation and immobilization using optical tweezers and thermosensitive hydrogel," Lab on a Chip, vol. 5, pp. 1399-1403, 2005.

[34] C. Luo, H. Li, C. Xiong, X. Peng, Q. Kou, Y. Chen, H. Ji, and Q. Ouyang, "The combination of optical tweezers and microwell array for cells physical manipulation and localization," Biomedical Microdevices, vol. 9, pp. 573-578, 2007.

[35] J. Seidl, R. Knuechel, and L.A. Kunz-Schughart, "Evaluation of membrane physiology following fluorescence activated or magnetic cell separation," Cytometry vol. 36, pp. 102-111, 1999.

[36] I. Safarik, M. Safarikova, "Use of magnetic techniques for the isolation of cells," Journal of Chromatography B, vol. 722, pp. 33-53, 1999.

[37] H. Lee, A.M. Purdon, and R.M. Westervelt, "Micromanipulation of biological systems with microelectromangets," IEEE Transactions on Magnetics, vol. 40, no. 40, pp. 2991-2993, 2004.

[38] H. Lee, Y. Liu, R.M. Westervelt, D. Ham, "IC/Microfluidic hybrid system for magnetic manipulation of biological cells," IEEE Journal of Solid Static Circuit, vol. 41, no. 6, pp. 1471-1480, 2006.

[39] T, Kimura, Y. Sato, F. Kimura, M. Iwasaka, and S. Ueno, "Micropatterning of cells using modulated magnetic fields," Langmuir, vol. 21, pp. 830-832, 2005.

[40] J. Do, J. Choi, and C. Ahn, "Low-cost magnetic interdigitated array on a plastic wafer," IEEE Transactions on magnetic, vol. 40, no. 4, pp. 3009-3011, 2004

[41] J.J. Chalmer, M. Zborowski, L. Moore, S. Mandal, B. Fang, and L. Sun, "Theoretical analysis of cell separation based on cell surface marker density," Biotechnology and Bioengineering, vol. 59, no.1 pp.11-20, 1998.

[42] G. P. hatch, and R. E. Stelter, "Magnetic design considerations for devices and particles used for biological high-gradient magnetic separation (HGMS) systems," Journal of Magnetism and Magnetic Materials, vol. 225, pp. 262-276, 2001.

[43] Q.A. Pankhurst, J. Connolly, S.K. Jones, and J. Dobson, "Applications of magnetic nanoparticles in biomedicine," Journal of Physics D: Applied Physics, vol. 36, pp. R167-R181, 2003.

[44] J. Connolly, T.G. St.Pierre, and J. Dobson, "Experimental evaluation of the magnetic properties of commercially available magnetic microspherses," Bio-Medical Materials and Engineering, vol. 15, pp. 421-431, 2005.

[45] N. Pamme, "Magnetism and microfluidics," Lab on a Chip, vol. 6, pp. 24-38, 2006.

[46] C. Liu, *Foundations of MEMS*, New Jersey: Pearson Education Inc., 2006.

[47] C. Liu, "Development of surface micromachined magnetic actuators using electroplated permalloy", Mechatronics, vol. 8, no. 5, pp. 613-633, 1998.

[48] O. Cugat, J. Delamare, and G. Reyne, "Magnetic Micro-Actuators and Systems (MAGMAS)", IEEE Transactions on Magnetics, vol. 39, no. 5, pp.3607-3612, 2003.

[49] N.V. Myung, D. Park, B. Yoo, and P.T.A. Sumodjo, "Development of electroplated magnetic materials for MEMS", Journal of Magnetism and Magnetic Materials, vol. 265, pp.189-198, 2003.

[50] P.C. Andricacos, and N. Robertson, "Future directions in electroplated materials for thin-flim recording heads", IBM Journal of Research and Development, vol. 42, no. 5, pp. 671-680, 1998.

[51] R Bozorth, *Ferromagnetism*, New Jersey: D. Van Nostrand Company, Inc., 1951.

[52] W.P. Taylor, M. Schneider, H. Baltes, and M.G. Allen, "Electroplated soft magnetic materials for microsensors and microactuators," IEEE Transducers '97, 1997, pp. 1445-1448.

[53] J.Y. Park, M.G. Allen, "Development of magnetic materials and processing techniques applicable to integrated micromagnetic devices," Journal of Micromechanical Microengineering, vol. 8, pp. 307-316, 1998.

[54] W. Ruythooren, K. Attenborough, S. Beerten, P. Merken, J. Fransaer, E. Beyne, C. Van Hoof, J. De Boeck, and J.C. Celis, "Electrodeposition for the synthesis of microsystems", Journal of Micromechanical Microengineering, vol. 10, pp. 101-107, 2000.

[55] S.Guan, and B.J. Nelson, "Magnetic composite electroplating for deposition micromagnets," Journal of Microelectromechanical Systems, vol. 15, no. 2., pp. 330-337, 2006.

[56] D. Niarchos, "Magnetic MEMS: keys issues and some applications," Sensors and Actuators A, vol. 106, pp. 255-262, 2003.

[57] M. Datta, and D. Landolt, "Fundamental aspects and applications of electrochemical microfabrication," Electrochimica Acta, vol. 45, pp. 2535-2558, 2000.

[58] W.C. Grande, and J.B. Talbot, "Electrodeposition of thin films of nickel-iron I. experimental," Journal of Electrochemical Society, vol. 14-, no. 3, 1993.

[59] D.L. Grimmett, M. Schwarts, and K. Nobe, "A comparison of DC and pulsed Fe-Ni alloy deposits," Journal of Electrochemical Society, vol. 140, no. 4, 1993.

[60] J. Quemper, S. Nicolas, J.P. Gilles, J.P. Grandchamp, A. Bosseboeuf, T. Bourouina, and E. Dufour-Gergam, "Permalloy electroplating through photoresist molds," Sensors and Actuators, vol. 74, pp. 1-4, 1999.

[61] S.D. Leith, and D.T. Schwartz, "High-rate through-mold electrodeposition of thick (>200 μm) NiFe MEMS components with uniform composition," Journal of Microelectromechanical Systems, vol. 8, no. 4, 1999.

[62] S.D. Leith, S. Ramli, and D.T. Schwartz, "Characterization of Ni_xFe_{1-x} ($0.10 < x < 0.95$) electrodeposition from a family of sulfamate-chloride electrolytes," Journal of the electrochemical society, vol. 146, no. 4, pp. 1431-1435, 1999.

[63] T. Kohlmier, V. Seidemann, S. Büttgenbach, H.H. Gatzen, "An investigation on technologies to fabricate microcoils for miniaturized actuator systems", Microsystem Technologies, vol. 10, pp.175-181, 2004.

[64] K.E. McCloskey, J.J. Chalmers, and M. Zborowski, "Magnetic Cell Separation: Characterization of Magnetophoretic Mobility", Analytical Chemistry, vol. 75, pp. 6868-6874, 2003.

[65] C.E. Orsello, D.A. Lauffenburger, and D.A. Hammer, "Molecular properties in cell adhesion: a physical and engineering perspective", TRENDS in Biotechnology, vol. 19, no. 8, pp. 310-316, 2001.

[66] K. McCloskey, J. Chalmers, and M. Zborowski, "Magnetophoretic Mobilities Correlate to Antibody Binding Capacities" Cytometry, vol. 40, pp. 307-315, 2000.

[67] M. Zborowski, L. Sun, L.R. More, P.S. Williams, and J.J. Chalmers, "Continuous cell separation using novel magnetic quadrupole flow sorter," Journal of Magnetism and Magnetic Materials, vol. 194, pp. 224-230, 1999.

[68] P. Todd, R.P. Cooper, J.F. Doyle, S. Dunn, J. Vellinger, M.S. Deuser, "Multistage magnetic particle separator," Journal of Magnetism and Magnetic Materials, vol. 225, pp. 294-300.

[69] I. Meyvantsson, J.W. Warrick, S. Hayes, A. Skoien, and D. Beebe, "Automated cell culture in high density tubless microfluidic device arrays," Lab on a Chip, vol. 8, pp. 717-724, 2008.

[70] K. Sakaki, N. Dechev, E.J. Park, R.D. Burke, "Development of a five degree-of freedom biomanipulator for autonomous single cell electroporation," in IEEE/RSJ International Conference on Intelligent Robots and Systems IROS 2007, 2007, pp. 3137-3143.

[71] J. Do, and C.H. Ahn, "A polymer lab-on-achip for magnetic immunoassay with on-chip sampling and detection capabilities," Lab on a Chip, vol. 8, pp. 542-549, 2008.

[72] K.D.R. Sakaki, "Development of a five degree-of-freedom robot for the manipulation of biological cells", M.A.Sc. thesis, University of Victoria, Victoria, BC, Canada, 2007.

Appendix A Data Points of H vs μ_r Plot of Permalloy

External magnetization **H** (A/m)	μ_r
-8037324	1
-779859	2
-190985	5.083333
-79577	10.8
-55704	15
-47746	17.33333
-39789	20.6
-31831	25.5
-23873	33.66667
-15915	50
-7958	95
-3979	180
-3187	218.75
-2387	283
-1592	400
-1000	665.7311
-990	668.786
-980	671.7208
-970	674.5321
-960	677.2164
-950	679.7699
-940	682.1893
-930	684.471
-920	686.6114
-910	688.6069
-900	690.4541
-890	692.1494
-880	693.6891
-870	695.0699
-860	696.2881
-850	697.3402
-840	698.2227
-830	698.9319
-820	699.4644
-810	699.8166
-800	699.9849
-796	700
0	700
796	700
800	699.9849
810	699.8166
820	699.4644
830	698.9319

External magnetization **H** (A/m)	μ_r
840	698.2227
850	697.3402
860	696.2881
870	695.0699
880	693.6891
890	692.1494
900	690.4541
910	688.6069
920	686.6114
930	684.471
940	682.1893
950	679.7699
960	677.2164
970	674.5321
980	671.7208
990	668.786
1000	665.7311
1592	400
2387	283
3187	218.75
3979	180
7958	95
15915	50
23873	33.66667
31831	25.5
39789	20.6
47746	17.33333
55704	15
79577	10.8
190985	5.083333
779859	2
8037324	1

Appendix B MatLab Code for Plotting Gradient of B-field

```
function [gx,gy,gz,x,y,z] = gradplot (grid_vec,fem,scalar_name)

%Defining the grid

x = linspace (grid_vec(1,1),grid_vec(1,2),grid_vec(1,3));
y = linspace (grid_vec(2,1),grid_vec(2,2),grid_vec(2,3));
z = linspace (grid_vec(3,1),grid_vec(3,2),grid_vec(3,3));

dx = x(2)-x(1);
dy = y(2)-y(1);
dz = z(2)-z(1);
[x,y,z] = meshgrid(x,y,z);
mesh_size = size(x);
coor = [x(:),y(:),z(:)];
coor = transpose(coor);

%Read data from solution structure, sol_name is name for the fem
solution

svec = postinterp(fem,scalar_name,coor,'ext',1e-6);

sfield = (formgrid(svec,mesh_size(2),mesh_size(1),mesh_size(3))).^2;
%Formgrid assign the norm of B-field to each point, value is squared
for this purpose only
[gx,gy,gz]=gradient(sfield,dx,dy,dz);

figure('Name','Gradient_Plot');
subplot (3,3,[1:6]);
patch([120e-6 120e-6 130e-6 140e-6 150e-6 160e-6 170e-6 180e-6 180e-6],
[10e-6 55e-6 50e-6 30e-6 25e-6 30e-6 50e-6 55e-6 10e-6],[0.5 0.5 0.5]);
%Draw the outline of the permalloy
hold on;
subplot (3,3,[1:6]); quiver3(x,y,z,gx,gy,gz);
axis equal;
axis([grid_vec(1,1) grid_vec(1,2) grid_vec(2,1) grid_vec(2,2)
grid_vec(3,1) grid_vec(3,2)]);
view(3);
grid on;

subplot (3,3,7); patch([0 0 10e-6 20e-6 30e-6 40e-6 50e-6 60e-6 60e-6],
[10e-6 55e-6 50e-6 30e-6 25e-6 30e-6 50e-6 55e-6 10e-6],[0.5 0.5 0.5]);
hold on;
subplot (3,3,7); quiver(x(:,:,(1)),y(:,:,(1)),gx(:,:,(1)),gy(:,:,(1)));
subplot (3,3,7); contour(x(:,:,(1)),y(:,:,(1)),gz(:,:,(1)),[-1000 -900
-800 -700 -600 -500 -400 -300 -200 -100 0 100 200]);
axis equal;
axis([grid_vec(1,1) grid_vec(1,2) grid_vec(2,1) grid_vec(2,2)]);

%figure('Name','Gradient_Plot_xy_level2');
subplot (3,3,8); patch([0 0 10e-6 20e-6 30e-6 40e-6 50e-6 60e-6 60e-6],
[10e-6 55e-6 50e-6 30e-6 25e-6 30e-6 50e-6 55e-6 10e-6],[0.5 0.5 0.5]);
```

```
hold on;
subplot (3,3,8); quiver(x(:,:,(2)),y(:,:,(2)),gx(:,:,(2)),gy(:,:,(2)));
subplot (3,3,8); contour(x(:,:,(2)),y(:,:,(2)),gz(:,:,(2)),[-1000 -900
-800 -700 -600 -500 -400 -300 -200 -100 0 100 200]);
axis equal;
axis([grid_vec(1,1) grid_vec(1,2) grid_vec(2,1) grid_vec(2,2)]);

%figure('Name','Gradient_Plot_xy_level3');
subplot (3,3,9); patch([0 0 10e-6 20e-6 30e-6 40e-6 50e-6 60e-6 60e-6],
[10e-6 55e-6 50e-6 30e-6 25e-6 30e-6 50e-6 55e-6 10e-6],[0.5 0.5 0.5]);
hold on;
subplot (3,3,9); quiver(x(:,:,(3)),y(:,:,(3)),gx(:,:,(3)),gy(:,:,(3)));
subplot (3,3,9); contour(x(:,:,(3)),y(:,:,(3)),gz(:,:,(3)),[-1000 -900
-800 -700 -600 -500 -400 -300 -200 -100 0 100 200]);
axis equal;
axis([grid_vec(1,1) grid_vec(1,2) grid_vec(2,1) grid_vec(2,2)]);

return


function [result] = formgrid (vfeed,an,bn,cn)

for k=1:cn
    for i=1:an
        for j=1:bn
            result(j,i,k) = vfeed((k-1)*an*bn+(i-1)*bn+j);
        end
    end
end

return
```

Appendix C Time-lapsed Images of Magnetic Particles Arraying Experiment

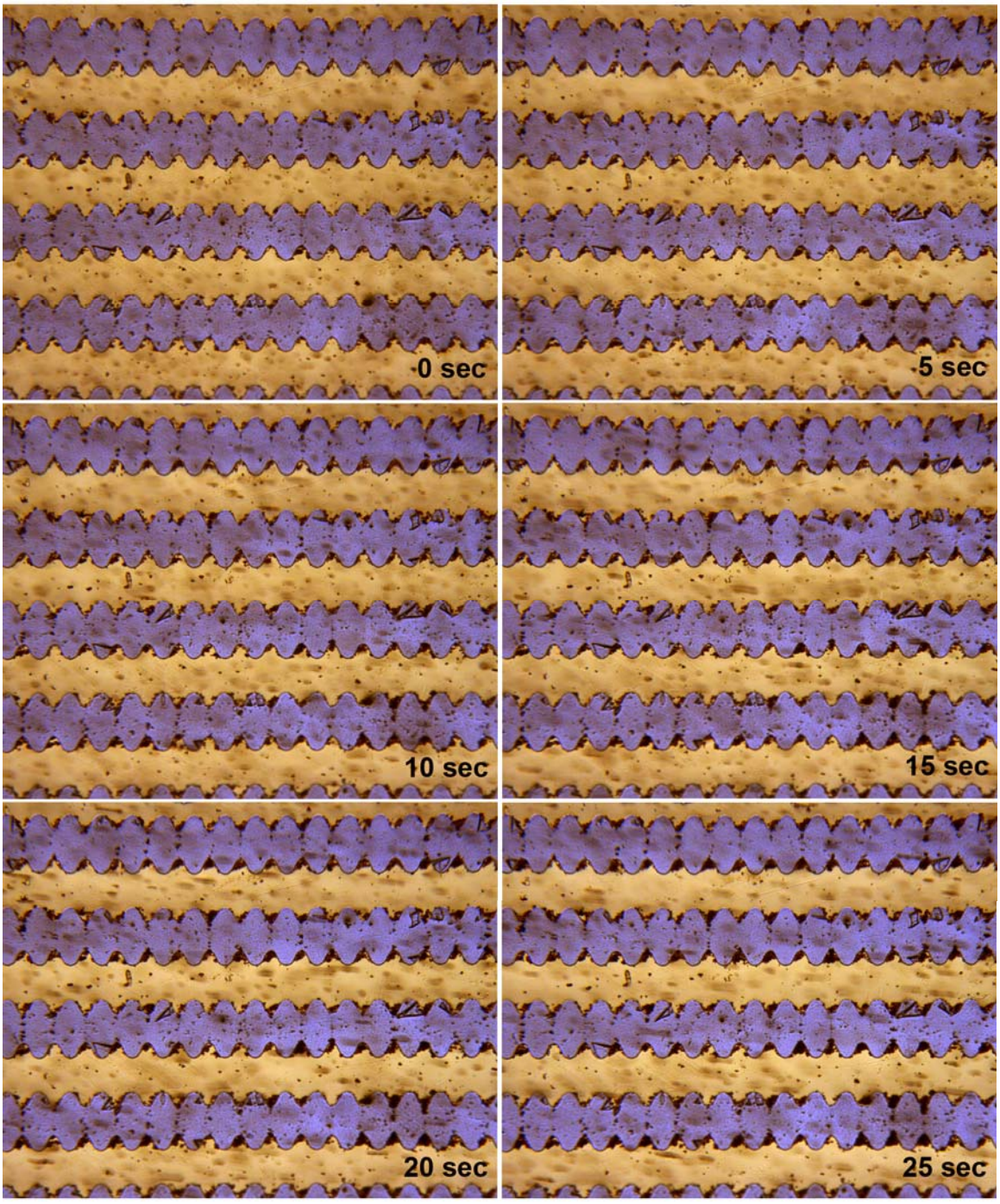

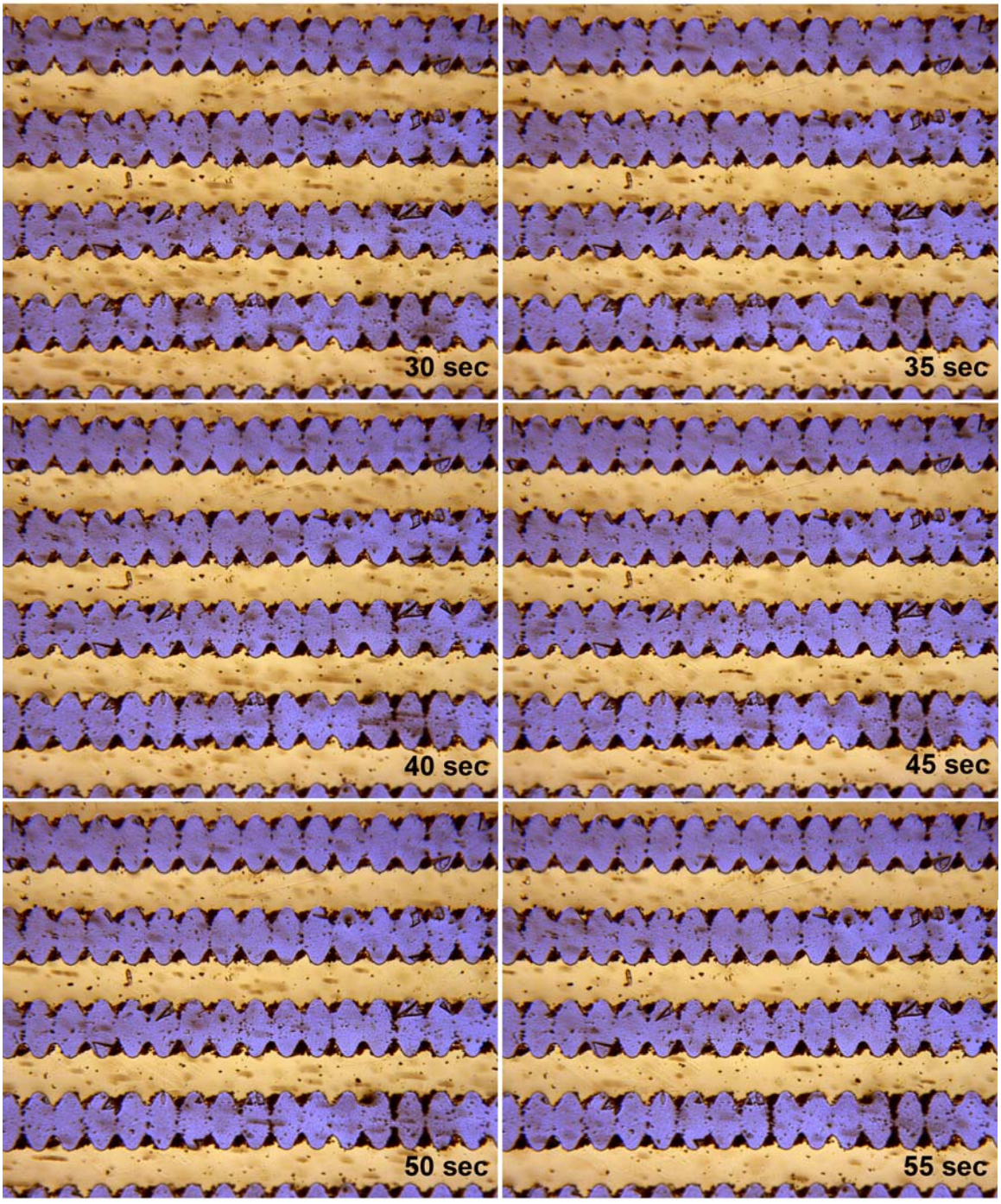
30 sec
35 sec
40 sec
45 sec
50 sec
55 sec

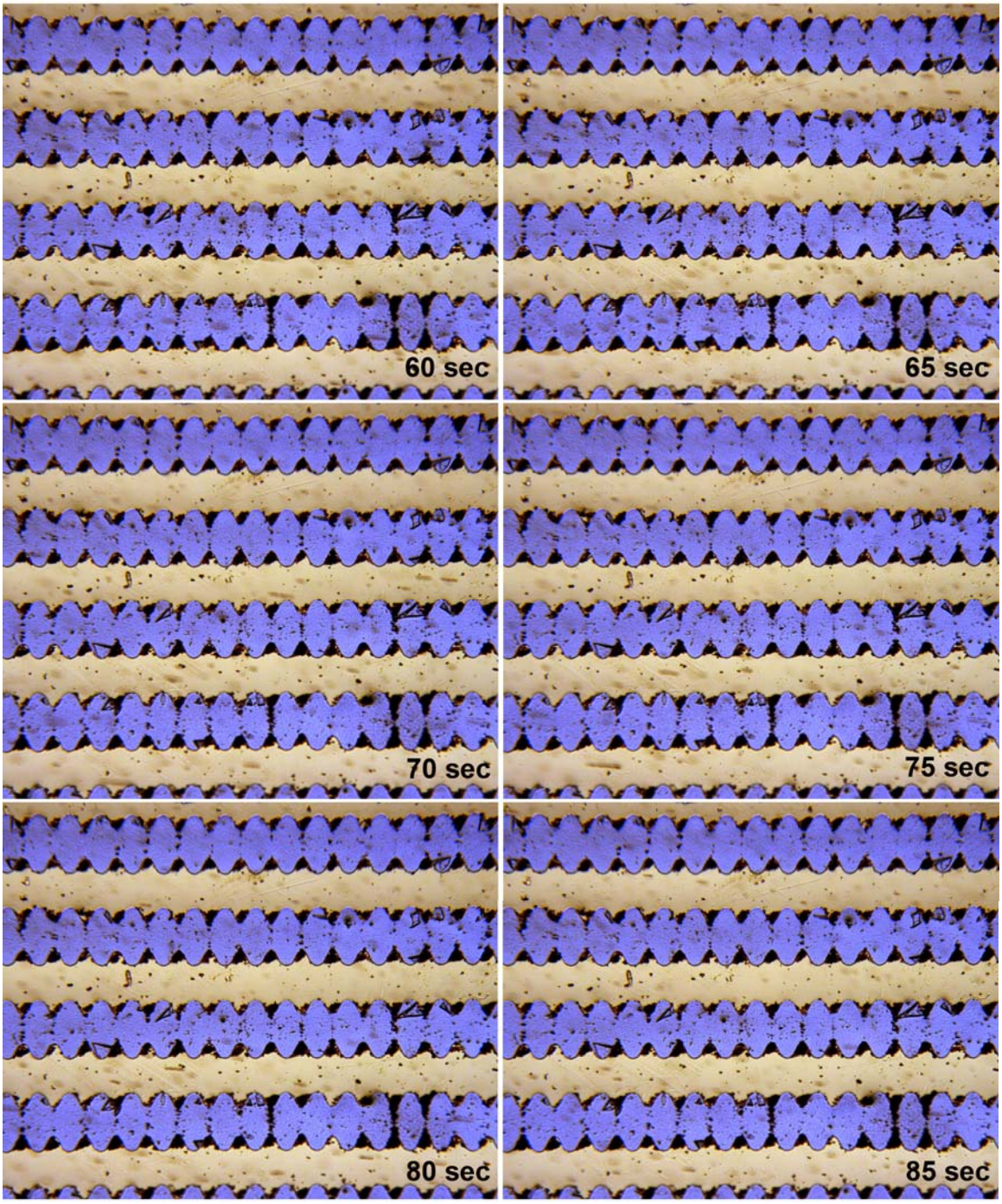
60 sec
65 sec
70 sec
75 sec
80 sec
85 sec

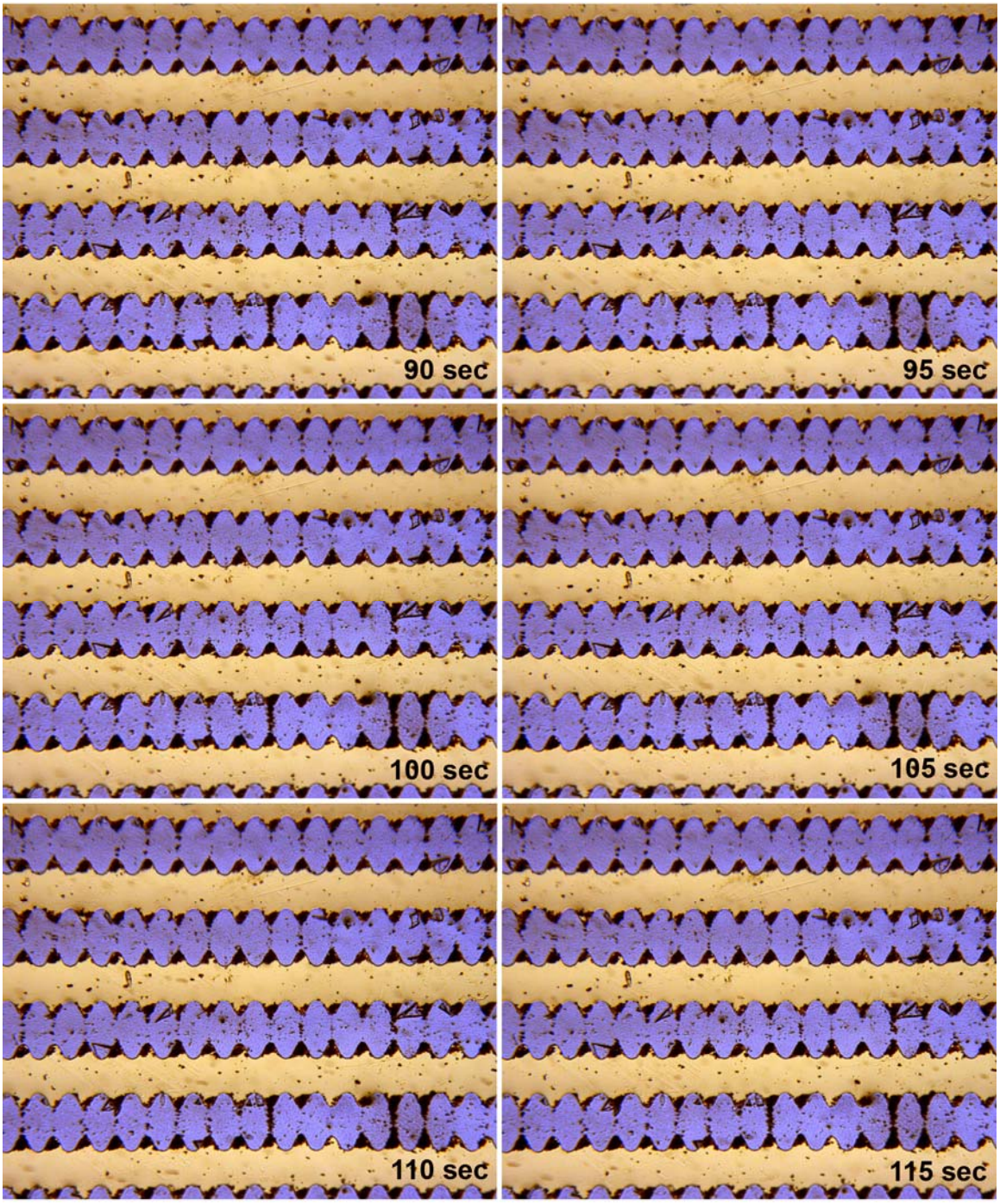
90 sec
95 sec
100 sec
105 sec
110 sec
115 sec

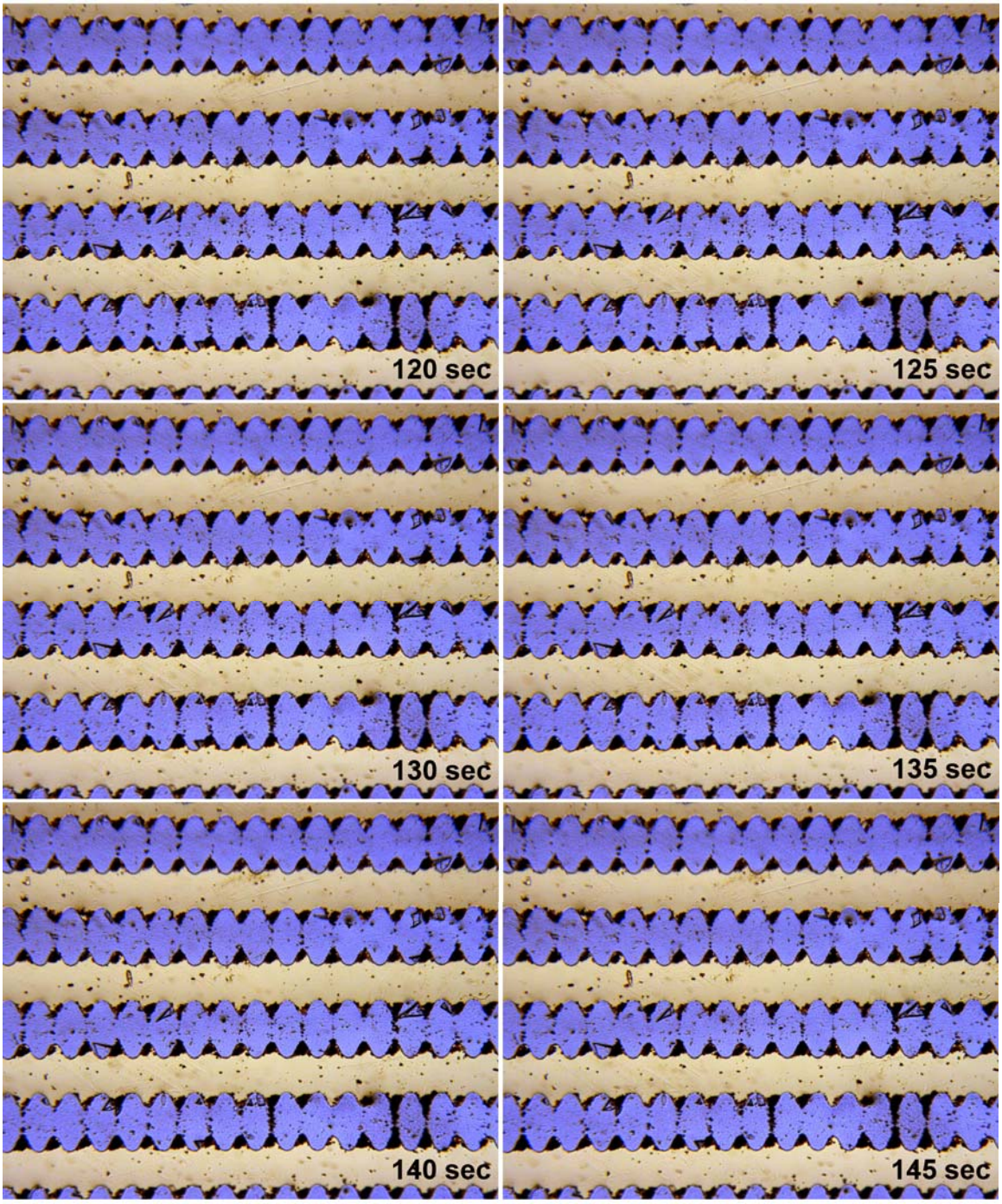
120 sec
125 sec
130 sec
135 sec
140 sec
145 sec

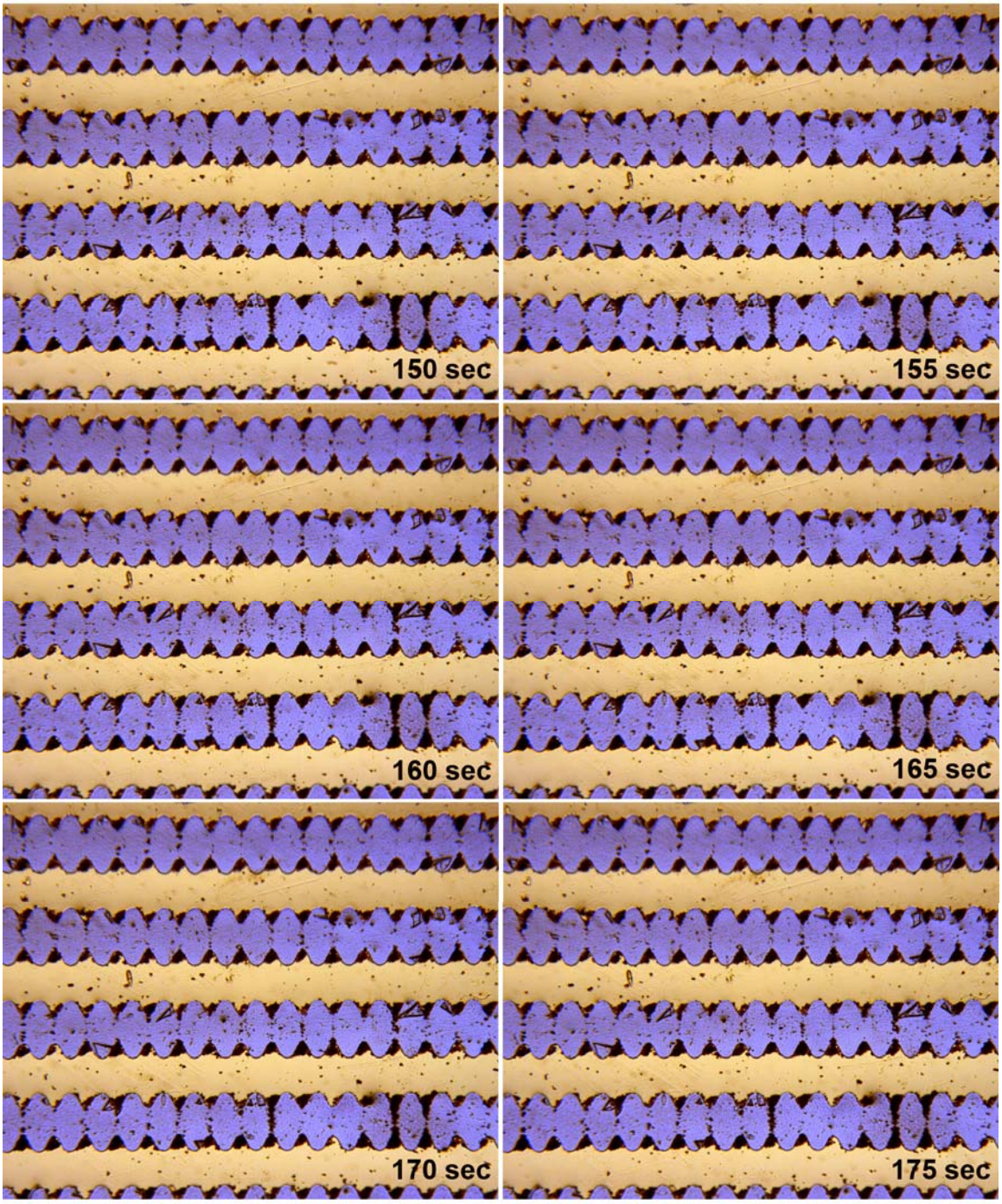
150 sec
155 sec
160 sec
165 sec
170 sec
175 sec

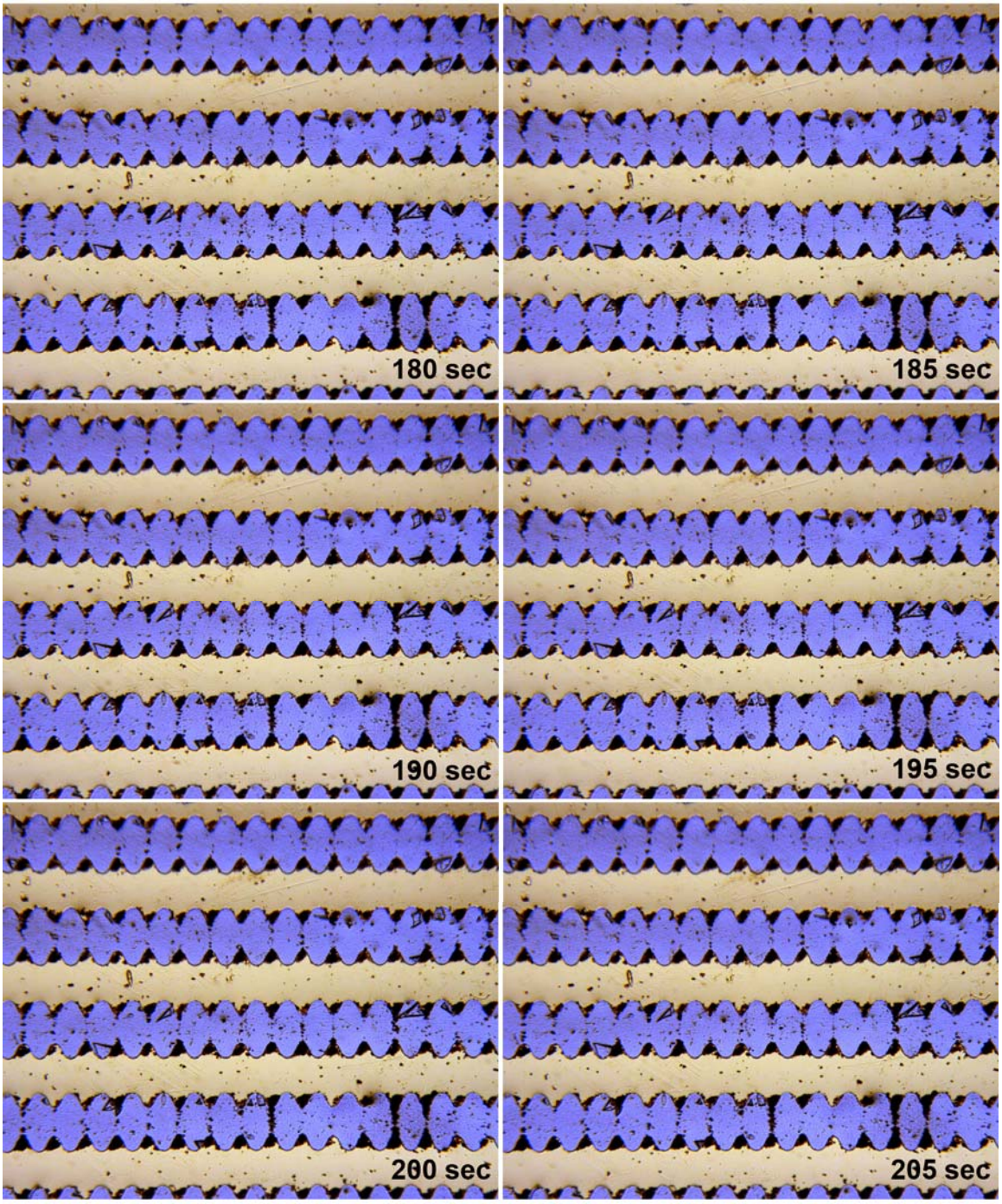
180 sec
185 sec
190 sec
195 sec
200 sec
205 sec

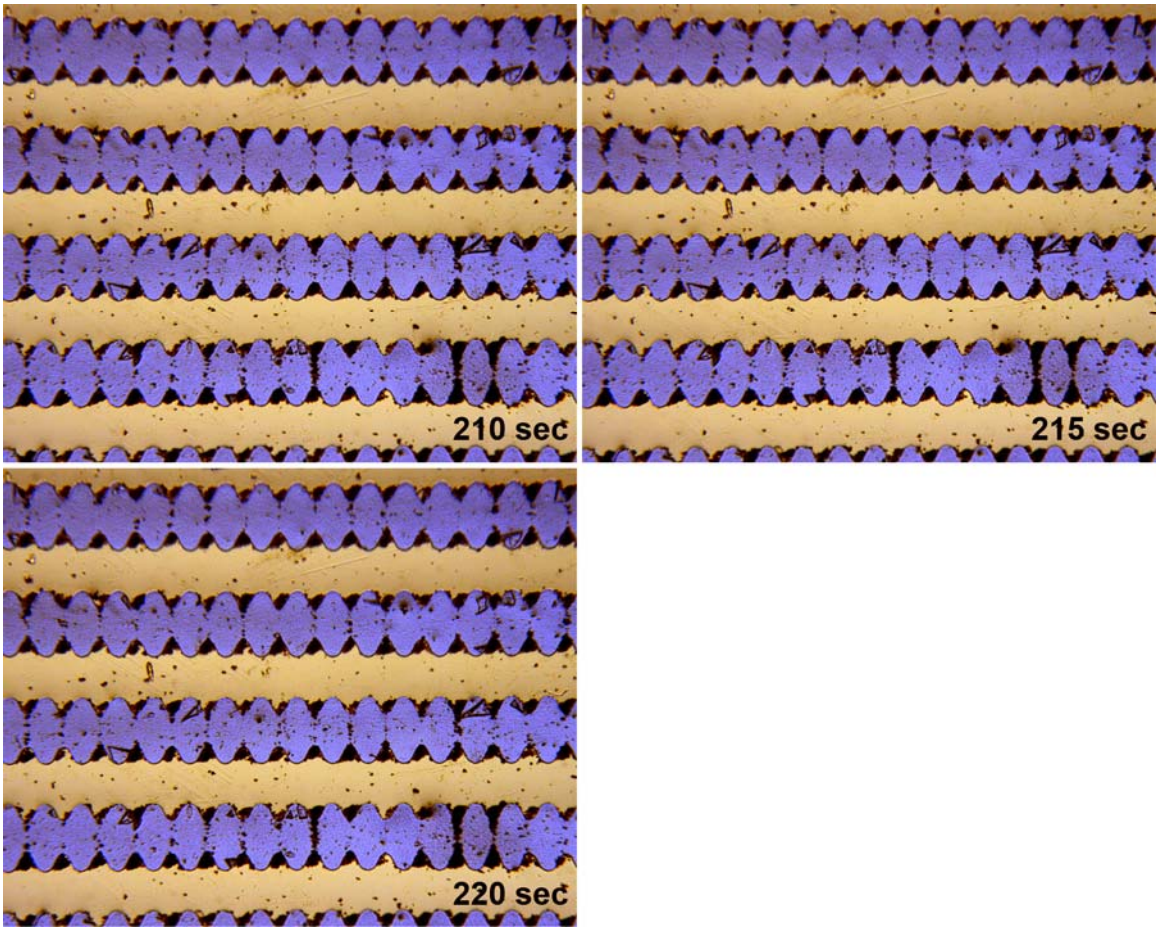
210 sec
215 sec
220 sec

Appendix D Time-lapsed Images of Cell Arraying Experiment

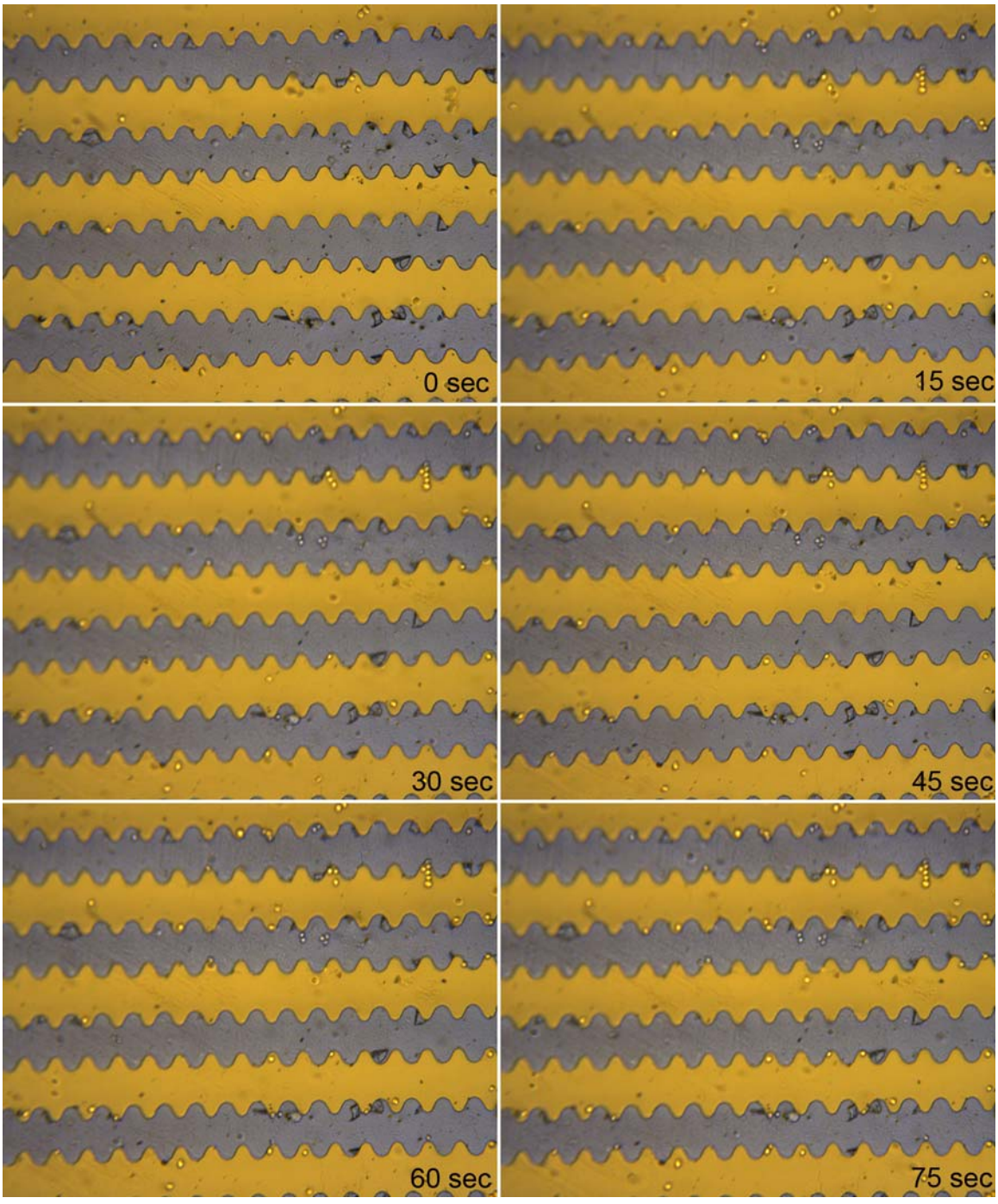

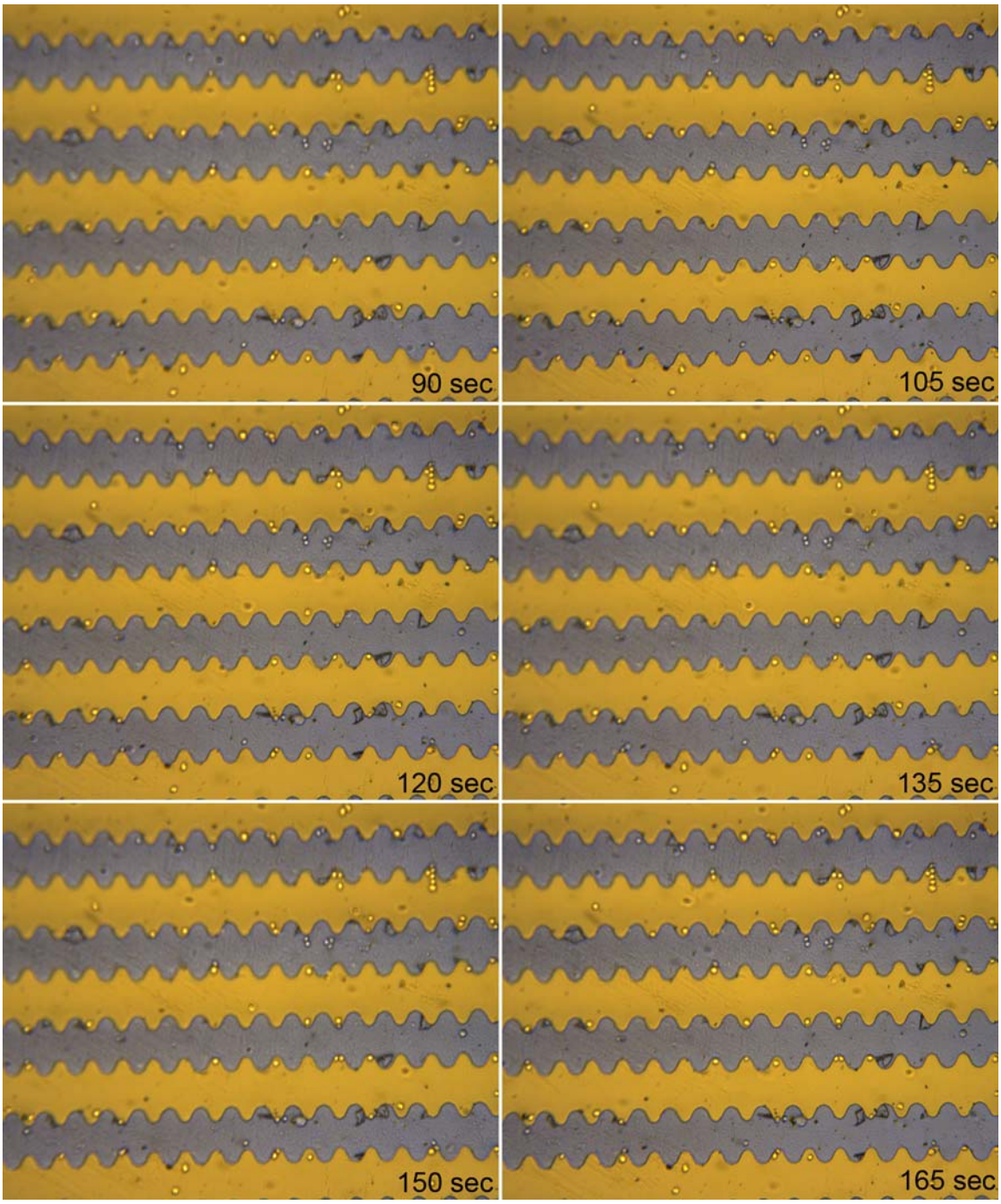
90 sec
105 sec
120 sec
135 sec
150 sec
165 sec

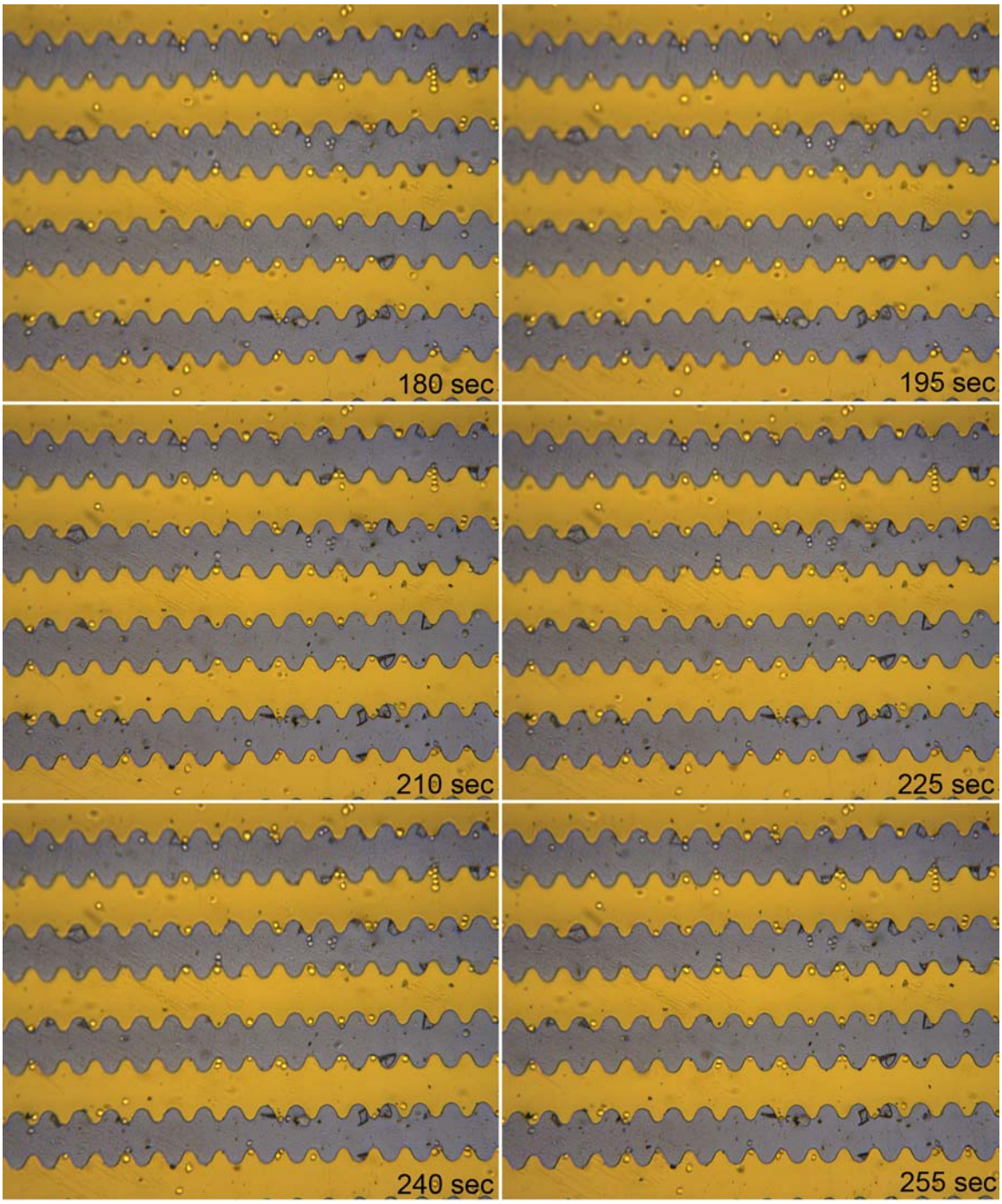
180 sec
195 sec
210 sec
225 sec
240 sec
255 sec

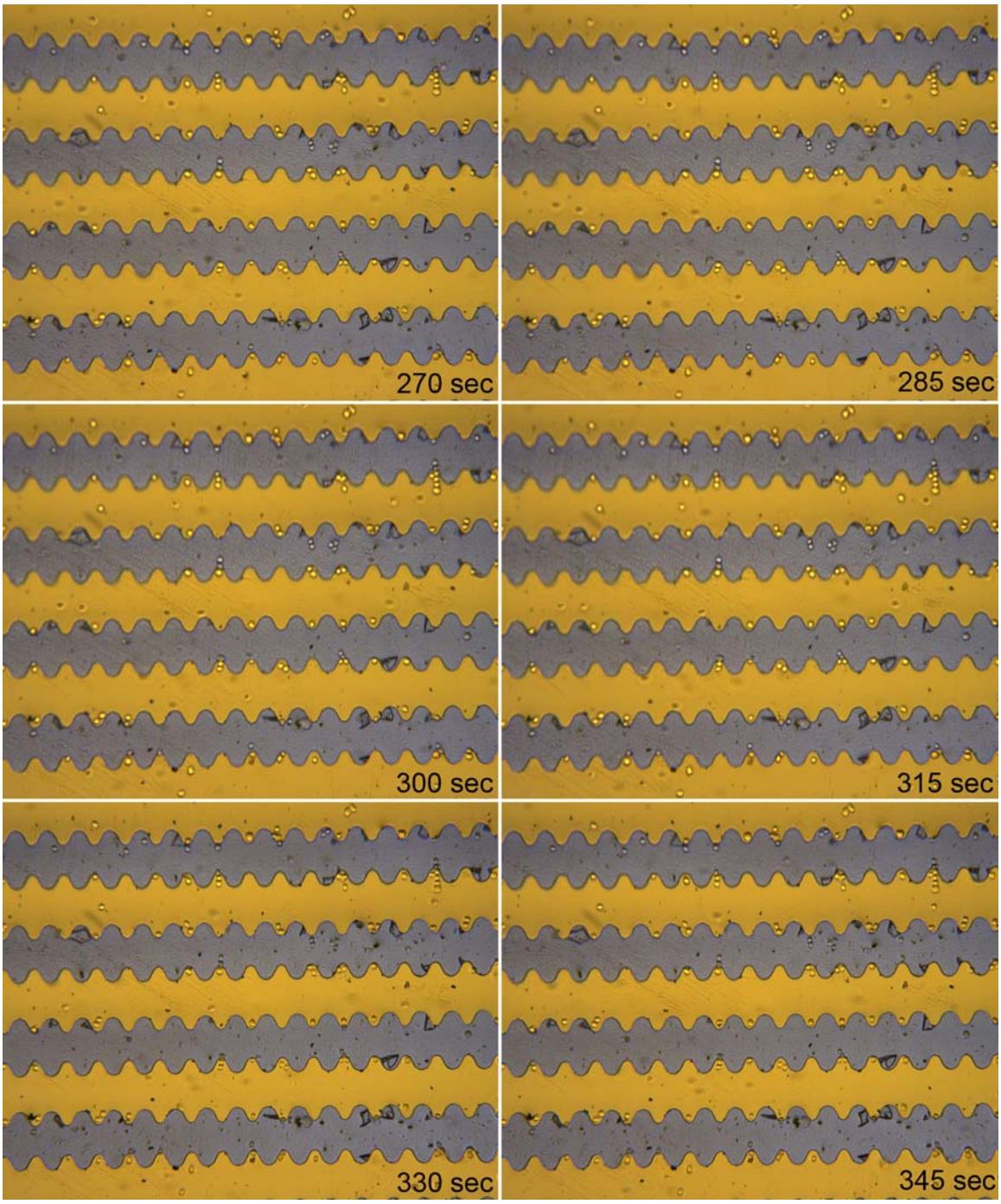
270 sec
285 sec
300 sec
315 sec
330 sec
345 sec

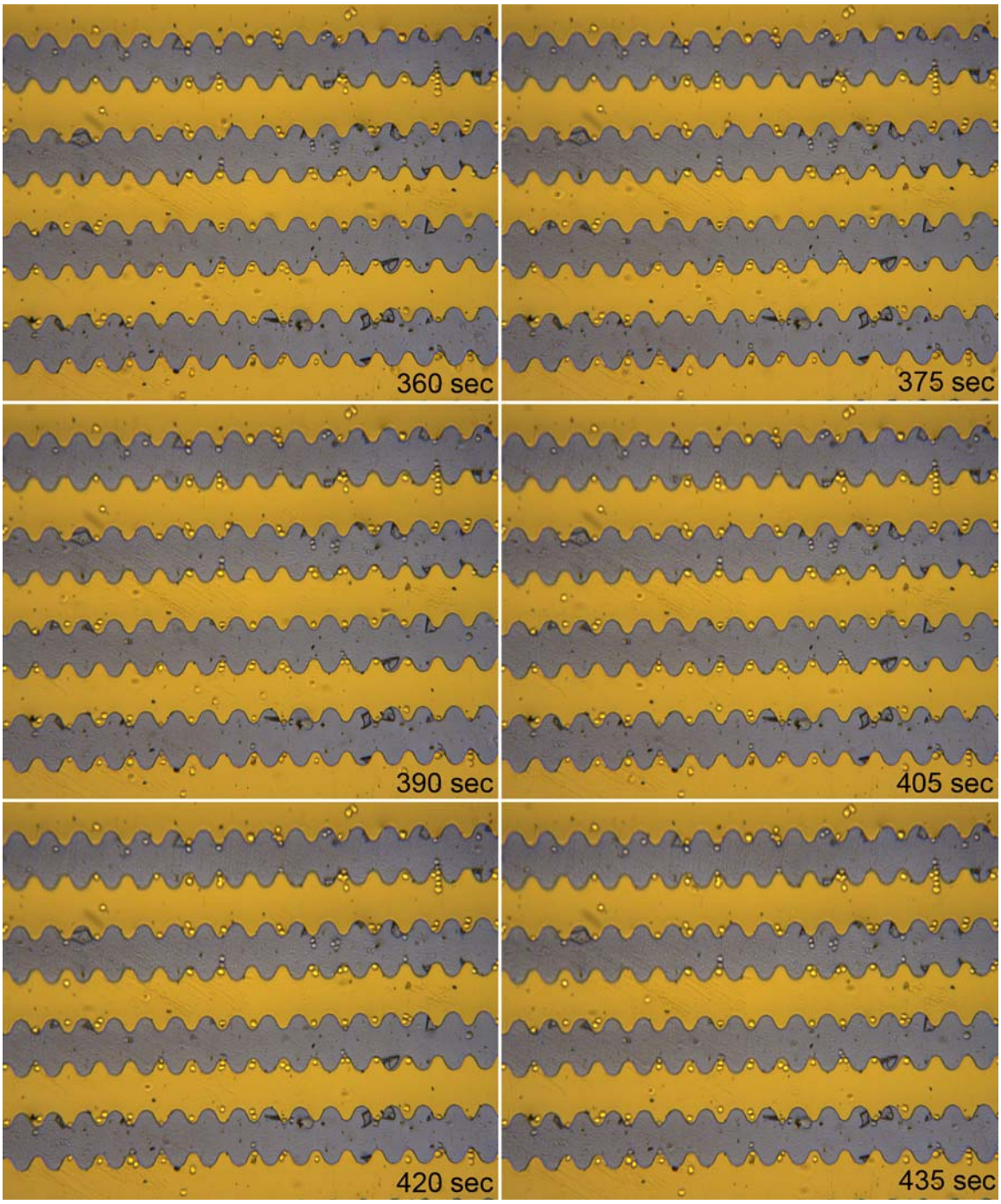
360 sec
375 sec
390 sec
405 sec
420 sec
435 sec

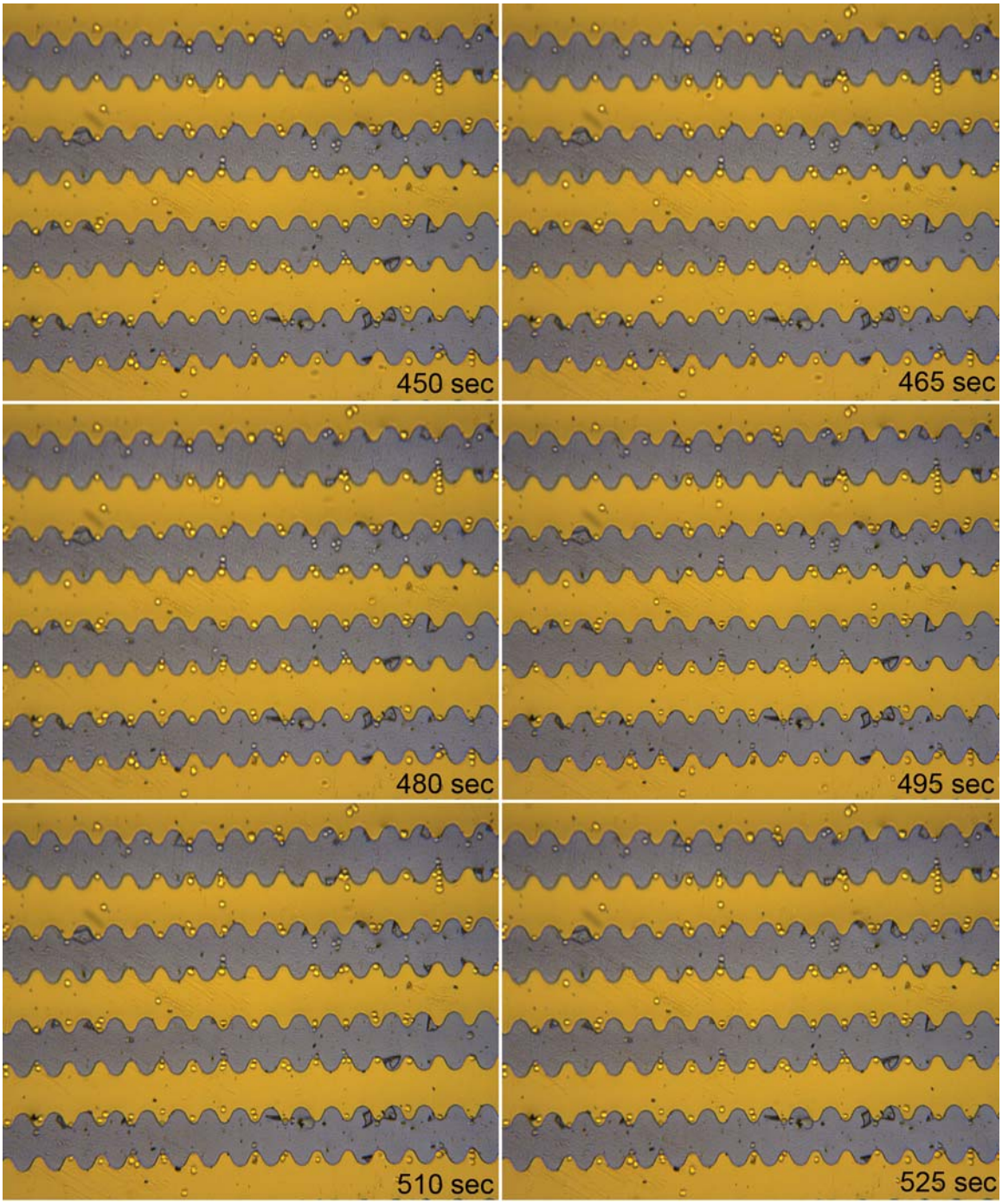
450 sec
465 sec
480 sec
495 sec
510 sec
525 sec